2012

High Temperature Materials Characterization And Sensor Application

Xinhua Ren
University of Central Florida

HIGH TEMPERATURE MATERIALS CHARACTERIZATION AND SENSOR APPLICATION

by

XINHUA REN
B.S. University of Science and Technology of China, 2006
M.S. University of Central Florida, 2010

A dissertation submitted in partial fulfillment of the requirements
for the degree of Doctor of Philosophy
in the Department of Electrical Engineering and Computer Science
in the College of Engineering & Computer Science
at the University of Central Florida
Orlando, Florida

Fall Term
2012

Major Professor: Xun Gong

ABSTRACT

This dissertation presents new solutions for turbine engines in need of wireless temperature sensors at temperatures up to 1300^{o}C. Two important goals have been achieved in this dissertation. First, a novel method for precisely characterizing the dielectric properties of high temperature ceramic materials at high temperatures is presented for microwave frequencies. This technique is based on a high-quality (Q)-factor dielectrically-loaded cavity resonator, which allows for accurate characterization of both dielectric constant and loss tangent of the material. The dielectric properties of Silicon Carbonitride (SiCN) and Silicoboron Carbonitride (SiBCN) ceramics, developed at UCF Advanced Materials Processing and Analysis Center (AMPC) are characterized from 25 to 1300^{o}C. It is observed that the dielectric constant and loss tangent of SiCN and SiBCN materials increase monotonously with temperature. This temperature dependency provides the valuable basis for development of wireless passive temperature sensors for high-temperature applications.

Second, wireless temperature sensors are designed based on the aforementioned high-temperature ceramic materials. The dielectric constant of high-temperature ceramics increases monotonically with temperature and as a result changes the resonant frequency of the resonator. Therefore, the temperature can be extracted by measuring the change of the resonant frequency of the resonator. In order for the resonator to operate wirelessly, antennas need to be included in the design. Three different types of sensors, corresponding to different antenna configurations, are designed and the prototypes are fabricated and tested. All of the sensors successfully perform at temperatures over 1000^{o}C. These wireless passive sensor designs will significantly benefit turbine engines in need of sensors operating at harsh environments.

ACKNOWLEDGMENTS

I wish to express appreciation to my advisor, Prof. Xun Gong, for his guidance and support over my six years at the University of Central Florida. He provided me with a project that turned out to become the basis of my dissertation He taught me many things both inside and outside of the classroom, and I will get benefits from these lessons forever. The members of my dissertation committee: Prof. Thomas Wu, Prof. Parveen Wahid, and Prof. Linan An for sharing their wealth of knowledge through courses, valuable insight and suggestions on how to improve the quality of my research. Thank you!

The members of the Antenna, RF, Microwave, and Integrated Systems (ARMI) lab for the abundance of peer support. I would like to acknowledge Dr. Siamak Ebadi, Mr. Haitao Cheng , Mr. Justin Luther, Ms. Ya Shen, Mr. Kalyan Karnati, and Ms. Tianjiao Li for their always valuable insights and contributions, and more importantly for their personal friendships. Thank you!

Lastly, I wish to thank my family and friends, who have been incredibly supportive of me. Without all of you, I certainly would not have made it this far. Thank you!

TABLE OF CONTENTS

LIST OF FIGURES

LIST OF TABLES

CHAPTER 1 INTRODUCTION

1.1 Motivation

New generations of turbines require the rotating blades to survive temperatures up to 1300^{o}C and more. This extremely high temperature is required in different types of turbines, including gas and jet turbines, in order to achieve higher engine efficiency [1]. This elevated temperature imposes a great challenge on the fabrication of turbine blades. In addition, if the temperature is not properly monitored at the vicinity of the turbine blades, there is a high chance for overheating, causing thermal damage. This has caused reduced engine lifetimes and calls for more frequent replacement of the blades. "However, currently there is no existing technology that can provide online, real time monitoring of the temperature within the hot sections of turbines. In the past decade, several techniques were under development for this purpose" [2]. Optical-based non-contact technology is currently being developed for measuring the operating temperature in turbine engines. This indirect measurement technology however lacks the necessary capabilities or accuracy [3][4][5][6] and "typically fails over the time due to the smearing of the dielectric windows" [2] . Another effective alternate method to measure these parameters without disturbing the working environment could be to use miniaturized sensors. Silicon carbide (SiC) and silicon nitride (Si_3N_4)-based ceramic micro-sensors are currently under the development for high temperature sensing application in harsh environment [7][8][9][10][11][12]. Those sensors are seriously restricted by limited fabrication methods, high cost, and limited operating temperature range (typically < 800^{o}C). In fact, any micro-sensor that involves electronic components and packaging has a slim chance of surviving in high-

temperature environments. Therefore, it is highly desired to develop low profile temperature sensors seamlessly integrated with the turbine blades, which continuously monitor the temperature, and wirelessly communicate with the outside environment. The next-generation sensors for turbines must have the following advantages: 1) wireless; 2) high accuracy; 3) robustness; 4) small size and flexibility; 5) low cost. "These requirements call for new sensor materials and innovative sensor designs" [2] .

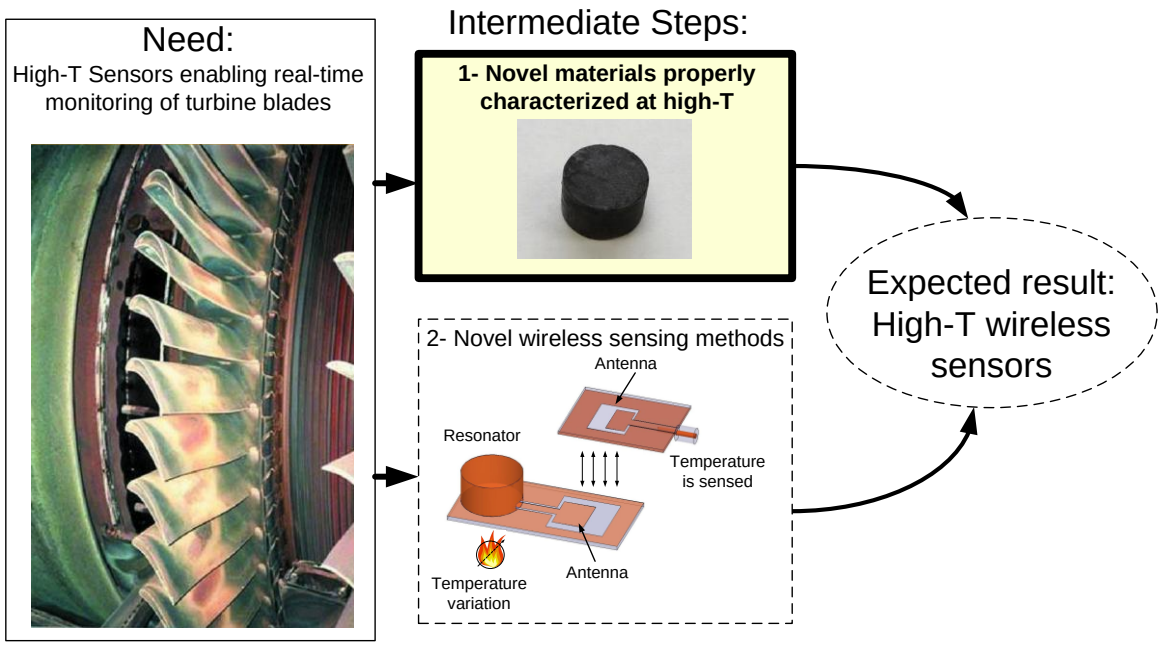

Figure 1.1: Illustration of the need for sensors to monitor extremely high temperatures of the turbine blade; novel material characterization methods and wireless sensing mechanisms are necessary to achieve this goal.

Fig. 1.1 illustrates the problem statement and the proposed solution. Hot and worn blades are visible in the left hand side image. This undesired fact can be prevented by developing the aforementioned sensor concept. Such a sensor is in need of two technologies in order to be successfully realized. First, novel materials need to be developed that can withstand the extremely hot environment inside turbines. In addition, such materials need to have electromagnetic properties which are desired in the sensor development. This may include temperature-variant dielectric permittivity, which is fundamentally congruent with wireless sensor realization. The critical final step in the material development is the electromagnetic characterization at elevated temperatures. The results of such characterization would reveal usefulness of the material for the sensor application.

The second question to be asked is how to use the newly developed and characterized materials and design a sensor. This calls for development of novel wireless sensing mechanisms which are tailored to our specific turbine application. In order for the sensor to be wirelessly interrogated, it will need an antenna which can send out and receive electromagnetic fields containing information about the sensor's temperature.

Successful answers to the aforementioned two questions will result in a wireless temperature sensor which can provide real-time monitoring of the turbine blade at extremely high temperatures. This dissertation is initially focused on the newly proposed characterization method for measuring the dielectric property of the new ceramic materials at high temperature. Furthermore, several types of wireless high temperature sensors are designed and tested utilizing

the characterized ceramic materials. In the following section, different material characterization techniques which can be potentially used at elevated temperatures are reviewed.

1.2 Literature Review: Existing Material Characterization Methods

Microwave frequencies are preferred for efficient transmission of electromagnetic waves, which is critical for realization of a wireless sensor. In addition, operating at high frequencies in the microwave regime allows for implementation of small size sensors with minimum undesired effects on the aerodynamic performance of the turbine blades. In order to design a wireless sensor at a particular frequency, the fundamental properties of the material, referred to as a dielectric in this context, need to be known. The two main properties to be characterized through this process are the dielectric constant ε_r and the loss tangent $\tan\delta$.

There exist several of methods which can measure the properties of an unknown material at microwave frequencies. In all of these approaches, the unknown material is exposed to a known electromagnetic waveform and modifies the properties of the waveform. The changes caused by the presence of the unknown material are measured and then translated to the desired dielectric properties using post-processing techniques. This process needs to be carried out over the temperature range in which the turbine blade is operating.

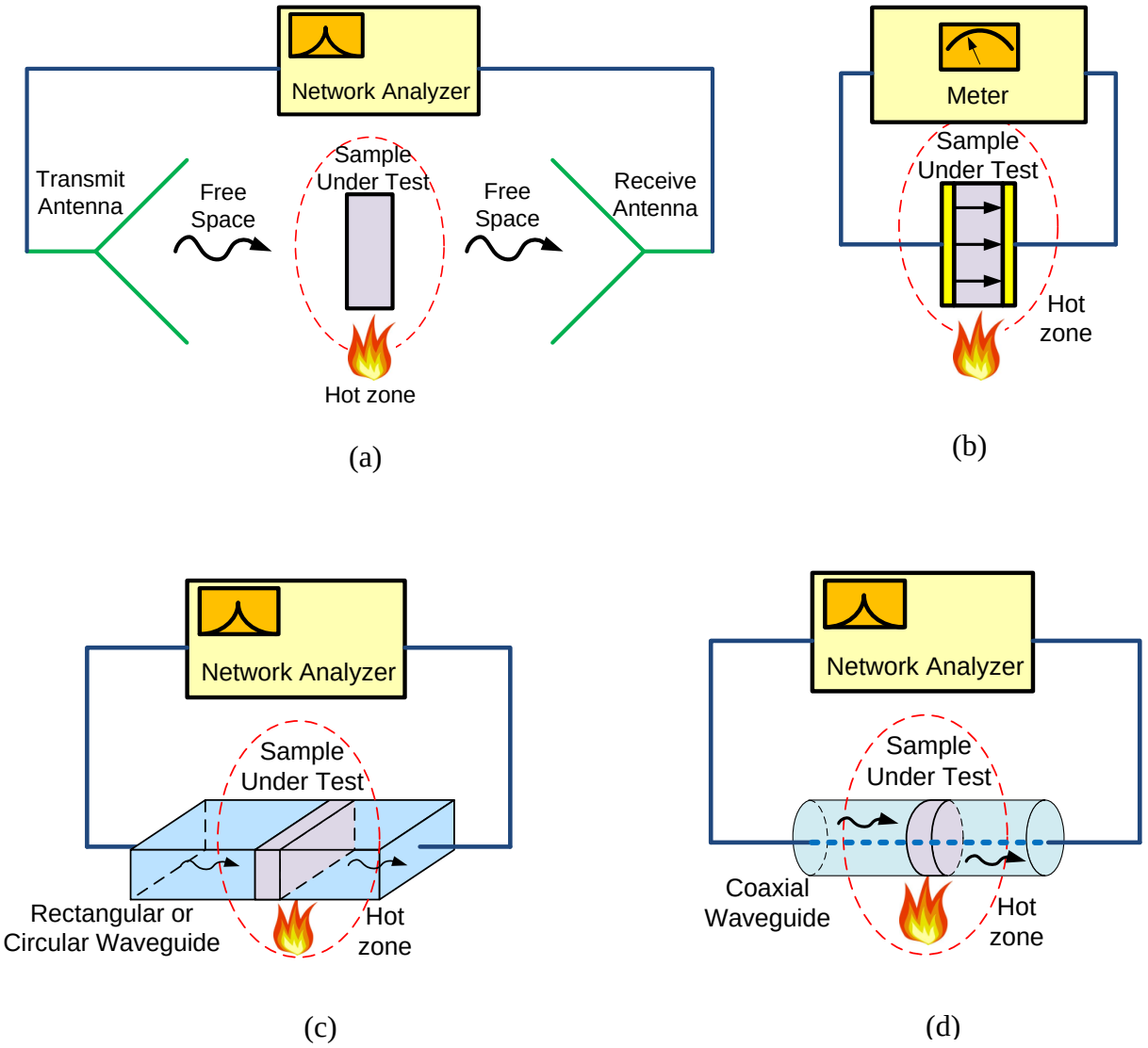

Figure 1.2: Different transmission-based material characterization methods which can be used for high temperature material characterization; (a) free space, (b) capacitive, (c) rectangular / circular waveguide, and (d) coaxial line.

The first category of the characterization methods shown in Fig. 1.2 is based on transmission of an electromagnetic wave between two terminals. The unknown material will be placed in the

middle of this channel and will affect its transmission coefficient accordingly. The simplest demonstration of this concept can be made using free space transmission as shown in Fig. 1.2(a). The electromagnetic wave is sent out and received by two antennas which are connected to a network analyzer [13]. The unknown material is placed in the line-of-sight connecting the two antennas. In order to extract the dielectric properties of the material, the same structure is simulated using commercial full wave electromagnetic simulator software. In the full wave simulation, the dielectric properties of the material are swept in a wide range to match the simulated and measured results. As a result, a set of ε_r and $\tan\delta$ values will be found in simulation which give the same transmission coefficient as the measured one. This will be reported as the dielectric properties of the material at that particular measurement temperature. In order to achieve the material's properties at other temperatures, the sample needs to be heated and the same process should be repeated. The main advantage associated with this method is the physical separation of the measurement ports and antennas with the sample under test, which makes this method attractive for high temperature measurements where proper protection of the measurement devices is a challenge. The drawback associated with the free space method is the requirement of large sample sizes in order to achieve reasonably high measurement accuracy. This makes characterization of small samples almost impossible using this method. This problem becomes more critical for applications in need of tiny material sizes for miniaturized sensor development.

The other transmission based method is parallel-plate or capacitive characterization scheme [14]. As shown in Fig. 1.2(b), the capacitance measured across two parallel plates changes as a dielectric material is inserted between the plates. In this approach, the unknown material will be

placed between two metallic and parallel plates and the capacitance will be measured at each temperature. Using basic circuit theory, the corresponding dielectric constant of the material can be calculated at each temperature. This method is very well suited for thin and flat materials and the involved calculations and data processing are quite simple. On the other hand, the maximum characterization frequency and its accuracy are limited. In addition, the parallel plate method lacks the necessary accuracy in the loss measurement.

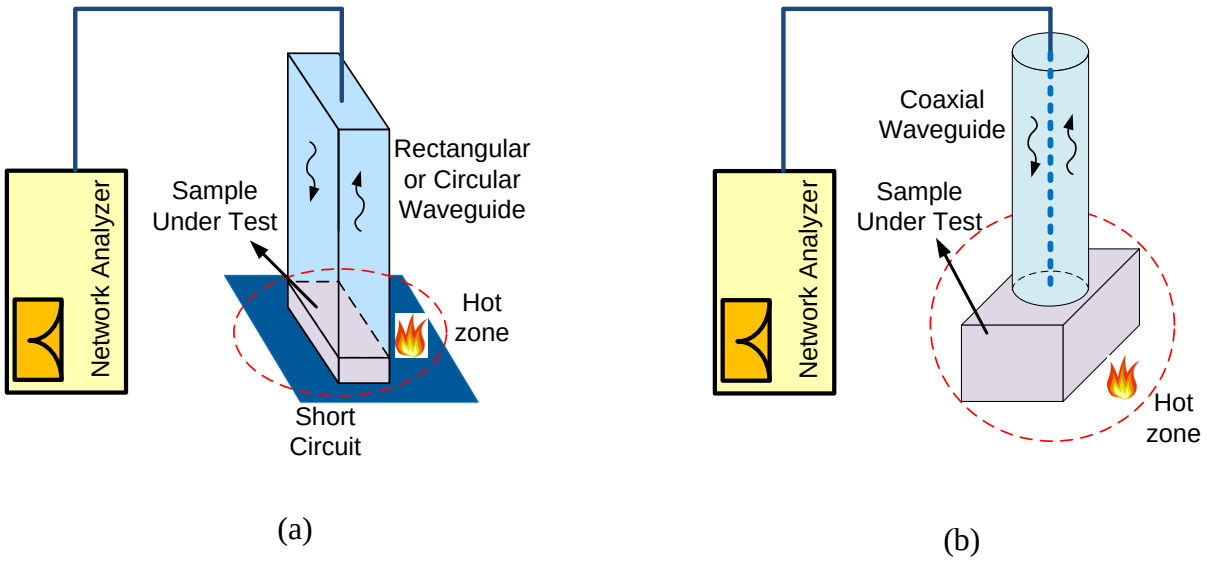

Figure 1.3: Different reflection based material characterization methods which can be used for high temperature material characterization; (a) rectangular/circular waveguide, and (b) coaxial probe.

The last class of transmission based material characterization methods consists of a waveguide which is partially loaded with the unknown material [15]. The two common configurations used in this method are the rectangular/circular waveguides and coaxial lines as illustrated in Fig.

1.2(c) and (d). As for the previous two methods, the transmission coefficient measured at the two ports will be affected by the presence of the material under study. Again, full wave simulations will be used to extract the material properties. This characterization method is simple to implement and analyze. However, it requires precise machining of the material to obtain the exact cross-sectional dimension of the waveguides. In addition, the small air gaps occurring between the material and the waveguide cause measurement uncertainties.

Beyond the transmission based characterizations, the next category of the material characterization methods is based on measuring the reflection coefficient of a waveguide loaded with the unknown material. There are two methods to be discussed in this category. In the first, the waveguide will be closed at one end with an electrically conducting plate and the unknown sample will be placed right before the short circuit as shown in Fig. 1.3(a) [16]. This method is similar in principle to the waveguide transmission method illustrated in Fig. 1.2(c) and has the same benefits and limitations, except for the fact that there will be only one measurement port. However existence of only one measurement port makes this configuration attractive. The other reflection based material characterization method is shown in Fig. 1.3(b) and is referred to as the coaxial probe method [17]. In this method, the sample is placed at one end of an open-ended coaxial line. However, there is no short circuit as previously described for the rectangular/circular waveguide case and the sample is suspended in free space. There are no strict requirements for the sample's dimensions when using this method and it provides more flexibility in characterizing samples with various shapes. However, the air gap between the sample and the probe can be the source for significant measurement errors.

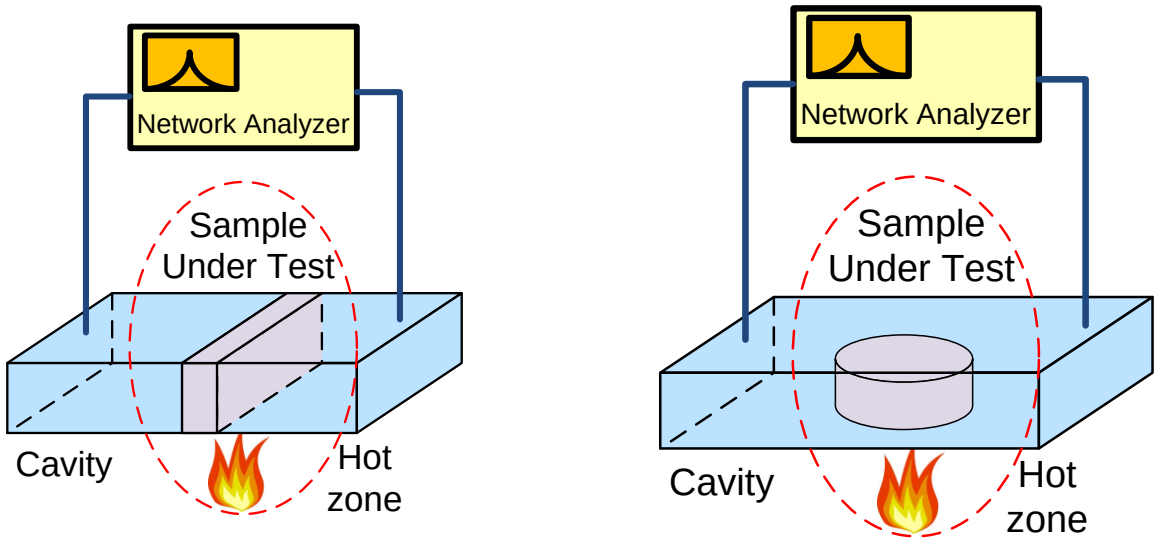

(a) (b)

Figure 1.4: Different resonator based material characterization methods which can be used for high temperature material characterization; (a) rectangular sample with the same cross-section dimension, and (b) cylindrical sample with arbitrary dimensions.

The last category of material characterization methods is illustrated in Fig. 1.4 and is based on a cavity resonator [18][19]. This is the most accurate characterization method which will be described in Chapter 3. This technique is based on a metallic cavity resonator which is coupled to the access ports enabling measurement of its resonant frequency and quality factor. The unknown material is then placed inside the cavity which modifies the aforementioned parameters. Full wave simulations are again used for the extraction of material properties. Being accurate, this method is very well suited for applications in need of precise material properties such as wireless sensors. However, realization of this technique at high temperatures is challenging. In addition, the other drawback associated with this method is its single frequency performance. In

other words, the measurement frequency is predefined by the cavity dimensions and cannot be easily tailored.

1.3 Overview of Dissertation

This dissertation presents the high temperature material characterization method and the design and test of three types of wireless high temperature sensors. Chapter 2 presents the fabrication process of the SiCN materials and the dielectric property at low frequencies. In Chapter 3, a waveguide cavity method is used to characterize the material properties at the room temperature with very high accuracy. The measured dielectric constant of SiCN material using this waveguide cavity method is used to estimate the resonant frequency of the resonator for high-temperature measurement and therefore is used to determine the dimensions of the TRL calibration kit. Chapter 4 presents the design and fabrication of high-temperature characterization setup as well as the TRL calibration kit. The measurement results of the dielectric properties of SiCN ceramics are also shown in the same chapter. In Chapter 5, three different types of sensors, corresponding to different antenna configurations, are designed and the prototypes are fabricated and tested. Finally, the conclusions and future works are described in Chapter 6.

CHAPTER 2 HIGH TEMPERATURE MATERIALS

2.1 SiCN Ceramic Material

SiCN ceramic materials are polymer-derived ceramics (PDCs), which are a new class of materials synthesized by thermal decomposition of polymeric precursors. PDCs possess excellent thermo-mechanical properties up to very high temperatures (> 1500^{o}C), such as excellent thermal stability, high oxidation/corrosion resistance, and creep resistance, thus making them suitable for high-temperature applications [20][21][22][23][24][25][26][27][28][29][30]. They are potential candidates to develop high-temperature MEMS sensors for turbine engines.

2.2 Fabrication Procedure

The amorphous SiCN ceramics can be fabricated through the thermal decomposition of a commercial liquid-phase precursor using the technique reported previously in [31], as shown in Figure 2.1 and Figure 2.2. Precursor is a compound that participates in a chemical reaction that produces other compounds. The one used in this paper is "VL20" which was purchased from KiOH Corporation. First, the precursor is solidified by heat treatment at 250^{o}C for 1 hour, and then being heated at 350^{o}C for 4 hours in a flow of ultra-high-purity nitrogen. The solids obtained from the previous step are then crushed and ball-milled into fine powders using a high-energy ball milling machine. Finally, the powders are compressed in the shape of disc and then pyrolyzed at 1400^{o}C or higher for 4 hours in a tube furnace with the ultra-high-purity nitrogen flowing. The scanning electron microscope (SEM) image shown in Fig. 1.3 reveals the typical microstructure of the pyrolyzed SiCN samples. In order to achieve better dielectric property

(high dielectric constant, low loss tangent) of SiCN materials, boron(B)-doped SiCN ceramics with the different ratios of Si to B are fabricated and characterized in this dissertation.

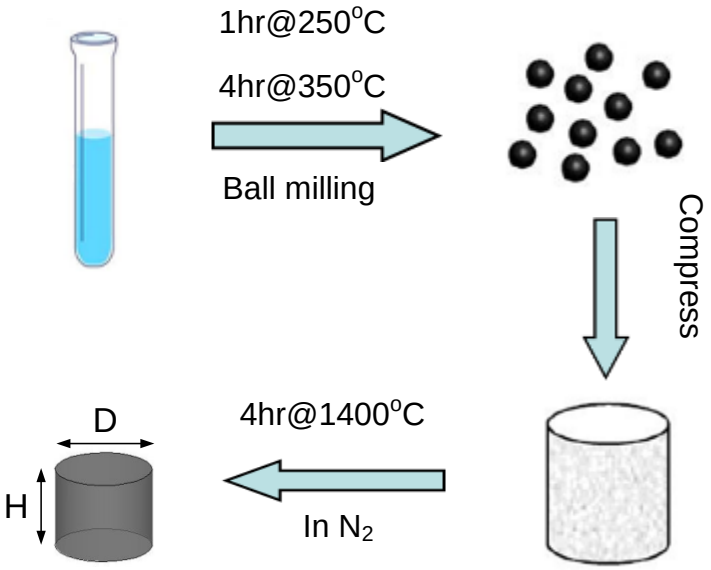

Figure 2.1:Process flow of SiCN ceramics in schematics

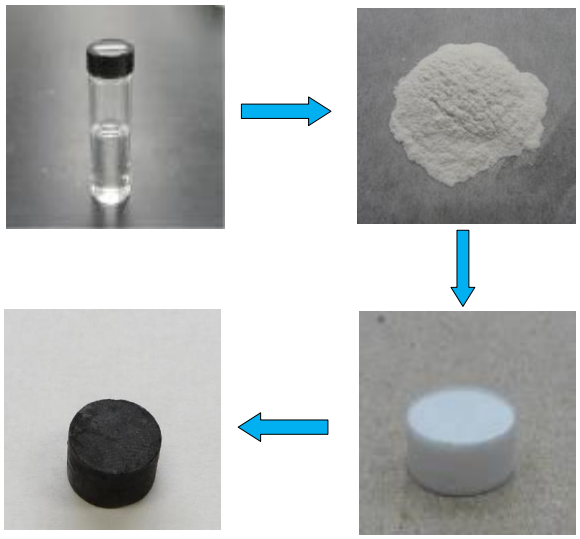

Figure 2.2: Process flow of SiCN ceramics in photos.

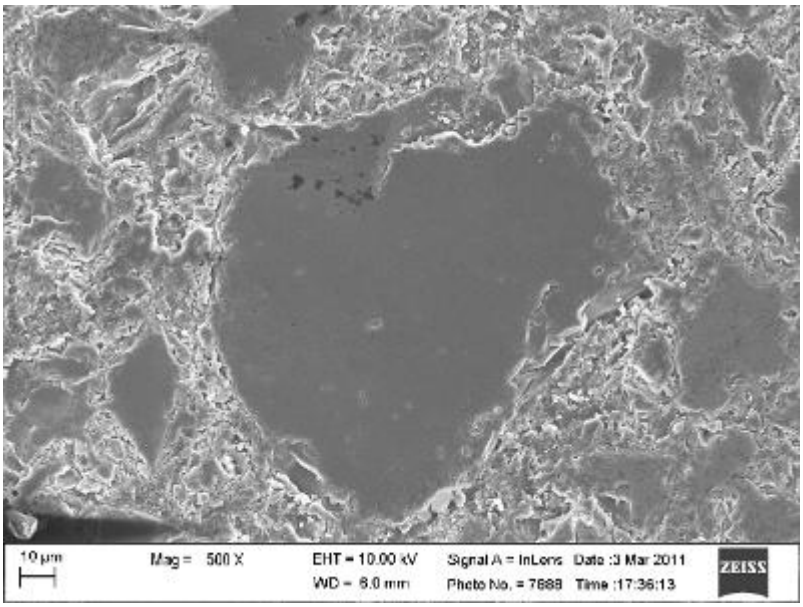

Figure 2.3:Scanning electron microscope (SEM) images of the SiCN material at 500× zoom level.

2.3 Dielectric Property of SiCN at DC and Low Frequencies

Figure 2.4 shows the temperature dependence of dielectric constant and tangent loss of sample SiCN (sintered at 1200^{o}C) measured at frequency of 1, 10, and 100 KHz over temperature range of 20 ~ 675^{o}C, respectively [32]. In general, dielectric constant increases with temperature.

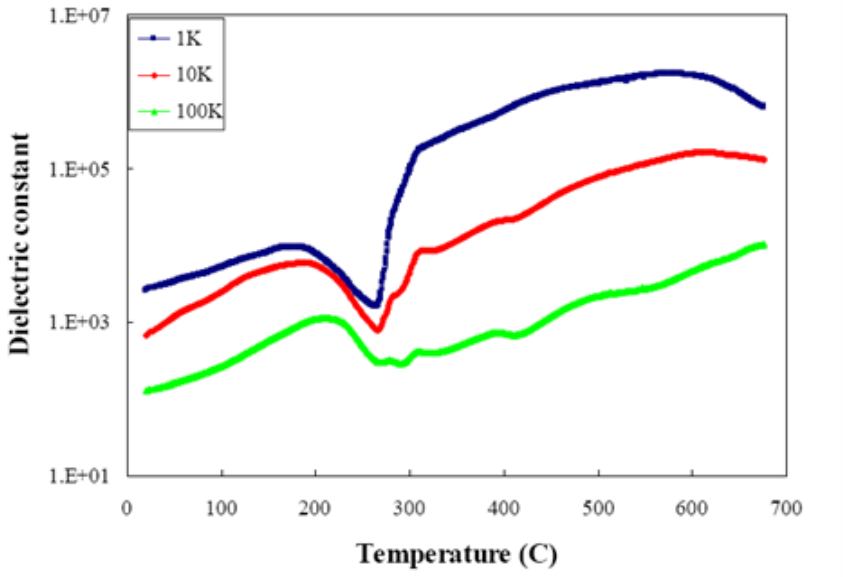

Figure 2.4: Temperature dependence of the dielectric constant of sample SiCN (sintered at 1200^{o}C) measured at frequency of 1, 10, and 100 KHz over temperature range of 20 ~ 675 ^{o}C [32].

2.4 Conclusion

SiCN ceramic materials have been demonstrated to be very stable and corrosion resistant for high temperature, which make them good candidates for high-temperature sensing applications. It was also discovered that their dielectric constant increases with temperature below 1 MHz. However, the proposed wireless passive sensing mechanism requires the use of microwave frequencies for reliable temperature sensing without the need of wire connections and packaging. Therefore, it is highly desired to characterize the dielectric properties of SiCN materials at microwave frequencies which will be used as the carrier frequencies in wireless sensing.

CHAPTER 3 ROOM TEMPERATURE CHARACTERIZATION

3.1 Introduction

As one of the important steps in high-temperature characterization, material properties of SiCN ceramics need to be characterized at room temperature first with high accuracy. There are two main reasons for this study. First, the measurement results at room temperature can provide a reference for the high-temperature characterization. It will be shown later that the measured dielectric properties agree very well for both measurement methods at room temperature. This ensures the validity of the results at other temperatures as well. Second, the room-temperature dielectric properties of SiCN materials will be required to design a custom-made TRL calibration kit to improve the accuracy for the high-temperature characterization.

There are several well-known techniques for characterizing the dielectric constant (ε_r) and loss tangent ($tan\delta$) including the transmission line methods, free-space methods, and cavity methods [19][33][34][35]. Transmission line methods are able to characterize the material properties over a very wide frequency range. However, the loss tangent measurement is usually not accurate enough. Free-space methods require a large sample to avoid edge diffraction and are usually used at millimeter-wave frequencies and above. Perturbation methods using waveguide cavities are easy to derive the dielectric constant and loss tangent. Nevertheless, the limited amount of energy storage within the test samples could cause a poor estimate of the loss tangent, particularly for low-loss-tangent materials. A fully-filled cavity is ideal to characterize the material properties with high accuracy, but it is very difficult to prepare the high-temperature ceramic material samples to fit in the cavity exactly. The resulting air gap between the sample

and cavity can greatly compromise the measurement accuracy. To address the need of characterizing low-loss-tangent materials with high accuracy, a cavity method with the assist of full-wave simulations was presented in [19] and was able to achieve very high accuracy with excellent repeatability. Loss tangent as low as 8×10^{-5} has been measured and independently verified by National Institute of Standards and Technology (NIST). In this work, these high-temperature ceramic materials exhibit both low dielectric constant and low loss tangent in contrast to the high dielectric constant and low loss tangent of the titania ceramics studied in [19]. As a result, dielectric resonator modes used in [19] are not visible for the materials studied herein. An alternative resonant mode is used to characterize the dielectric constant and loss tangent in this chapter.

3.2 X-band Adapter Cavity Characterization

3.2.1 Characterization Setup

The measurement setup is illustrated in Figure 3.1. Ceramic samples are placed inside a metallic waveguide cavity. The dimensions of the waveguide cavity are 53.71 mm by 22.78 mm by 10.08 mm. A Rogers Duroid 5880 spacer (11.20 mm in diameter and 0.8 mm in height, ε_r = 2.2, $tan\delta$ = 0.0009) is used to elevate the ceramic samples. It was found in [19] that the sensitivity of the resonant frequency and unloaded Q factor (Q_U) caused by the air gap between the ceramic samples and the bottom of the cavity is very high if no spacer is used. This cavity is weakly coupled by two open-ended coax connectors [36].

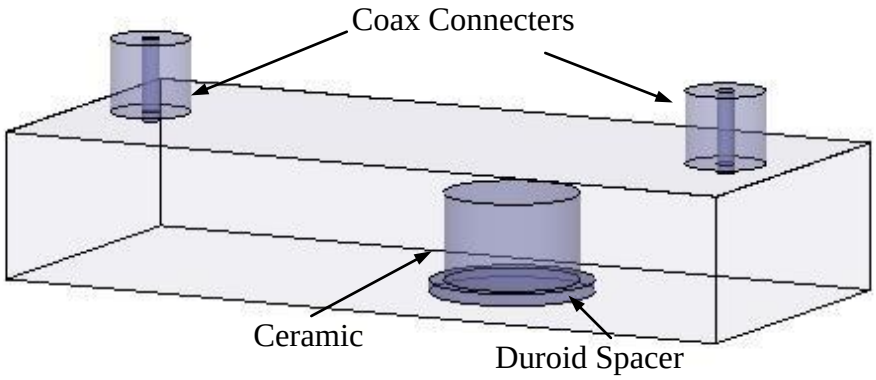

Figure 3.1: Measurement setup for SiCN sample.

First, the resonant frequency and Q_U of the lowest mode of the empty waveguide cavity are measured to be 7.127 GHz and 3,216, respectively. Therefore, the effective conductivity of the waveguide cavity wall is found to be 1.178×10^7 S/m by performing full-wave Ansoft High Frequency Structure Simulator (HFSS) simulations. This effective conductivity will be used in the simulations of the loaded cavity. In [19], dielectric resonator (DR) modes were used since these modes maximize the amount of energy storage inside the test samples, consequently maximizing the measurement accuracy. The resonant peaks for a SiCN sample are measured using an Agilent performance network analyzer (N5230A) and shown in Figure 3.1. To match these measured resonant peaks, a parametric sweep of dielectric constants is performed in HFSS. A good agreement is found between simulation and measurement results. In order to identify the resonant modes of these peaks, electric field distributions of different modes are simulated in HFSS and presented in Figure 3.2 using the dielectric constant found in the parametric sweep. Both driven mode and eigen mode simulations are performed. It is found that the first DR mode

occurs at 11.684 GHz in the eigen mode simulation. However, this mode is not visible in both driven mode simulations and measured results. This is due to the fact that DR modes can well confine the energy within the sample, causing a very low energy transfer at these modes. In addition, as observed in Figure 3.1, there are two strong transmission peaks at 10.050 GHz and 11.938 GHz, respectively. The transmission peak of the DR mode at 11.684 GHz could possibly be inundated by the two adjacent strong peaks.

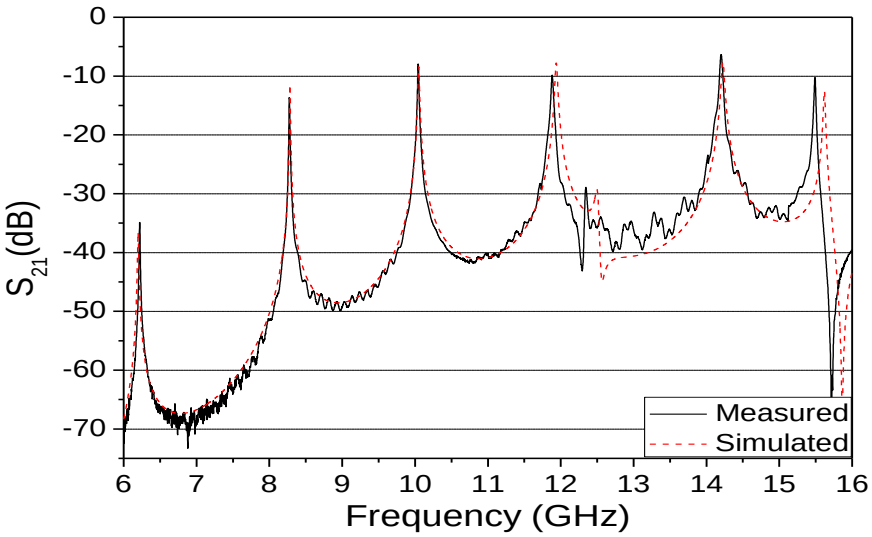

Figure 3.2: Measurement result for SiCN sample.

In order to minimize the uncertainty of characterizing the permittivity of the ceramic materials, maximal energy storage inside ceramic samples is desired. Therefore, the volume fraction (V_f) of each resonant mode needs to be identified. V_f is the percentage of energy stored inside the samples [37]. The waveguide cavity mode with the highest volume fraction (V_f) of the electric

field inside the sample was chosen to achieve the best measurement accuracy. The following relation exists between V_f and different quality factors:

$$\frac{1}{Q_U} = \frac{1}{Q_d} V_{fd} + \frac{1}{Q_s} V_{fs} + \frac{1}{Q_m} \tag{3.1}$$

where Q_U is the unloaded Q factor of the cavity loaded with the sample, Q_d is the inverse of loss tangent of the material to be characterized, Q_s is the inverse of the loss tangent of the materials for the spacer, Q_m corresponds to the metal loss of the cavity, V_{fd} is the volume fraction inside the measured sample, and V_{fs} is the volume fraction inside the spacer. An eigen mode simulation with just the loss tangent of the ceramic sample specified is performed to give a Q_U. The inverse of the product of this Q_U and the specified loss tangent is equal to V_f.

Driven Mode Simulation

6.198 GHz

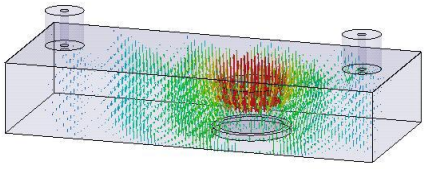

8.284 GHz

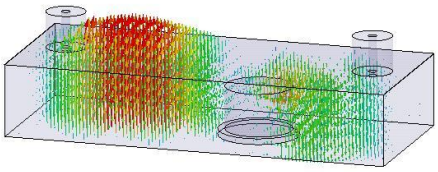

Eigen Mode Simulation

6.212 GHz

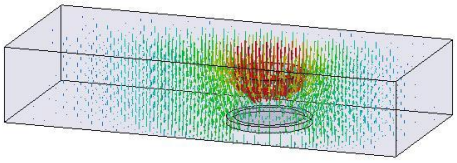

8.298 GHz

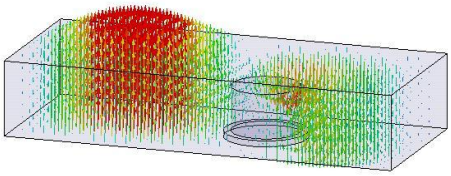

10.050 GHz

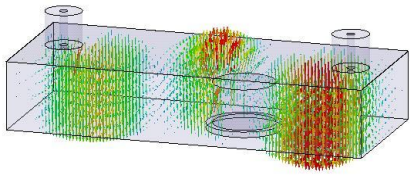

10.070 GHz

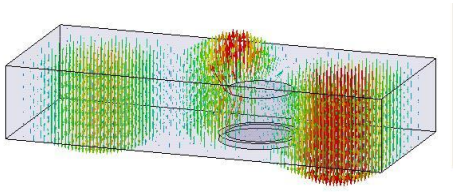

11.684 GHz

NO Visible Coupling

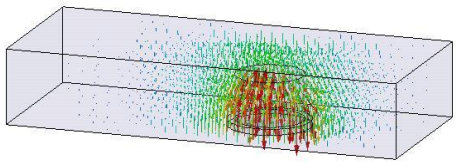

11.938 GHz

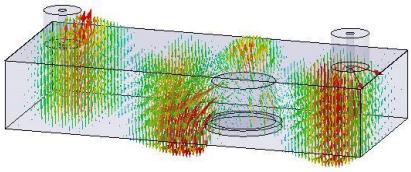

11.958 GHz

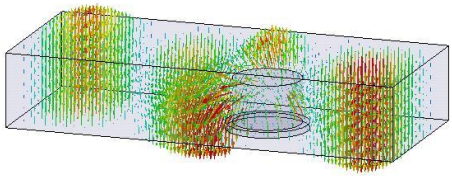

Figure 3.3: E field of the first five resonant modes for the SiCN sample

The geometrical dimensions of the SiCN sample are 4.64 mm in diameter and 5.97 mm in height. The V_f of the first four resonant modes for the SiCN sample are listed in Table 3.1. It is apparent that the first mode of both samples has the largest V_f. As a result, the first mode is used for the analysis in the next section.

Table 3.1: V_f of different modes for SiCN sample

Mode	Freq. (GHz)	V_f
1	6.212	22.4%
2	8.298	5.1%
3	10.070	11.9%
4	11.958	19.2%
5		

3.2.2 Measurement Results

The measured resonant frequencies and Q_U of the SiCN sample are listed in Table 3.2. Three independent measurements are performed to verify the measurement repeatability. The ε_r and *tanδ* of the SiCN sample are obtained by parametric sweeps in HFSS to match the measurement results with the material properties of the waveguide wall and spacer specified.

The average and standard deviation for both ε_r and *tanδ* are shown in Table 3.3. The calculated ε_r of the SiCN sample is 4.358 with a 0.58% standard deviation, demonstrating a very consistent measurement. The *tanδ* is found to be 5.26×10^{-3} with a standard deviation of 5.72%, which is very good since a larger variation in the Q measurement is normally expected.. A summary of the measured material properties of the SiCN ceramic material is listed in Table 3.

The accurate estimation of the dielectric constants of these high-temperature ceramic materials is critical for the design of temperature sensors for turbine engines. The low loss tangents of both

materials are important to achieve high-Q resonances which ultimately determine the sensitivity and sensing range of the sensor systems.

Table 3.2: Summary of results for SiCN

No.	Resonant Freq.(GHz)	Q_U	ε_r	tanδ (10^{-3})
	SiCN			
1	6.218	691.9	4.387	4.91
2	6.225	668.2	4.340	5.41
3	6.224	664.9	4.347	5.45

Table 3.3: Average and standard deviation (σ) of ε_r and $tan\delta$

Material	Avg. ε_r	σ (ε_r)	Avg. tanδ (10^{-3})	σ (tanδ)
SiCN	4.358	0.58%	5.26	5.72%

3.3 Ku-band Adapter Cavity Characterization

This section improves the waveguide cavity characterization method proposed in previous section by further increasing V_{fd} and optimizing the spacer design to achieve better measurement accuracy. In [19], although two *H*-band coax-to-waveguide adaptors were used to form the cavity for characterization, V_{fd} was still large because of the high dielectric constant of test samples. In the previous section, two *X*-band coax-to-waveguide adaptors were used. In this section, two K_u-band adaptors are employed to increase V_{fd} from 22.4% to 33.4% for the same

sample material and size. There are different electric field distributions for different resonance modes. This results in V_f different for each resonant mode. The dielectric constants of the test sample also affect V_f. For the same size of the samples, a higher dielectric contrast results in a higher V_f since the field is more tightly constrained within the test dielectric sample. The K_u band adaptor cavity is smaller than *X*-band adaptor cavity, so for the same resonant mode there is more electric field energy in the test sample. In addition, the resonant frequency corresponding to the waveguide cavity mode of interest, increases from 6.22 to 7.899 GHz, which is much closer to the resonant frequency of the dielectrically-loaded cavity resonator used for the high-temperature characterization. To reduce the measurement uncertainty caused by the spacer, a hollow ring shape is adopted to minimize V_{fs} while maintaining the mechanical support of the ceramic sample. Since SiCN materials exhibit dielectric constants around 3-5, the electric field confinement inside the SiCN sample is not as concentrated as in the Titania cases. The dielectric constant of porous Titania varies from 12 to 90 [19]. Because of the ring spacer's hollow structure, less electric field energy is concentrated in it, compared with the solid spacer, and the V_f of the ring spacer is smaller. Therefore, the V_f of the test sample is larger for the ring spacer case and the measurement uncertainty decreases. In addition, according to the datasheet from the vendor, the dielectric constant of materials used for spacer is in the range of from 2.18 to 2.22, however, in the simulation, the mean value of the dielectric constant, 2.2, was used. Therefore, it involves the error for the characterization. The spacer in the shape of ring reduces the size of the spacer compared with a solid spacer, so the measurement uncertainty is reduced, too. Therefore, the adverse effects from a solid spacer are more pronounced compared with the Titania cases. This ring-shaped spacer design can provide near-air supporting structure underneath the material

sample, and therefore represents an optimized design. It should be noted that RT/Duroid 5880 is chosen here again for its low dielectric constant of 2.2 and low loss tangent of 0.0009.

3.3.1 Characterization Setup

Figure 3.4: Illustration of the waveguide cavity method. For 5880 measurement, D_s=14; H_s= 3.19; D_{i_r}=8; D_{o_r}=9; H_r=3.19. For SiCN measurement, D_s=9.29 H_s= 6.26; D_{i_r}=6; D_{o_r}=7.08; H_r=0.08 (unit: mm).

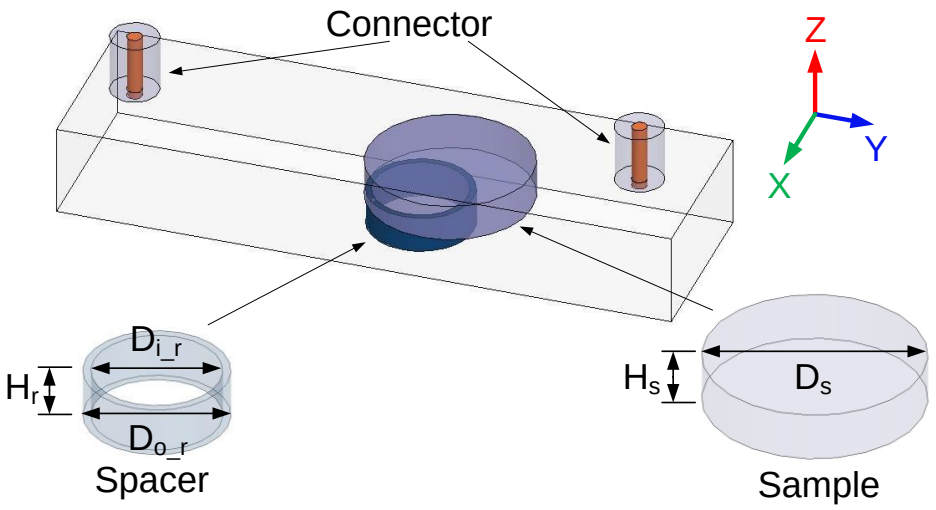

Figure 3.4 illustrates the characterization setup, which is consisted of a metallic waveguide cavity loaded with the to-be-measured sample. The corresponding measurement setup is shown in Fig. 3.5. As shown in Figure. 3.5, two K_u-band coax-to-waveguide adaptors are assembled together to form a waveguide cavity with dimensions of 52.46×15.74×7.86 mm^3. The dimensions of the samples and spacers are shown in Figure 3.4. The cavity is weakly excited by two coaxial probes. The cylindrical sample is elevated using a ring-shaped spacer. The dielectric constant and loss tangent of the material under study can be extracted from the measured

resonant frequency f_{r_w} and unloaded Q factor Q_{U_w} of the cavity containing the sample, with the assist of Ansoft High Frequency Structure Simulator (HFSS) full-wave simulation software package. The eigen-mode simulation is used for the dielectric property extraction. The number of tetrahedra for meshing the simulated structure is more than 40,000 and the ΔS for the convergence criteria is less than 0.0005.

Figure 3.5: Waveguide cavity method setup. View of (a) the half cavity at the assembly plane and (b) the whole cavity after assembly.

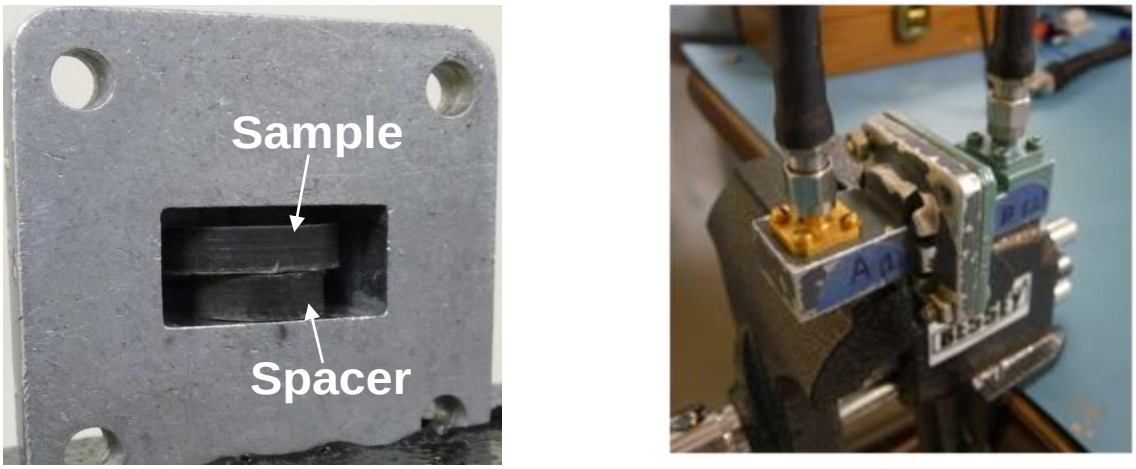

(a) (b)

The measurements of two materials, i.e. RT/Duroid 5880 and SiCN, are performed using this improved waveguide cavity method at room temperature. The size of SiCN samples is restricted by the molds used in fabrication and is also affected by the different fabrication process, such as sintering temperature, time, and other experimental parameters. The dimensions of the SiCN samples for characterization are about 10 mm in diameter and 5 mm in height. The ring spacer

should be large enough to elevate the test sample in the middle of the cavity in the z direction and the sidewall should be as thin as possible to reduce the electric field concentration inside the spacer. The size of RT/Duroid 5880 samples as shown in Fig. 3 is in the range of the size of SiCN sample. Its V_f is smaller than SiCN case. Therefore, the accuracy for the SiCN characterization is not less than that for RT/Duroid5880 characterization.

3.3.2 Measurement Results

To verify the measurement accuracy of the improved waveguide cavity method, RT/Duroid 5880 material is characterized, which represents a challenging case for its low dielectric constant of 2.2±0.02 and low loss tangent of 0.0009. Ten independent measurements are performed to identify the measurement consistency. The average extracted ε_r and $\tan\delta$ are 2.18 and 0.0008, which match the nominal values very well. The standard deviations for ε_r and $\tan\delta$ are 0.10% and 3.61%, respectively, which are much better than 0.58% and 5.72% presented in the previous section. The Type A experimental uncertainties for for ε_r and $\tan\delta$ are 0.001 and 0.00001, respectively, based on the statistical analysis in [38]. This is primarily attributed to the increased V_{fd} and improved spacer design which corresponds to reduced V_{fs}.

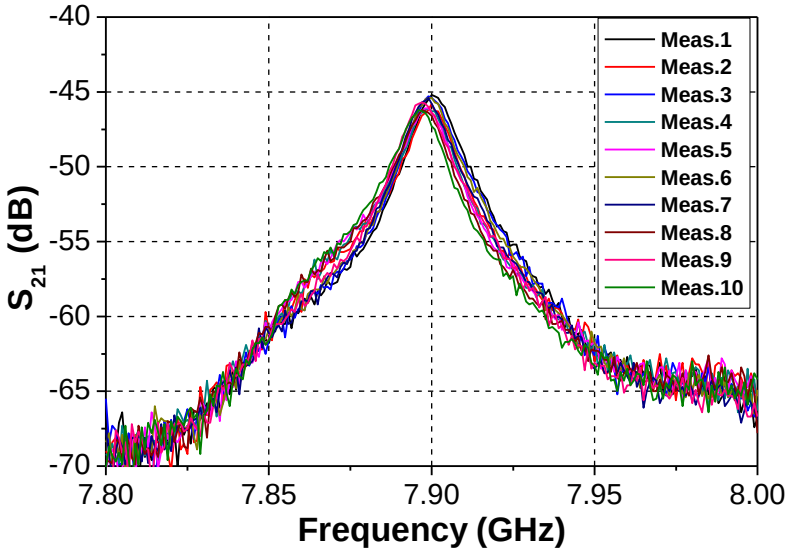

Figure 3.6: S_{21} results of 10 measurements for SiCN sample characterization.

Table 3.4: Measured f_{r_w}, Q_{U_W} and extracted ε_r, $tan\delta$ with standard deviations (σ) and uncertainty (s_u) using waveguide cavity method at room temperature

Measured Sample	f_{r_w} (GHz) (σ) (s_u)	ε_r (σ) (s_u)	Q_{U_w} (σ) (s_u)	tanδ (σ) (s_u)
5880	9.1126 (0.01%) (0.0004)	2.182 (0.13%) (0.001)	2292 (1.20%) (11)	0.00082 (3.61%) (0.00001)
SiCN	7.8989 (0.03%) (0.0006)	3.655 (0.13%) (0.001)	540 (2.15%) (3)	0.00408(2.16%) (0.00002)

The same measurement and simulation process is performed for the SiCN material. The dimensions of the SiCN sample and spacer are shown in Fig.3.4. Again, 10 independent measurements are performed. Fig. 3.6 shows S_{21} results for these measurements. The average extracted ε_r and tanδ are 3.655 and 0.00408, respectively. The standard deviations for ε_r and tanδ

are 0.13% and 2.16%, respectively, which are again much better than the results in X-band cavity characterization. The Type A experimental uncertainties for deviations for ε_r and tanδ are 0.001 and 0.00002, respectively,The measurement results as well as extracted complex permittivity for both materials are summarized in Table 3.4. It is noted that this waveguide cavity approach can provide very high measurement accuracy; however, it cannot be easily extended for high-temperature measurements. A new characterization method which is specifically designed for high-temperature characterization of dielectric materials at microwave frequencies will be presented in the next section. This method requires relatively small sample sizes and can be tailored to different microwave frequencies with high measurement accuracy.

3.4 Conclusion

The dielectric properties of SiCN ceramic materials have been characterized at microwave frequencies using an accurate measurement technique based on cavity resonator and full-wave simulations. This material property information serves as a basis to develop wireless passive ceramic MEMS high-temperature sensors for turbine engines. It is noted that this waveguide cavity approach can provide very high measurement accuracy; however, it cannot be easily extended for high-temperature measurements. A new characterization method which is specifically designed for high-temperature characterization of dielectric materials at microwave frequencies will be presented in the next chapter. This method requires relatively small sample sizes and can be tailored to different microwave frequencies with high measurement accuracy.

CHAPTER 4 HIGH TEMPERTURE CHARACTERIZATION

4.1 Introduction

SiCN is stable and corrosion resistant at high temperatures with temperature-dependent permittivity at low frequecies. These advantages make SiCN a suitable candidate for high temperature wireless sensor development. However, the wireless passive sensing mechanisms require the use of microwave frequencies for reliable temperature sensing without the need of wire connections and packaging. Therefore, it is necessary to characterize the dielectric properties of SiCN materials at microwave frequencies and high temperatures, which will be used as the carrier frequency in wireless sensing. In addition, this measurement setup can be easily adapted for wireless passive sensing.

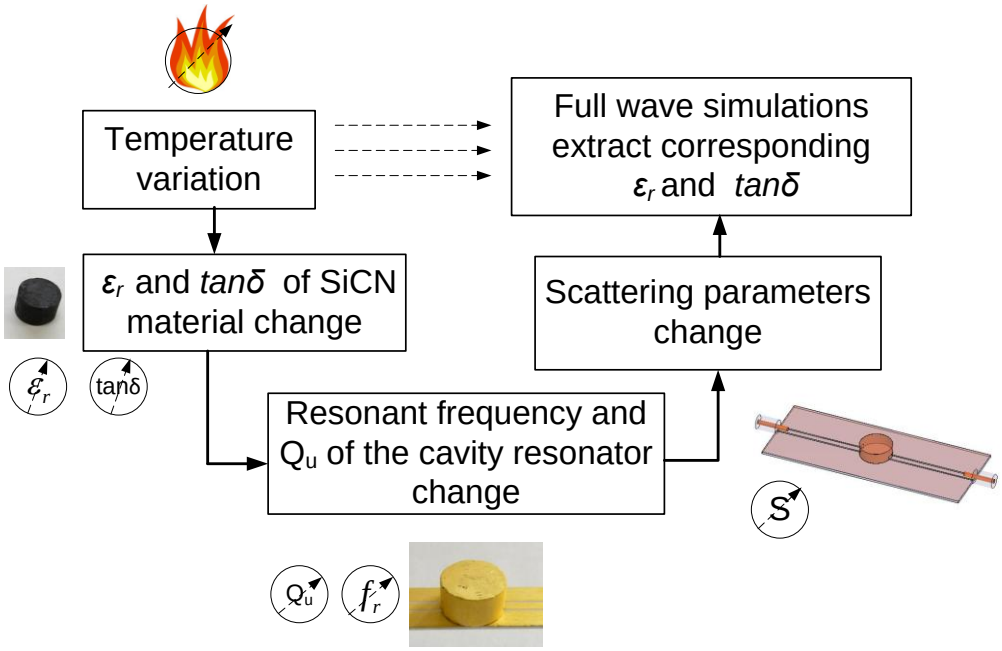

Figure 4.1: Flowchart of the high temperature characterization mechanism.

4.2 Proposed High-Temperature Characterization Method

Fig. 4.1 illustrates the mechanism behind the high-temperature characterization setup which is shown in Fig. 4.2. The dielectric material under study is first metalized to form a dielectrically-loaded cavity resonator. The material could take any shape. In this paper, a cylindrical form is used. Two opening slots are required to allow the transmission of microwave signal through the resonator. The resonator is then placed over short-ended CPW lines. The CPW line and resonator are weakly coupled through the aforementioned slots. The resonator and CPW line are simply in contact without glue. Because the contacting surfaces of the resonator and CPW line are very flat, this connection can still achieve the desired coupling level. Moreover, only f_r and Q_u which are not very sensitive to the level of S_{21} are used for the extraction of the dielectric properties of the test materials. SMA connectors are connected to the CPW lines. The substrate material used for the CPW line is alumina. Extracting dielectric properties is the inverse process. First, The scattering parameters of the described setup are measured at various temperatures. Then, the resonant frequencies and unloaded Q factors of the resonator with the test sample can be extracted from the measured S results. The next step is to use the full simulation tool HFSS to extract the dielectric constant and loss tangent of the test sample. The parametric sweeps of dielectric constants and loss tangent of the test sample are performed using HFSS to match the measured resonant frequency and unloaded Q. Finally, when the simulated resonant frequency and unloaded Q are the same to the measurement results, the dielectric constant and loss tangent of the material under study are extracted.

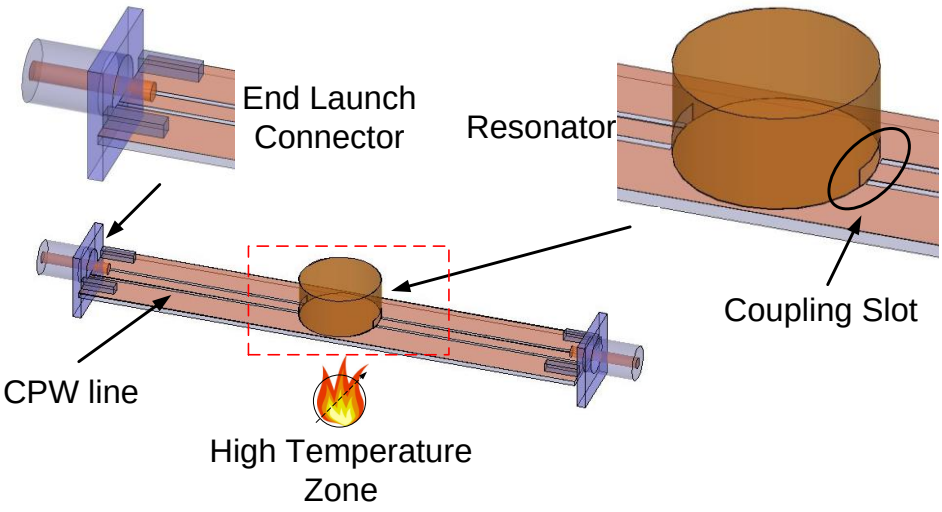

Figure 4.2: Illustration of the high temperature characterization method

The resonant frequency (f_r) and Q of the TM_{010} mode inside the dielectrically-loaded cavity resonator can be calculated using the following equations [39]:

$$f_r = \frac{1}{2\pi\sqrt{\mu_0\varepsilon_0\varepsilon_r}}\frac{\chi_{01}}{\frac{D}{2}} \tag{4.1}$$

$$Q_U = \left(\frac{1}{Q_{dielectric}} + \frac{1}{Q_{metal}}\right)^{-1} \tag{4.2}$$

$$Q_{dielectric} = \frac{1}{tan\delta} \tag{4.3}$$

$$Q_{metal} = \frac{\chi_{01}\sqrt{\frac{\mu_0}{\varepsilon_0\varepsilon_r}}}{2\left(1+\frac{D/2}{H}\right)\sqrt{\frac{2\pi f_r\mu_0}{2\sigma}}} \tag{4.4}$$

where ε_0 and μ_0 are the permittivity and permeability of free space. χ_{01} is the first root of Bessel function of the first kind $J_0(z)$, i.e. 2.2048, and σ is the bulk conductivity of the metal. In this study, gold is used for metallization purpose with $\sigma = 4.1\times10^7$ S/m. D and H represent the diameter and height of the cavity. ε_r and tanδ are the dielectric constant and loss tangent of the dielectric material, respectively.

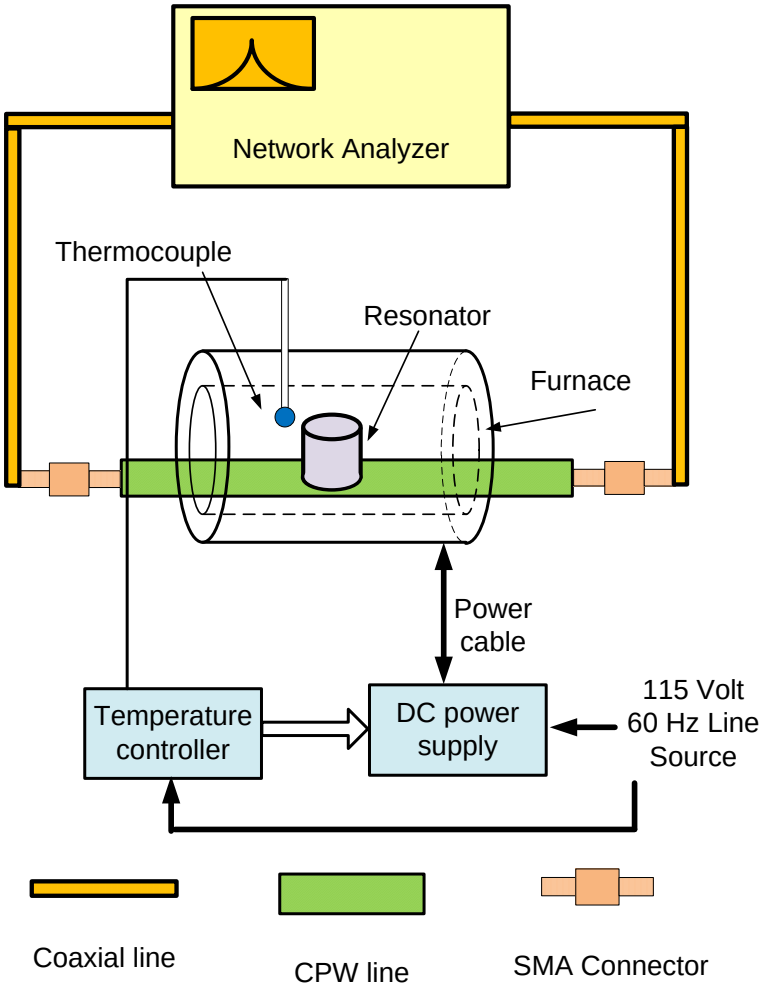

Figure 4.3: The proposed high temperature material characterization setup.

In Chapter 1, different material characterization techniques have been described. It was shown that some of the methods benefit from being simple and easy to implement, while others provide higher accuracy. In addition, in order to use any of those methods to characterize materials at extremely high temperatures for turbine applications, careful considerations need to be made. The "*hot zone*" illustrated in Figs. 1.2 to 1.4 is an abstract concept which needs to be properly realized. The physical realization of this hot zone should not overheat the measurement facilities including the connectors, cables and the network analyzer. In addition, stable temperature at the vicinity of the sample is required. Therefore, the heating element in the measurement apparatus should occupy a substantial portion of the furnace to mitigate fast temperature fluctuations. The other issue to be considered is the temperature control loop. There should be direct access to the sample in order to monitor its real temperature during the measurement. This requires the measurement setup to provide access to the sample under test while maintaining a stable local temperature, which is a challenging task, as such access generally exposes the measurement environment to the external environment.

To achieve the aforementioned requirements at the same time, the characterization setup is presented as illustrated in Fig. 4.3. A CPW transmission line is loaded with a cavity resonator in the middle and passes through a cylindrical ceramic furnace. There are a number of advantages associated with this setup. Using a transmission line alleviates any reliance on fully-confined measurement chambers, allowing for realization of a relatively large hot zone compared with the sample size. In addition, the open ends of the furnace provide proper access to the sample in order to monitor the local temperature at the resonator using a thermocouple. Use of CPW configuration as the transmission line enables real time observation of the sample which is not

possible in the closed environment of a rectangular/circular waveguide or coaxial line. In addition, the proposed configuration provides reasonable high temperature gradient outside the hot zone to protect the measurement facilities.

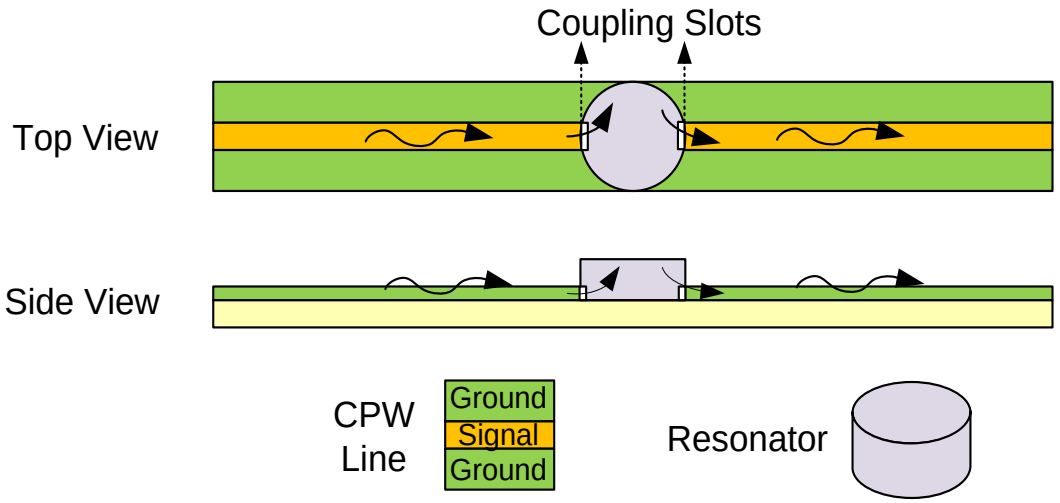

Figure 4.4: Details of the proposed material characterization mechanism including a CPW line loaded with a cavity resonator.

Fig. 4.4 shows more details about the presented characterization method. The CPW line consisting of the dielectric layer, signal and ground lines is illustrated. The cavity resonator is formed by metalizing the material under test. Two small slots are opened at the sidewalls of the cavity to enable coupling of the signal into and out of the resonator. The resonant frequency and quality factor of the cavity can be consequently measured at the two ports of the CPW line. These parameters are functions of the dielectric properties of the unknown material inside the cavity at the operating temperature. After measuring the resonant frequency and quality factor of the resonator, full wave simulations are employed to extract the corresponding dielectric

properties of the material under study. The materials to be characterized here is silicon carbon nitride (SiCN) without and without boron doping (SiBCN) developed at UCF. SiCN is stable and corrosion resistant at high temperatures with temperature-dependent permittivity. These advantages make SiCN a suitable candidate for high temperature wireless sensor development. However, before being able to utilize SiCN in the sensor development, the material needs to be characterized at different temperatures. To do so, two different metallization processes are implemented for the measurements with the highest temperatures of 500^{o}C and 1300^{o}C, respectively.

4.3 Characterization Up to 500^{o}C

4.3.1 Measurement Setup Design

It is noted that to design a dielectrically-loaded cavity resonator, dielectric properties of the material need to be identified first. The measured SiCN material properties using the cavity method presented in the previous section, i.e. ε_r = 3.65 and tanδ = 0.005, are employed here to achieve this goal. f_r and Q_U for the enclosed cavity are calculated to be 12.77 GHz and 189.2, respectively. However, as the cavity is coupled to the CPW lines through the slots, its f_r and Q_U will change. In addition, the temperature not only modifies the f_r and Q_U but also affects the transmission level. Therefore, a parametric study to show the effect of coupling slot dimensions on f_r, Q_U, and transmission level is necessary. The full-wave simulations are performed with reference planes at the coaxial connectors.

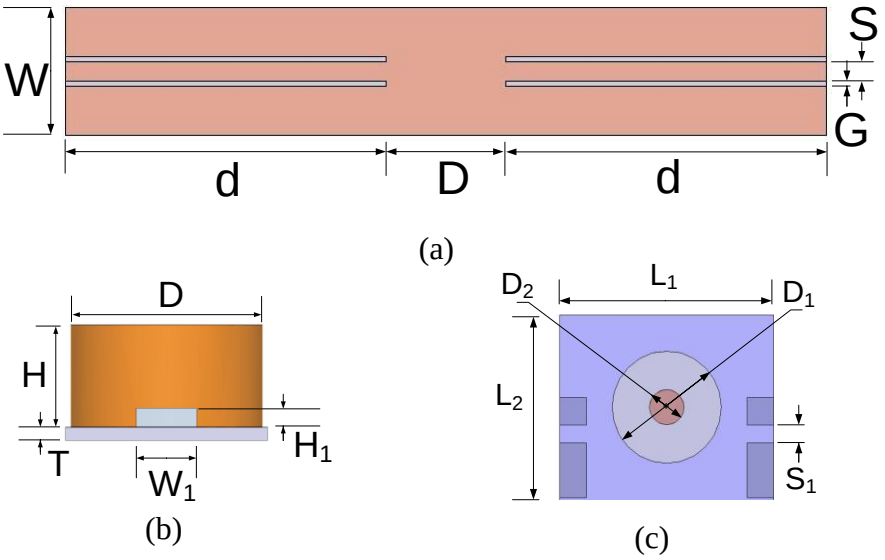

Figure 4.5:: Dimensions of (a) CPW line. (b) fabricated SiCN cavity resonator and (c) connector. S = 1.5; G = 0.4; W = 10; T = 0.635; d = 70; D = 9.41; H = 5.01; H_1 = 1; W_1 = 3; L_1 = 9.5; L_2 = 7.92; D_1 = 3.9; D_2 = 0.76; S_1 = 0.81. (unit: mm).

Fig. 4.6 (a) shows the f_r corresponding to the peak in the simulated S_{21} for different slot dimensions. The f_r changes from 12.23 to 12.87 GHz for different combinations of slot widths (2-4 mm) and heights (0.2-2 mm). It is observed that as the slot width or height increases, the f_r decreases. Additionally, higher sensitivity to the slot size is observed at larger dimensions.

Q_u of the cavity can be extracted from the measured loaded Q (Q_L) using [40]:

$$Q_u = \frac{Q_L}{1 - |S_{21}|} \tag{4.5}$$

where $|S_{21}|$ is the value of S_{21} in linear at the resonant frequency.

As seen in Fig. 4.6(b), smaller Q_u is achieved for larger slot sizes. Again, higher sensitivity to the slot size is observed at larger dimensions.

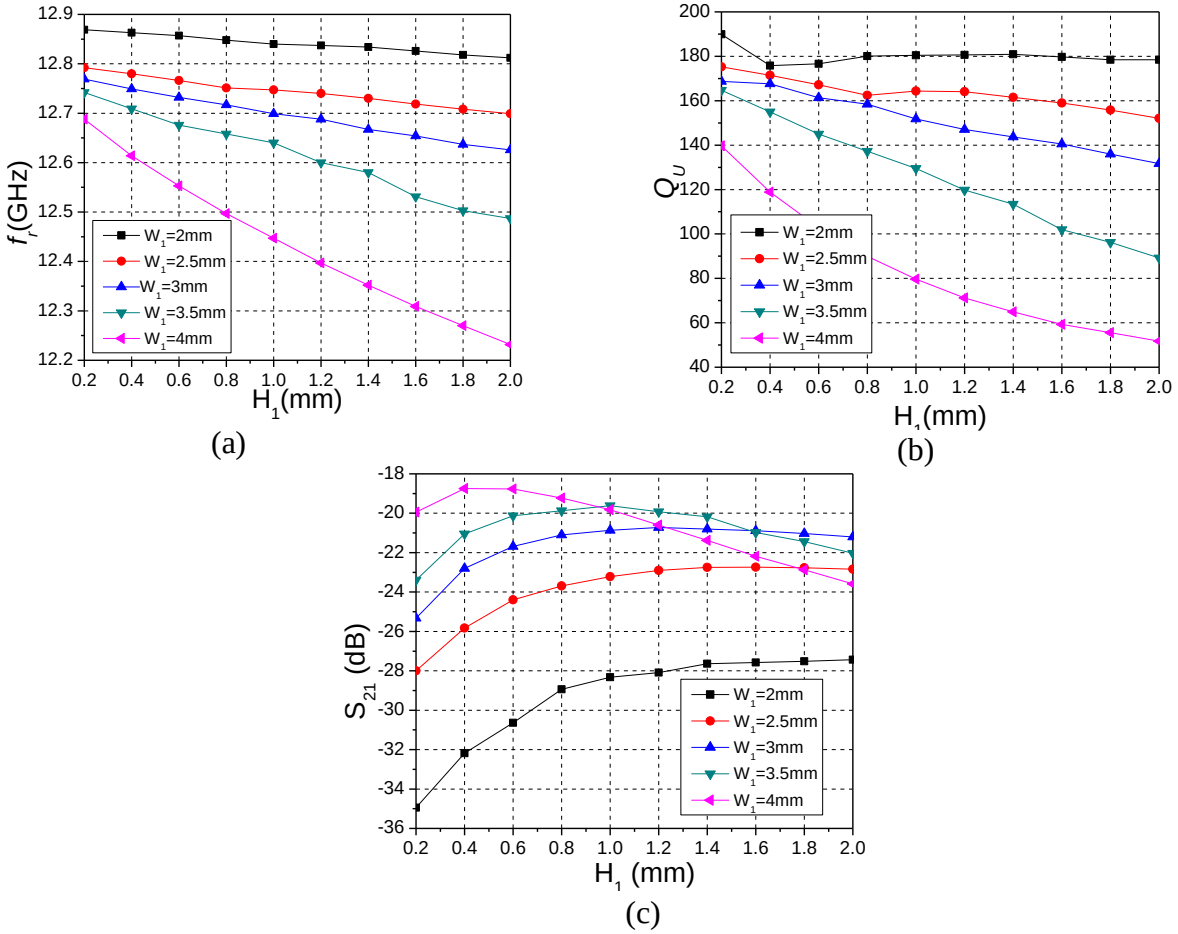

Figure 4.6: Effect of the coupling slot dimensions on (a) resonant frequency, (b) unloaded *Q*, and (c) transmission level.

Fig. 4.6(c) shows the peak level of the simulated S_{21} for different slot dimensions. In general, larger slot dimensions produce higher transmission levels. However, this trend does not hold when W_1 is above 3.5 mm.

Since the transmission level decrease with rising temperatures which will be shown later, maximum transmission level is desired at room temperature. From Fig. 6(c), it is observed that the slot width should be more than 3 mm to have a transmission level around -20 dB. Fig. 8(b)

suggests smaller width for higher Q_u. Therefore, W_1 and H_1 are chosen to be 3 and 1 mm, respectively, by trading off between performance and sensitivity. The simulated f_r and Q_u of the resonator as shown in Fig. 4.5 with the aforementioned slot dimensions are 12.70 GHz and 151.8, respectively.

4.3.2 TRL Calibration Kit

In order to keep the connectors at low temperatures without damaging the cables connected to the network analyzer when the sample is heated to high temperatures, the length of the alumina board should be above 14 cm, which is based on the dimensions of the furnace used for characterization. Short-Open-Load-Through (SOLT) calibration was carried out at the reference planes of the SMA connectors. The measurement results revealed undesirable ripples and excessive losses which came from the long transmission lines and the transitions between the connectors and alumina board. In order to remove the undesirable effects from the long CPW line and achieve better accuracy, custom-made TRL calibration standards are designed and fabricated, similar to the approach used by NASA for high-temperature characterization on Sapphire and Alumina substrates [41].

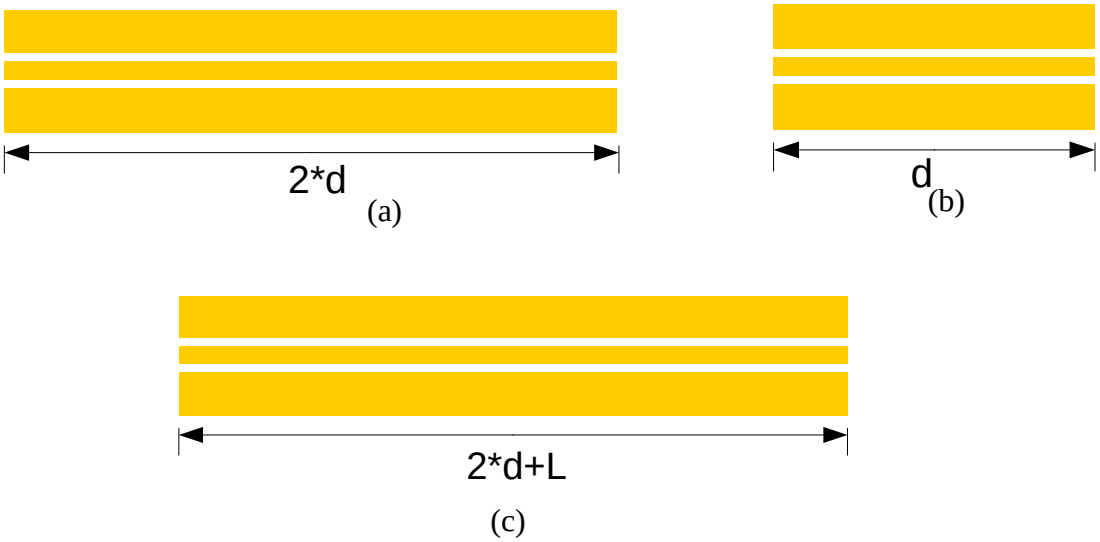

Figure 4.7:Designed TRL calibration kit at 12.4 GHz. (a) Through, (b) Reflect, and (c) Line. d = 70, L = 2.57. (Dimensions in mm)

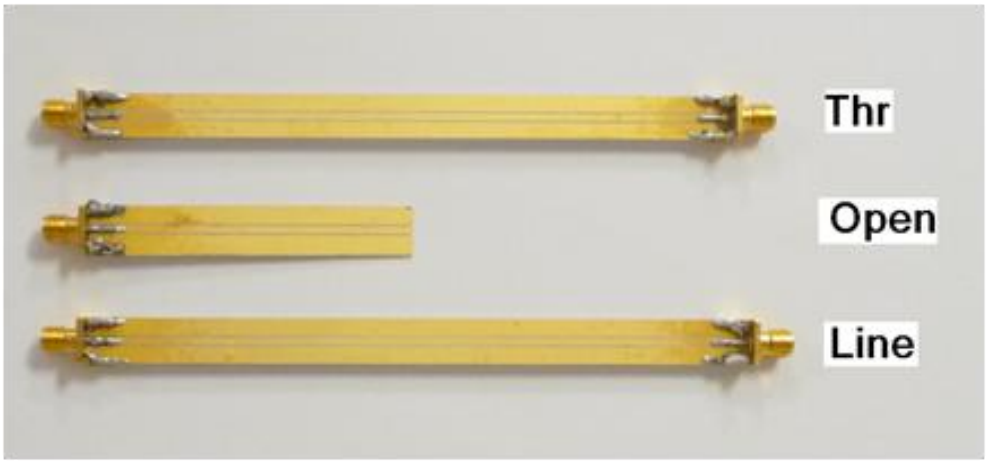

Figure 4.8: Fabricated TRL calibration standards.

As shown in Fig. 4.7, a TRL calibration kit is designed at 12.4 GHz, which corresponds to the fr of the cavity resonator at around 500oC as shown in the next section. The substrate is ADS-96R alumina with a thickness of 0.635 mm. The widths of the center conductor and slot are 1.5 and 0.4 mm, respectively. The electrical length of L is typically designed at 90^o but can be between 20^o and 160^o [42]. Due to the restrictions from the fabrication equipment for patterning and cutting, L is chosen to be 2.57 mm, corresponding to an electrical length of 62^o which is around 1/6 λg. λg is the guide wavelength of the CPW line at 12.4 GHz. The fabricated TRL calibration kit is shown in Fig. 4.8.

4.3.3 Metallization

The metallization of the SiCN sample is performed in two steps. First, a 0.3-μm-thick Cr layer is evaporated on the sample. It is noted that due to the directive nature of evaporation, five evaporations at different angles are needed to cover the entire surface of the sample. Then, a 7-μm-thick Au layer is electroplated to minimize the conductor loss due to the skin depth effect. The temperature of the gold plating solution and the voltage cross the anode and cathode has been optimized through many experiments to realize uniform coverage of Au. The solution is stirred and heated in the range of 65 ± 2^oC using a stirring hot plate. To ensure high plating quality, the voltage should be less than 1.5 volts and the current density passing through the surface of the sample should be kept less than 4 mA/in^2. Fig. 4.9 shows the variation of voltage and current density during the gold electroplating process. In Stage 1, since the resistance of the 0.3-μm-thick Cr seed layer is relatively high, the voltage is slowly ramped up from 0.5 to 1.5 V when the current density increases from 0 to 4 mA/in^2 in a nonlinear fashion. t0 depends on the sample size and is approximately 10 min in this study. To keep the current density at 4 mA/in^2 in Stage 2,

the voltage needs to be decreased as shown in Fig. 4.9 since the resistance of the metal layer becomes smaller as the gold layer gets thicker. The coupling slots are formed by taping during the evaporation. The final dimensions of the two coupling slots are measured to be 3.1 × 0.6 mm^2, and 2.7 × 0.8 mm^2, respectively, due to fabrication tolerances.

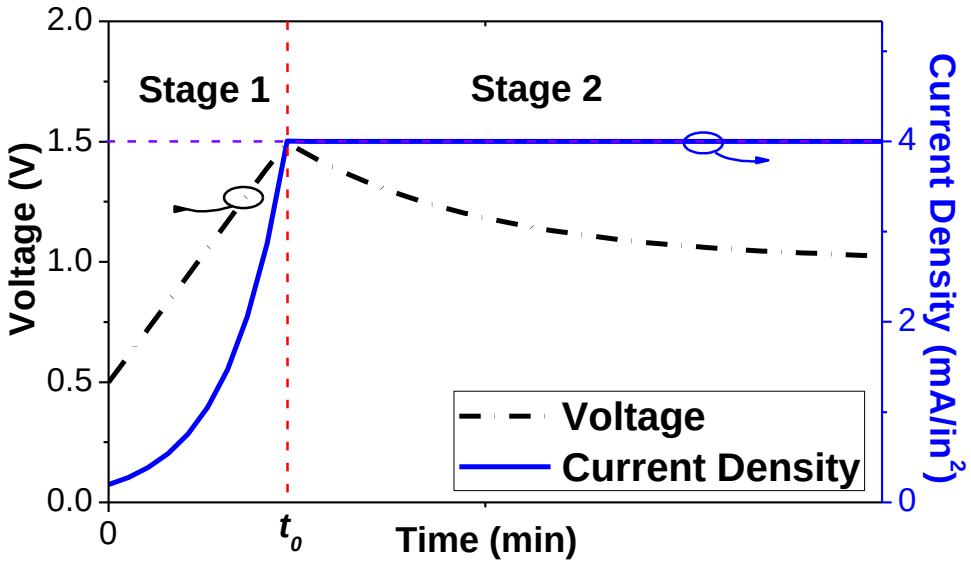

Figure 4.9: Voltage and current density variations during gold electroplating.

The CPW lines on the alumina board are photolithographically defined and metalized using the same procedure as for the sample.

4.3.4 High Temperature Measurement Setup

The measurement is performed from 25 to 500°C, which is limited by the choice of metals in this study. SiCN ceramic materials have been demonstrated to be thermally and mechanically stable in corrosive gases and at temperatures up to 1500°C.

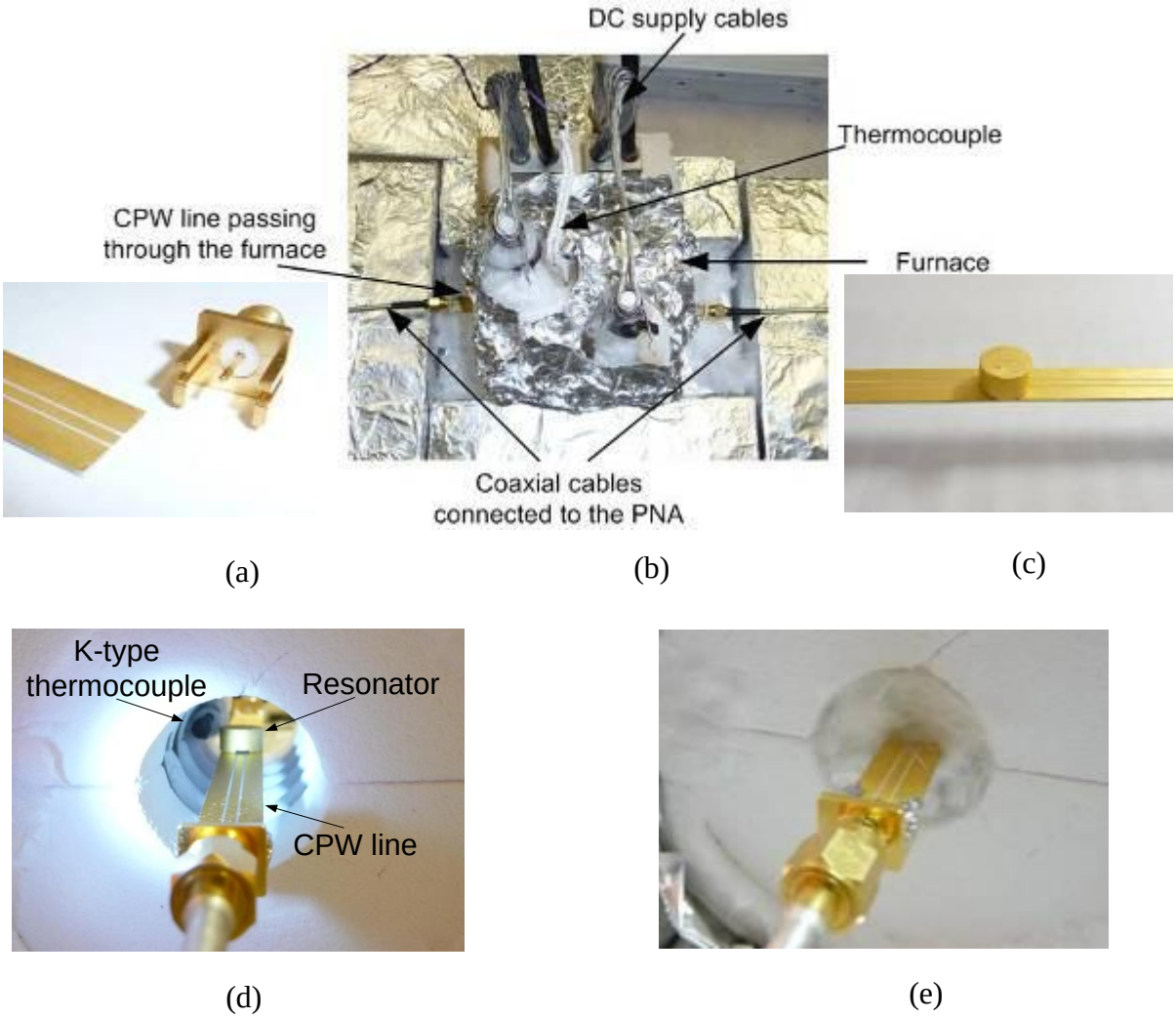

Figure 4.10: (a) The connector before soldering. (b) The furnace containing high-temperature measurement setup connected to the RF cables. (c) Sample over CPW line outside the furnace. (d) Sample and CPW line inside the furnace. (e) Sample inside the furnace with thermal isolation at the open ends of the furnace.

The high-temperature measurement setup is shown in Fig. 4.10. To create a high-temperature zone with precise temperature control, a cylindrical furnace (Robust Radiator from Micropyretics Heaters International Inc., Model number RHUL-MP1125-4) is used. This furnace has a

cylindrical hot zone of 25.4 mm in diameter and 50.8 mm in length, which can be heated up to 1500^{o}C with ±2^{o}C accuracy using a closed-loop feedback temperature controller. In the measurement, a programmable DC power supply (Genesys^{TM} 1500W from TDK-Lambda Americas Inc., Model number GEN 12.5-120) and a temperature controller (Omega CN96211TR) are used to realize precisely temperature control inside the furnace. The alumina board is placed inside the furnace with both ports extending outside the furnace. The metalized SiCN resonator is located in the middle of the hot zone.

To avoid ventilation and temperature instability, the two open ends of the furnace are sealed using Alumina Silica Ceramic Fiber extreme-temperature sheeting (Al_2O_3 Wool) which can withstand up to 1260^{o}C. With the sealing, the temperature at the open ends of the CPW lines outside the furnace is measured to be around 120^{o}C when the hot zone is heated to 500^{o}C. Therefore, SMA connectors remain intact during the entire measurement procedure.

4.3.5 Measurements Results

TRL calibration is performed using an Agilent Performance Network Analyzer (PNA) N5230A at every temperature point where the sample is measured. IF-bandwidth is 1.5 KHz, spanned frequency range from 12 GHz to 12.8 GHz, and the number of acquired points is 6401. Then, calibrated S_{21} of the high-temperature characterization setup described in the previous section is recorded and shown in Fig. 4.11.

The measured f_r and Q_u of the SiCN resonator are plotted against temperature in Fig. 4.12. f_r decreases from 12.643 to 12.357 GHz as the temperature increases from 25 to 500^{o}C. Therefore, the average measurement sensitivity is found to be 0.547 MHz/^{o}C. It should be noted that the thermal expansion coefficient (CTE) of SiCN is very small, i.e. 5×10^{-6}/K; therefore its effect on the f_r is insignificant. The maximum Q_u of 207.5 was measured at room temperature. Q_u is reduced to 45.1 at 500^{o}C due to the increased losses within SiCN and metal. Ten independent measurements are performed to verify the measurement repeatability. The mean value, standard deviation and experimental uncertainty for both f_r and Q_u , and extracted ε_r and tanδ are listed in Table II. It shows the standard deviation for f_r is very small, no more than 0.02%, and for Q_u, less than 3%.

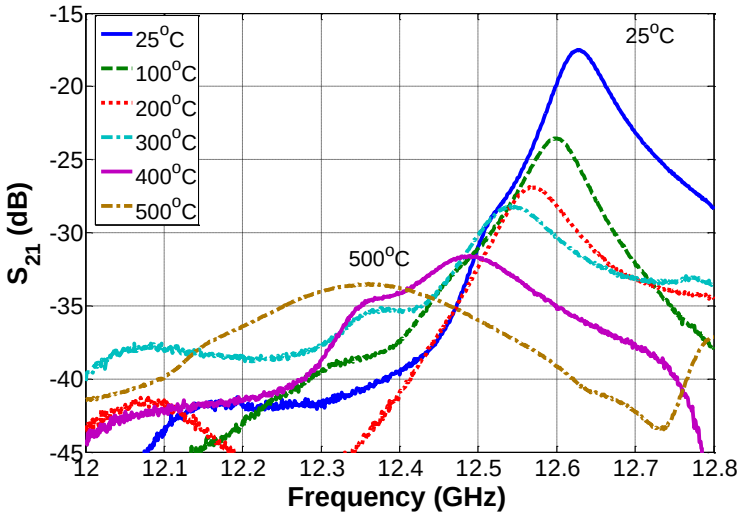

Figure 4.11: Measured S_{21} versus frequency at different temperatures.

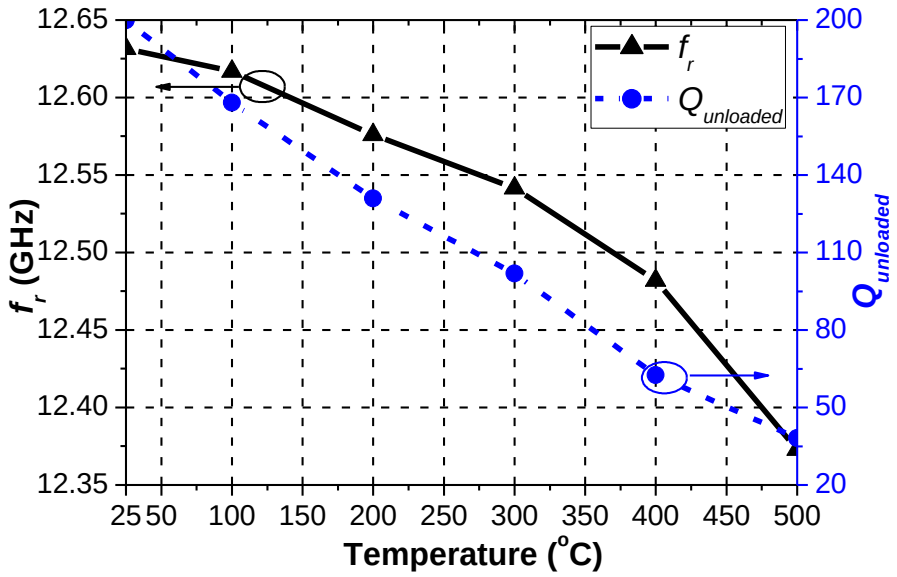

Figure 4.12: Measured f_r and Q_u versus temperature.

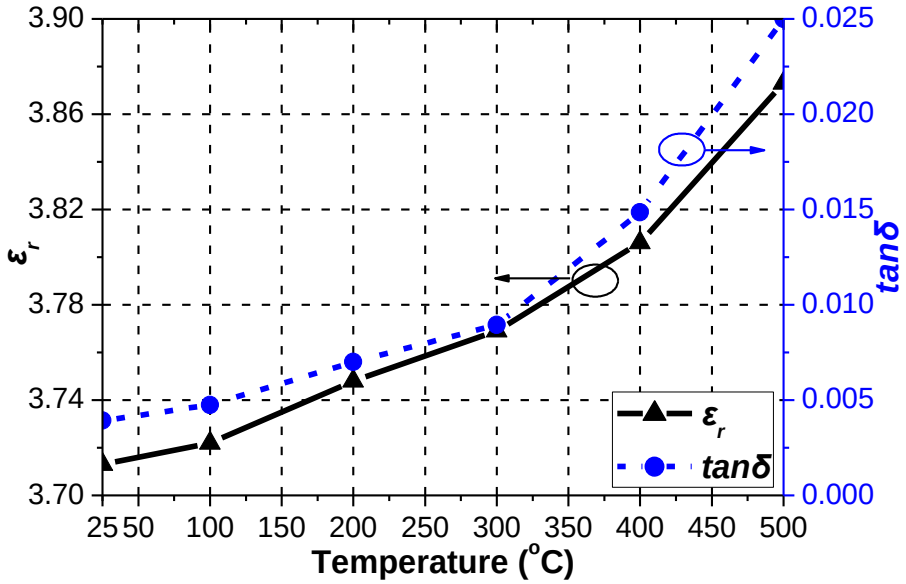

Figure 4.13: Extracted ε_r and $tan\delta$ versus temperature.

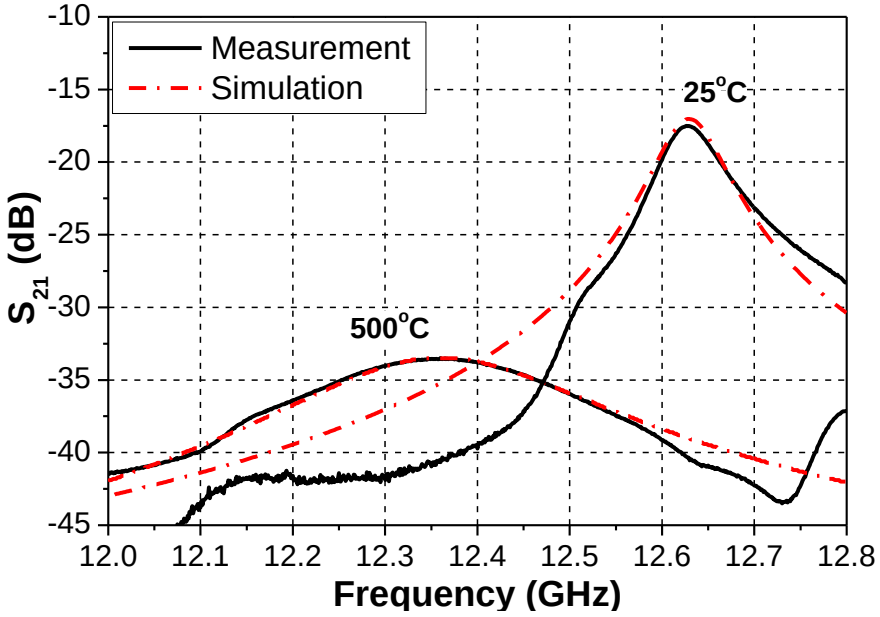

Figure 4.14: Measured and simulated S_{21} results of the SiCN sample characterization at 25 and 500°C

The extracted ε_r and tanδ of SiCN are plotted in Fig. 4.13, by performing parametric sweeps of these two variables in HFSS simulations. The comparison between the measured and simulated S_{21} results for 25 and 500°C characterization is shown in Fig. 4.14. It should be noticed that the agreement between the two curves constituted an excellent confirmation of this method. The dielectric constant and loss tangent of SiCN increase from 3.707 to 3.883 and from 0.0038 to 0.0213, respectively, within 25-500°C. It should be noted that these two values at the room temperature agree well with the results obtained from the waveguide cavity method. In addition, due to the lack of experimental data on the temperature-dependent metal conductivity, it is assumed to be constant across the temperature range in HFSS simulations, which typically

decreases versus temperature. Therefore, the actual loss tangent of SiCN at elevated temperatures should be lower than the extracted values.

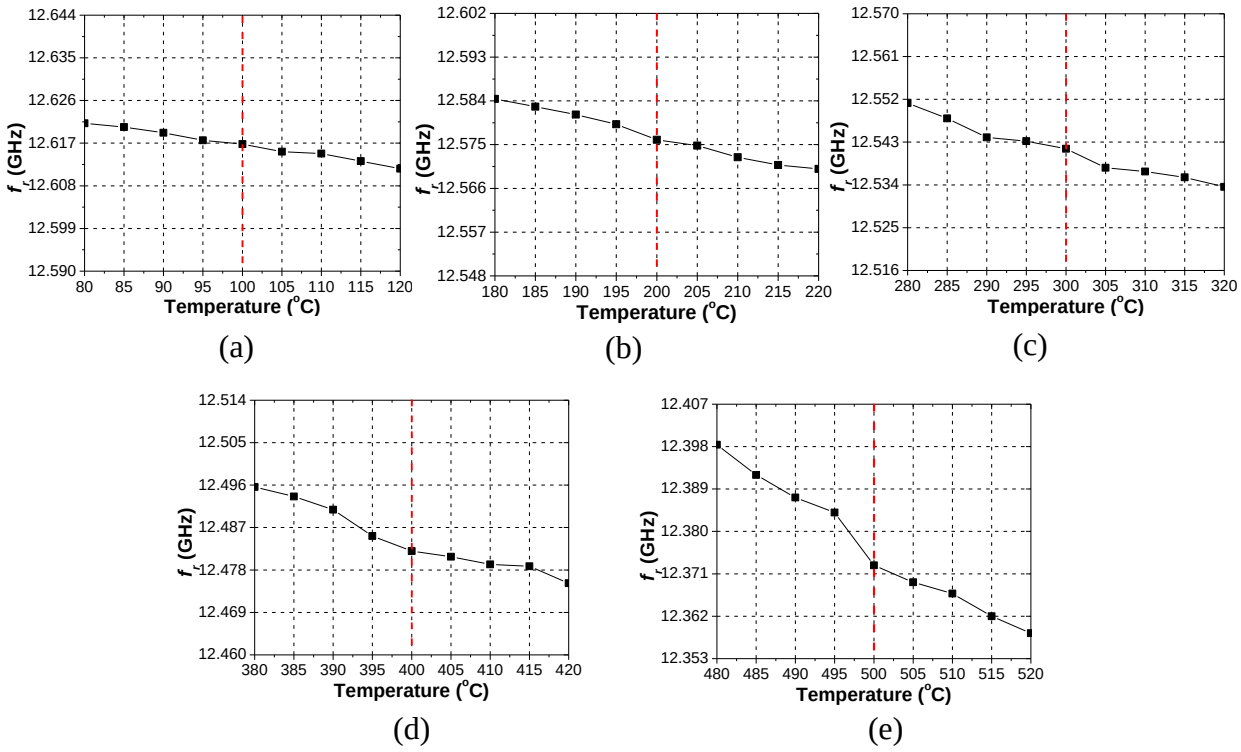

Figure 4.15:Measured f_r versus temperature at the center temperature of (a) 100°C, (b) 200°C, (c) 300°C, (d) 400°C, and (e) 500°C.

In order to quantify the temperature measurement accuracy using this method, the measurement procedure is repeated in the range of ±20°C at center temperatures of 100, 200, 300, 400, and 500°C, with 5°C increments. The measured f_r versus temperature is shown in Fig. 4.15. To compare the slope of these curves, all the plots in Fig. 4.15 use the same scale in the vertical axis. It is observed the change of f_r is progressively faster when temperature increases, which indicates

higher temperature measurement sensitivity (resolution) at higher temperatures. It is noted that Q_u decreases versus temperature, which adversely affects the measurement sensitivity.

Table 4.1: Measured f_r, Q_u and extracted ε_r, $tan\delta$ with standard deviations (σ) and uncertainty (s_u) for SiCN sample at different temperatures

Temperature(^{o}C)	f_r (GHz) (σ) (s_u)	ε_r (σ) (s_u)	Q_U (σ) (s_u)	$tan\delta$ (σ) (s_u)
25	12.6433 (0.02%) (0.0007)	3.7071 (0.04%) (0.0004)	207.5 (2.92%) (1.9)	0.0038 (3.49%) (0.0001)
100	12.5958 (0.01%) (0.0005)	3.7357 (0.03%) (0.0003)	169.7 (1.24%) (0.6)	0.0048 (1.31%) (0.0001)
200	12.5776 (0.01%) (0.0002)	3.7466 (0.01%) (0.0001)	144.6 (1.27%) (0.6)	0.0063 (1.99%) (0.0001)
300	12.5553 (0.01%) (0.0002)	3.7601 (0.01%) (0.0001)	100.4 (1.58%) (0.6)	0.0093 (1.65%) (0.0001)
400	12.4758 (0.01%) (0.0004)	3.8081 (0.02%) (0.0002)	73.1 (1.36%) (0.2)	0.0130 (1.39%) (0.0001)
500	12.3565 (0.02%) (0.0007)	3.8826 (0.04%) (0.0004)	45.1 (1.97%) (0.2)	0.0213 (2.25%) (0.0001)

4.4 Characterization Up to 1000^{o}C

At the temperature above 500^{o}C the chromium oxide products, even though there is a 7-μm layer of gold covering the chromium layer. Therefore, the CPW line with Cr-Au metallization cannot work when the temperature is over 500^{o}C. The platinum is more stable at high temperature and is one of the best candidates for the metallization. Platinum (Pt) paste (5542 PRINT Grade, ESL Electro Science) is used to metalize the CPW line and the Si_4B_1CN (sintered at 1000^{o}C) sample.

The advantages of the metallization with Pt paste are relatively simple and low cost, compared with evaporation and plating techniques.

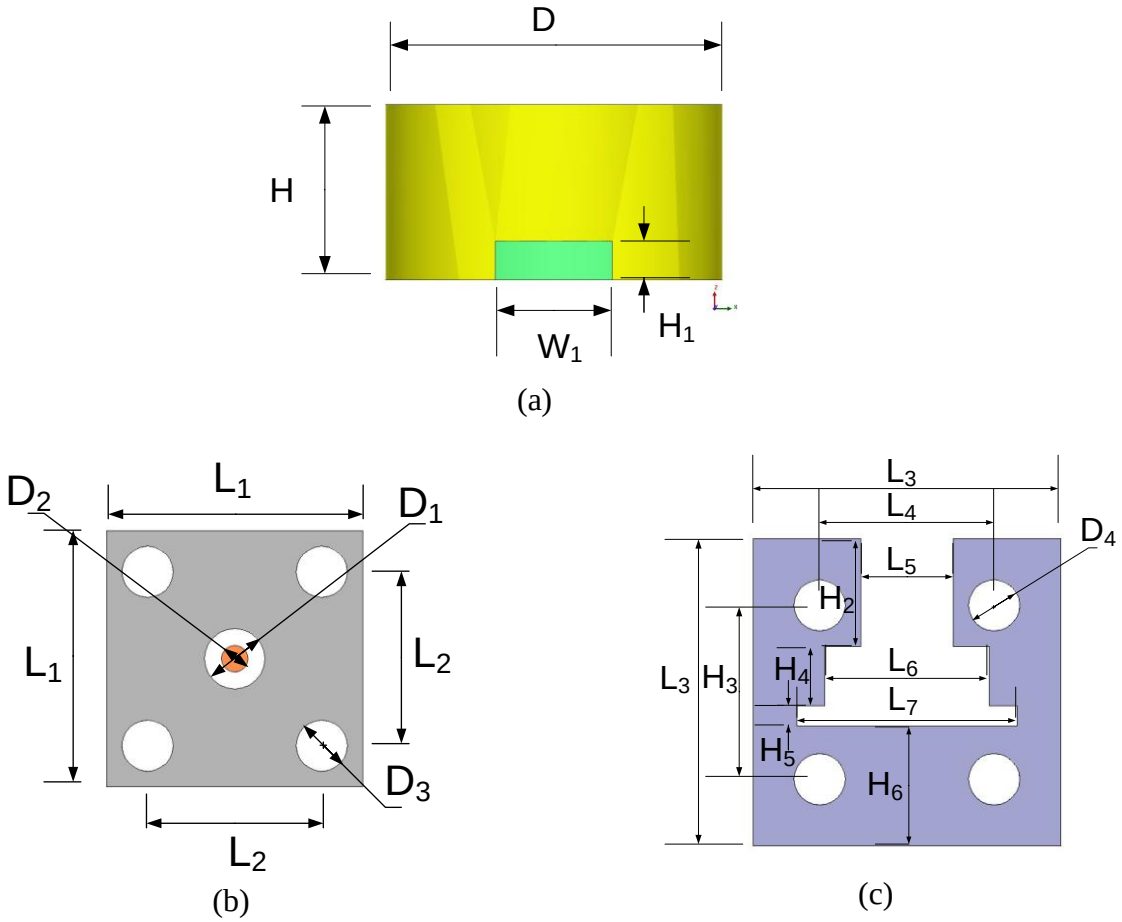

Figure 4.16:Dimensions of (a) the Si_4B_1CN (1000°C) resonator and the coupling slot, (b) high temperature connector and (c) holder. D = 9.37; H = 4.71; W_1 = 3; H_1 = 1; W = 1.5; L = 1.35; S = 0.4; L_1 = 12.7; L_2 = 8.64; D_1 = 3.05; D_2 = 1.32; D_3 = 2.54; L_3 = 15.24; L_4 = 8.64; L_5 = 4.57; L_6 = 7.00; L_7 = 10.92; H_2 = 5.33; H_3 = 8.64; H_4 = 2.60; H_5 = 1.00; H_6 = 6.31. (unit: mm)

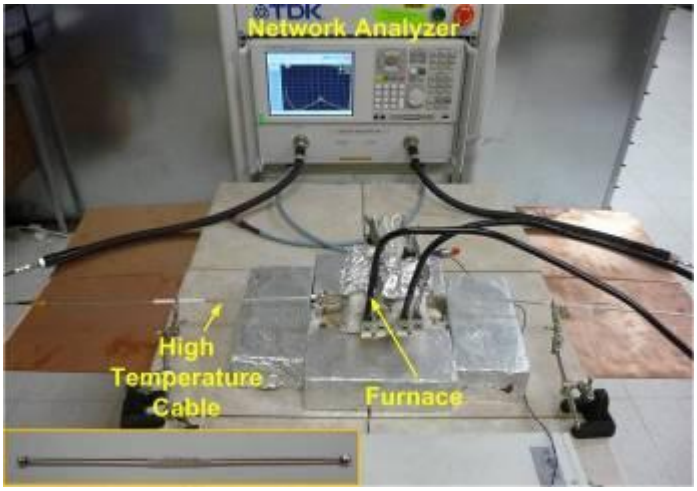

(a)

(b)

(c)

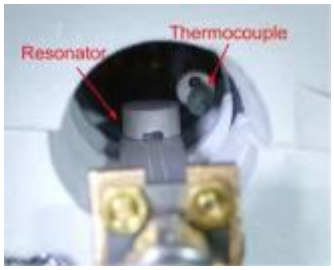

(d)

(e)

Figure 4.17: (a) The furnace containing high-temperature measurement setup connected to the high temperature cables. (b) Sample over CPW line outside the furnace. (c) Connector with holder before soldering .(d) Sample and CPW line inside the furnace. (e) High temperature connectors soldered onto the CPW line with the high temperature solder.

4.4.1 Metallization Process and Measurement Setup

The metallization process of the CPW line and the resonator is performed as follows. First, a layer of Pt paste was painted over a piece of alumina board and the board was left at room temperature for 10 minutes. Then, the board was dried at 100^{o}C for 10 minutes, and the sample was fired at 1000^{o}C for 10 minutes in the MTI GSL-1600X furnace. The ramp rate for both heating up and cooling down is 10^{o}C/min. The thickness of formed Pt layer is approximately 40 μm. Slots with 0.4 mm in width were cut on the board using diamond saw to form the CPW line. The dimension of CPW line with Pt metallization is the same as the one in Section III-B. The procedure of the metallization of the resonator is the same as that for CPW line, except that the opening slots on the sidewall of the sample were covered by the tape before being painted. The dimensions of the resonator with coupling slots are shown in Fig. 4.16(a).

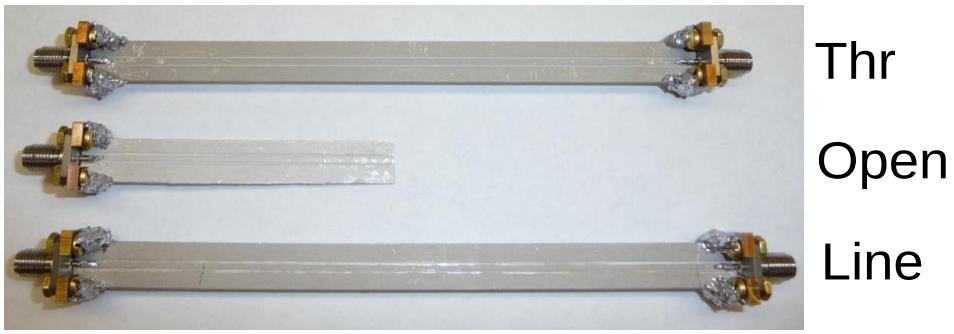

Figure 4.18:TRL calibration standards for the measurement

In order to ensure the measurement setup working above 1000^{o}C, high temperature solder (91Pb4Sn4Ag1In, melting point: 313^{o}C, Indium Corporation), high temperature connectors (600^{o}C) and cables (1000^{o}C, Time Microwave Systems) are used. A copper holder was custom-

made for better connection between the CPW line and connector. The dimensions of the connector and holder are shown in Fig. 4.16(b) and (c). The whole setup with close-up figures is shown in Fig. 4.17. High temperature cables are also used as the extension of CPW line to connect to the VNA, so the temperature at the ports of VNA is the room temperature.

The TRL calibration was conducted at each temperature before the measurements. The dimensions of the TRL calibration standards shown in Fig. 4.18 is the same as the one in the characterization up to 500^{o}C . The temperature of the inside of furnace was increased from 25 to 1000^{o}C during the measurement at the step of 100^{o}C when the temperature was above 100^{o}C. Ten independent measurements were performed for each temperature.

4.4.2 Measurement Results

The measurement results of S_{21} for the Si_4B_1CN (1000^{o}C) sample at different temperatures are plotted in Fig. 4.19. The f_r and Q_u versus temperature extracted from the results of S_{21} are plotted in Fig. 4.20. The f_r decreases from 11.206 to 10.856 GHz and Q_{un} decreases from 224.1 to 47.7, when the temperature increases from 25 to 1000^{o}C. Through HFSS simulations the ε_r and tanδ are extracted and plotted in Fig. 4.21. The ε_r and tanδ of SiCN increase from 4.8169 to 5.1322 and from 0.0020 to 0.0186, respectively, within 25-1000^{o}C. The type A experimental uncertainties for ε_r and tanδ are not more than 0.0004 and 0.0001, respectively. The mean value, standard deviation and experimental uncertainty for measured f_r and Q_u ,and extracted ε_r and tanδ are listed in Table 4.2. In comparing the measured and simulated S_{21} results for 25 and 1000^{o}C shown in Fig. 4.22, it is found that the consistent agreement between the two curves confirms this characterization method.

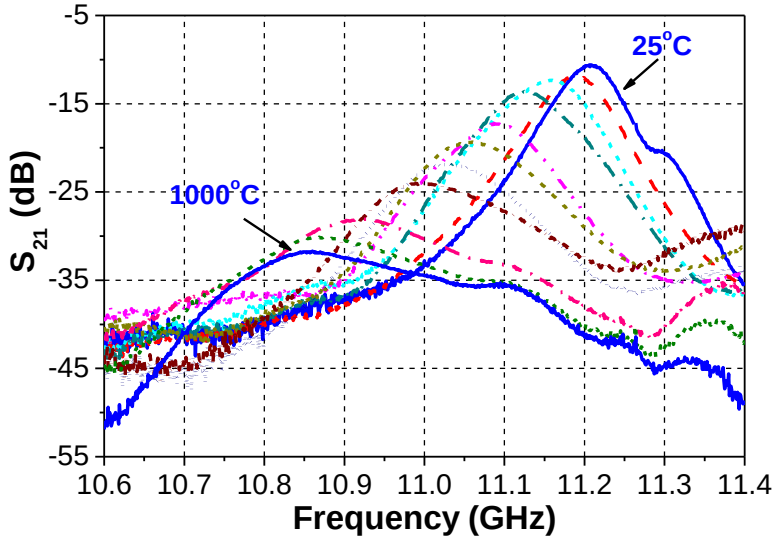

Figure 4.19:Measured S_{21} versus frequency at different temperatures.

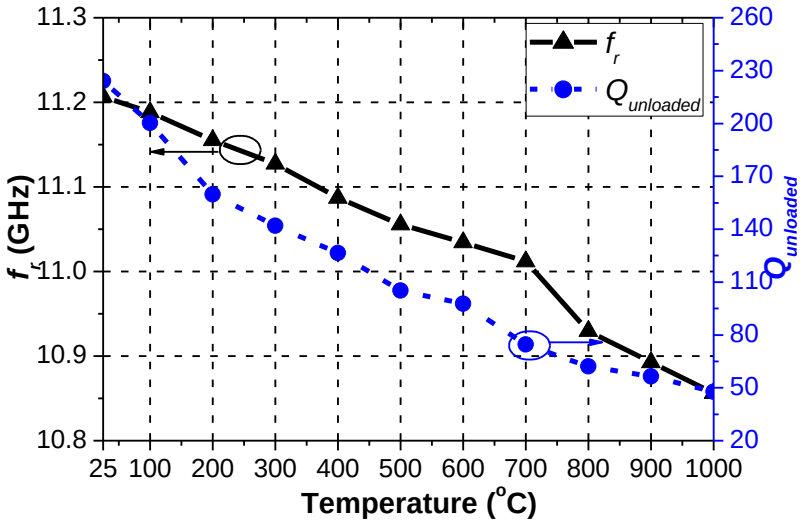

Figure 4.20:Measured f_r and Qu versus temperature.

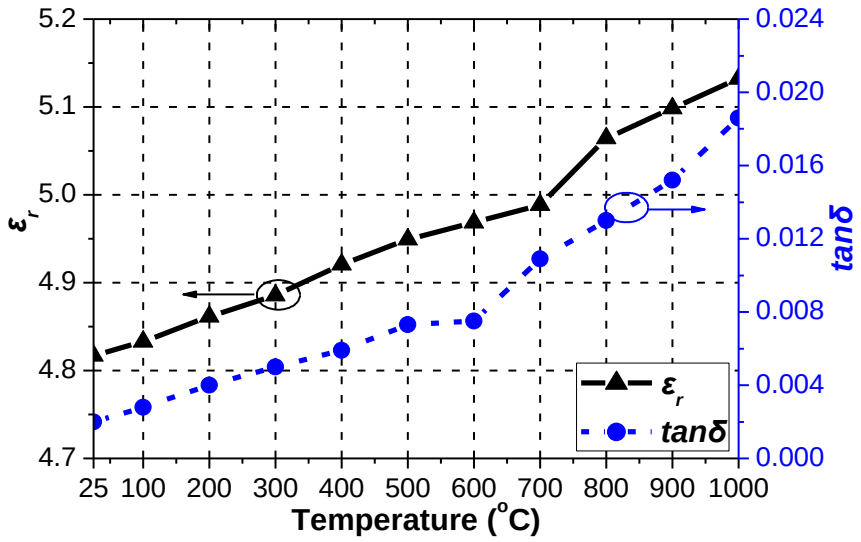

Figure 4.21: Extracted εr and tanδ versus temperature.

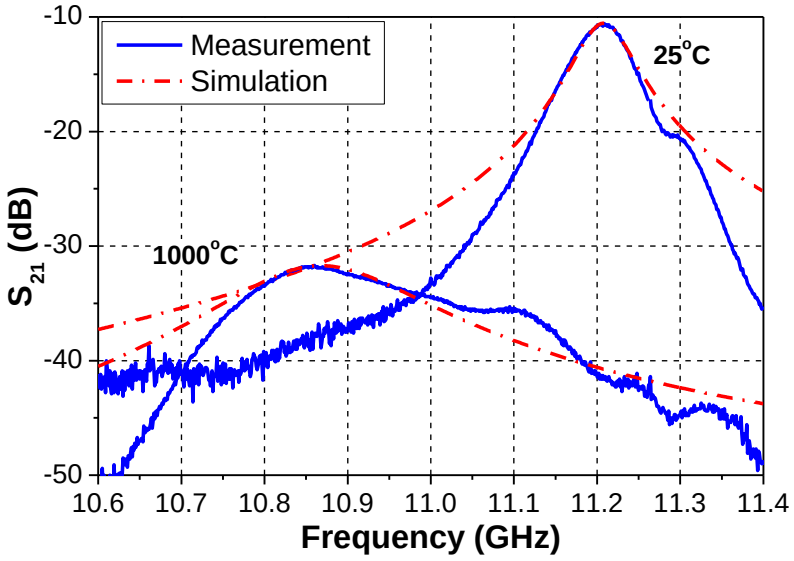

Figure 4.22: Measured and simulated S_{21} results of the Si_4B_1CN sample characterization at 1000°C.

Table 4.2: Measured f_r, Q_u and extracted ε_r, $tan\delta$ with standard deviations (σ) and uncertainty (s_u) for Si_4B_1CN (1000^{o}C) sample at different temperatures

Temperature (^{o}C)	f_r (GHz) (σ) (s_u)	ε_r (σ) (s_u)	Q_U (σ) (s_u)	$tan\delta$ (σ) (s_u)
25	11.2065 (0.01%) (0.0005)	4.8169 (0.03%) (0.0004)	224.1 (1.71%) (2.2)	0.0020 (5.80%) (0.0001)
100	11.1880 (0.01%) (0.0001)	4.8330 (0.01%) (0.0001)	200.3 (1.20%) (0.6)	0.0028 (2.68%) (0.0001)
200	11.1553 (0.01%) (0.0002)	4.8615 (0.01%) (0.0002)	159.7 (1.05%) (0.3)	0.0040 (2.34%) (0.0001)
300	11.1275 (0.01%) (0.0002)	4.8857 (0.01%) (0.0002)	142.0 (0.48%) (0.2)	0.0050 (0.76%) (0.0001)
400	11.0871 (0.01%) (0.0003)	4.9208 (0.02%) (0.0003)	126.5 (0.80%) (0.3)	0.0059 (1.06%) (0.0001)
500	11.0557 (0.01%) (0.0002)	4.9494 (0.01%) (0.0002)	105.1 (0.30%) (0.1)	0.0073 (0.29%) (0.0001)
600	11.0343 (0.01%) (0.0001)	4.9685 (0.01%) (0.0001)	97.7 (0.76%) (0.2)	0.0075 (1.46%) (0.0001)
700	11.0118 (0.01%) (0.0002)	4.9886 (0.01%) (0.0002)	74.5 (1.77%) (0.4)	0.0109 (1.45%) (0.0001)
800	10.9095 (0.02%) (0.0005)	5.0643 (0.03%) (0.0004)	62.2 (0.99%) (0.2)	0.0130 (1.40%) (0.0001)
900	10.8925 (0.01%) (0.0004)	5.0986 (0.02%) (0.0004)	56.4 (0.72%) (0.1)	0.0152 (0.94%) (0.0001)
1000	10.8563 (0.01%) (0.0004)	5.1322 (0.02%) (0.0003)	47.7 (0.96%) (0.1)	0.0186 (0.94%) (0.0001)

4.5 Characterization Up to 1300°C

Due to the higher loss tangent of the ceramic materials at the higher temperature, the resonant peak would fall below the noise level at the higher temperature. Therefore, it is harder to observe the resonant peaks of the resonator by the weak coupling through the openings on its sidewall. In order to keep the resonant peaks above the noise level, the slots under the resonator are cut for stronger coupling. The dimensions of coupling slots for characterizing Si_4B_1CN (sintered at 1200°C) are shown in Fig. 4.23.

Through calibration was conducted at room temperature before the measurements. The temperature of the inside of furnace was increased from 25 to 1300°C during the measurement at the step of 50°C when the temperature was above 50°C. The measurement results of S_{21} for different temperatures are plotted in Fig. 4.24. The f_r and Q_u versus temperature extracted from the results of S_{21} are plotted in Fig. 4.25 (a) and (b). The f_r decreases from 11.2 to 10.6 GHz and Q_{un} decreases from 85 to 19, when the temperature increases from 25 to 1300°C. At 1300°C the resonant peak is closed to the noise floor and the Q_{un} reaches the lowest value of 19. The extracted ε_r and $tan\delta$ versus temperature are plotted in the Fig. 4.26. The ε_r and tanδ of SiCN increase from 4.7561 to 5.3281 and from 0.0081 to 0.0434, respectively, within 25-1300°C.

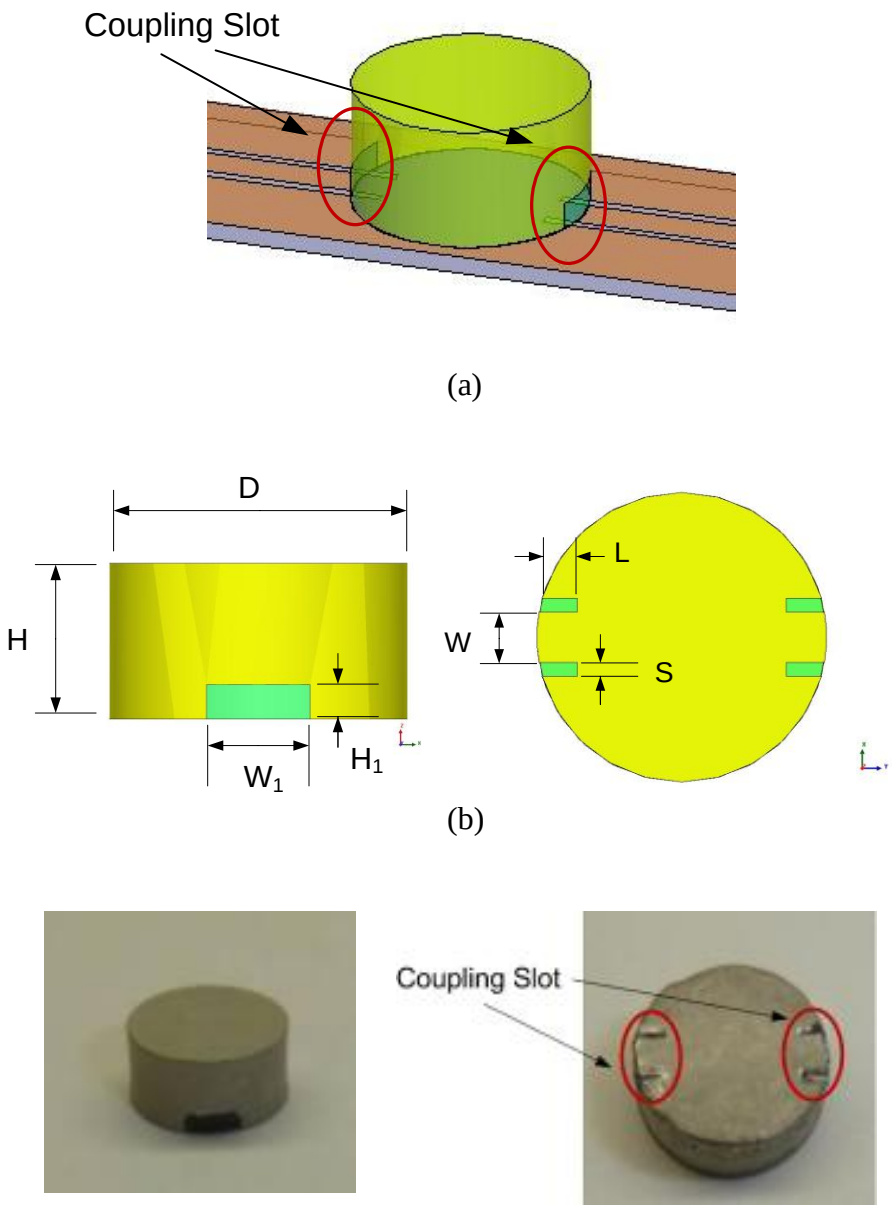

Figure 4.23: (a) Schematic of the resonator over CPW line (b) dimensions of the coupling slots (c) photos of sidewall and bottom with coupling slots for sample Si_4B_1CN (1200^{o}C). (*D*=9.37; *H*=4.71; W_1=3; H_1=1; *W*=1.5; *L*=1.35; *S*=0.4) (unit: mm)

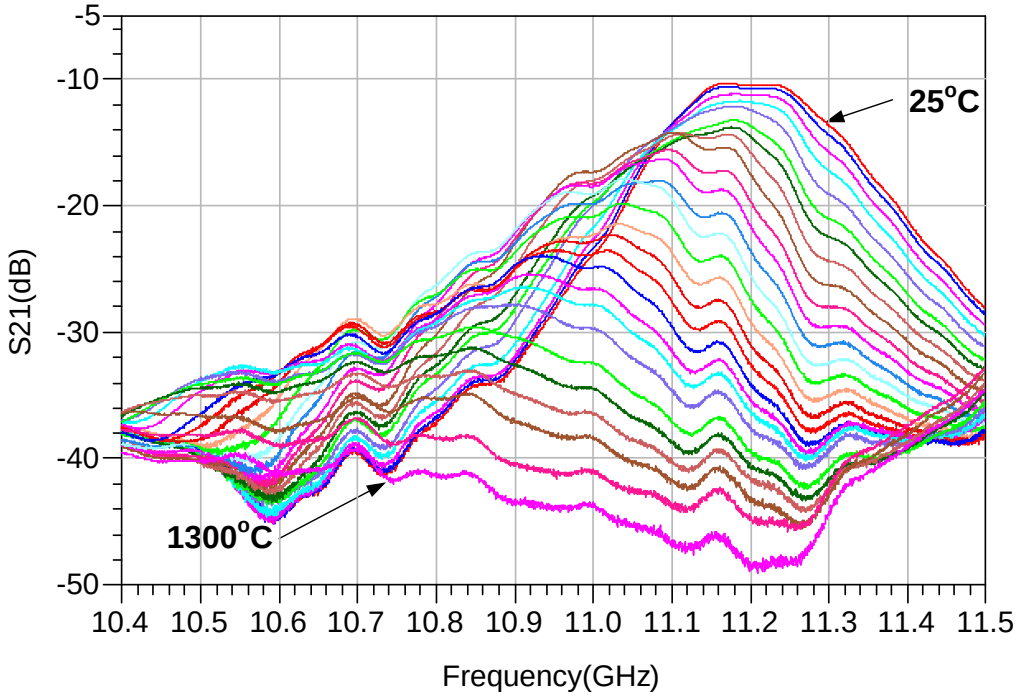

Figure 4.24:S_{21} for temperature from 25°C to 1300°C.

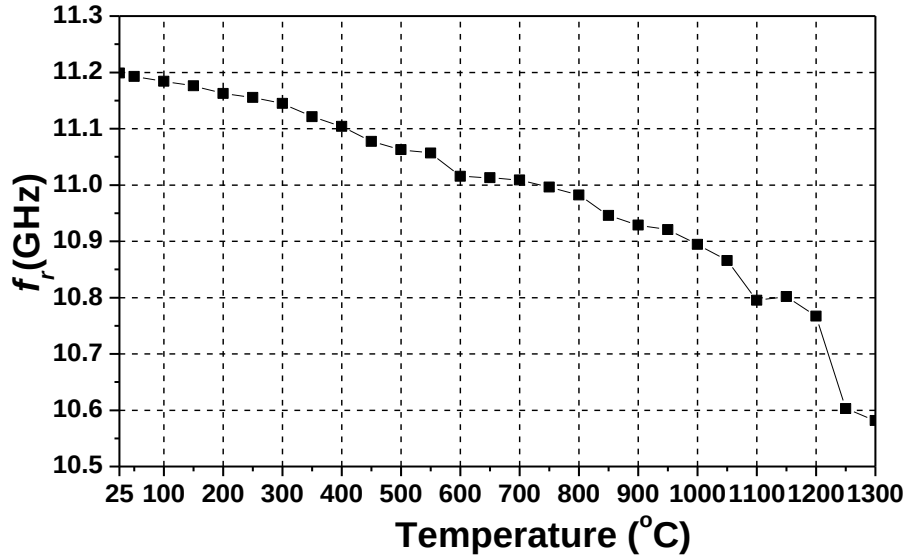

(a)

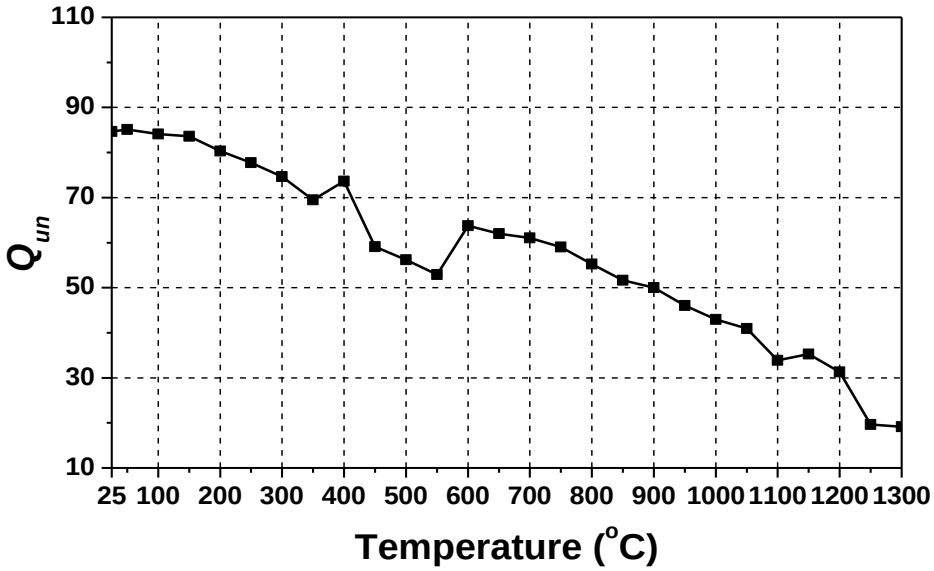

(b)

Figure 4.25:(a) Extracted f_r and (b) extracted Q_{un} versus temperature.

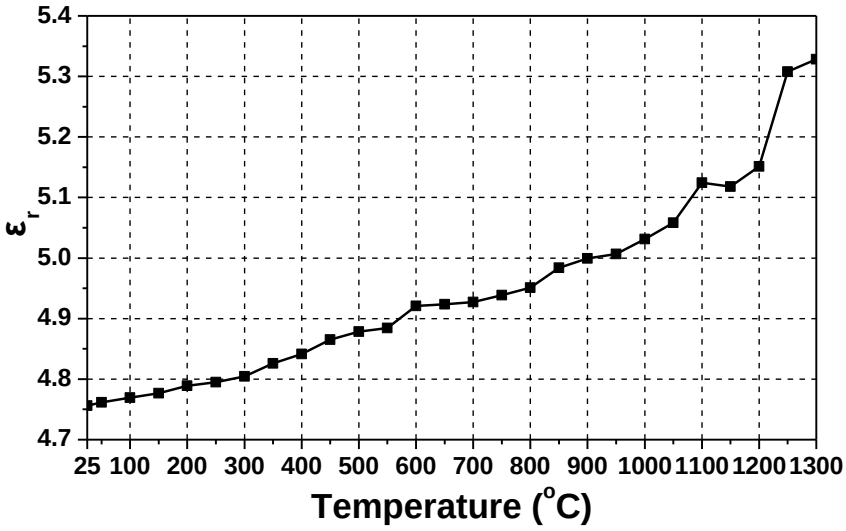

(a)

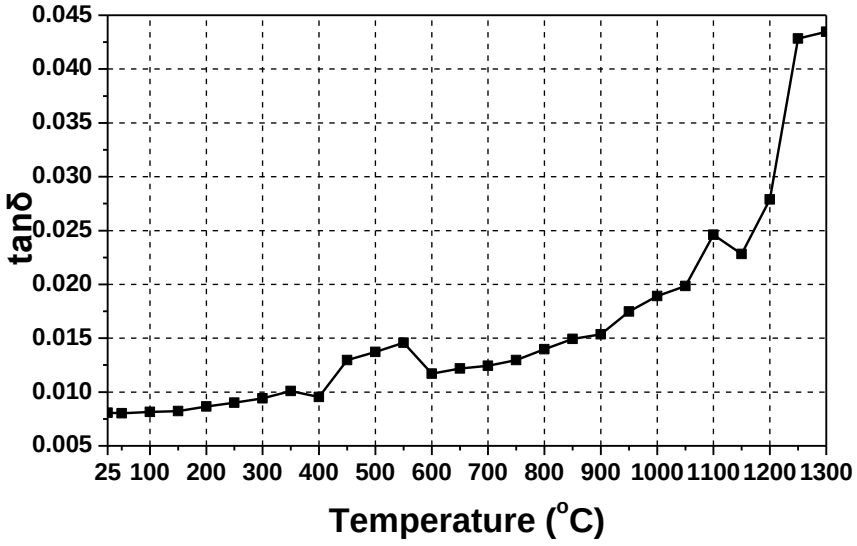

(b)

Figure 4.26:(a) Extracted ε_r and (b) extracted *tanδ* versus temperature .

4.6 Conclusion

The dielectric constant and loss tangent of high-temperature-stable Si(B)CN ceramic materials have been characterized at microwave frequencies up to 1300^{o}C. Two measurement setups for 500^{o}C and 1000^{o}C characterization with TRL calibrations were described in the paper. More than 10 measurements were done for all the characterizations to correctly estimate the statistical quantities: mean value and Type A experimental uncertainty. The accurate characterization of SiCN materials is critical for developing wireless passive sensors in harsh environment applications. Wireless passive sensors using SiCN materials will be developed for combustion turbines in the next chapter. Some sections inside turbines used in the power generation are at the high temperatures (from a few hundred to 1000^{o}C and above), so these proposed sensors can be used for temperature sensing.

CHAPTER 5 HIGH TEMPERATURE MATERIALS APPLICATIONS

5.1 Introduction

Wireless passive sensing systems are very attractive in a wide range of applications. The advantages of wireless passive sensing include battery-free operation, higher reliability, low maintenance cost, and a better chance of surviving harsh environments. The temperature dependency of the dielectric constant of SiCN materials is demonstrated at both low frequencies and microwave frequencies in the previous chapters. Based on this temperature-dependent dielectric constant behavior, three different types of sensors, corresponding to different antenna configurations, are designed and the prototypes are fabricated and tested. All of the sensors successfully perform at temperatures over 1000^{o}C.

5.2 Two-antenna Sensor

5.2.1 Wireless Sensing System Using Passive Microwave Resonators

A wireless sensing technique based on passive microwave resonators is proposed. The resonant frequency of the microwave resonator is related to temperature or gas properties. By measuring the resonant frequency of the resonator using a wireless technique, the information regarding temperature or gas properties can therefore be retrieved. To prove this concept, a wireless sensing system is designed and measured using a spiral resonator. However, this developed technique is general enough to be implemented to high-temperature or gas sensing applications by using resonators made of either high-temperature ceramics or gas sensitive materials [43].

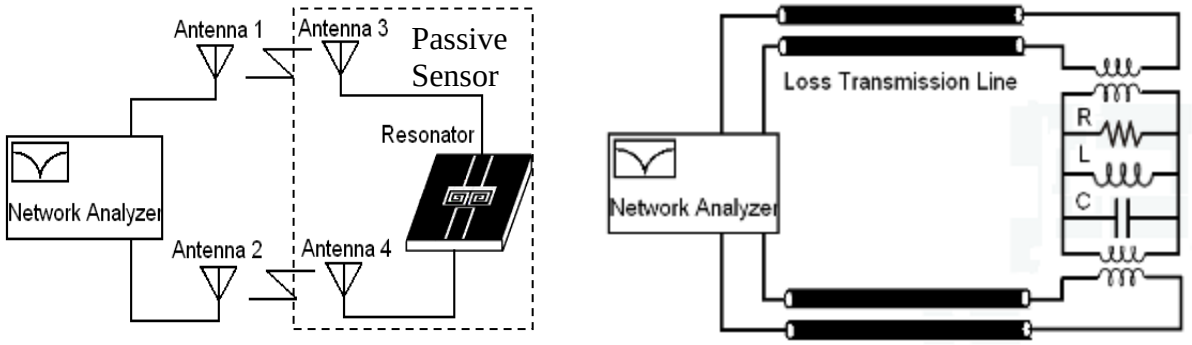

(a) (b)

Figure 5.1:(a) Illustration of a wireless passive sensor system. (b) Equivalent circuit of the sensor system in (a).

Fig. 5.1(a) illustrates the proposed wireless sensing system based on a passive microwave resonator. The passive sensor is composed of two antennas and a microwave resonator. This sensor system sends out a signal from Antenna 1 to Antenna 3. Since there is a resonator in between Antennas 3 and 4, only the energy at the resonant frequency passes through this resonator and reaches Antenna 2 via Antenna 4, representing a peak in S_{21} measured by a vector network analyzer.

This wireless sensing system is modeled by an equivalent circuit as shown in Fig. 5.1(b). The microwave resonator is represented by a parallel RLC network. The coupling between the resonator and the transmission line can be characterized using a transformer. Since there is free-space path loss due to the transmission of energy between the antennas, we can use a lossy transmission line to model this phenomenon. Based on this equivalent circuit model, it is expected that S_{21} has a peak in the frequency domain which corresponds to the resonant

frequency of the microwave resonator, though the magnitude of S_{21} is reduced due to the free space path loss.

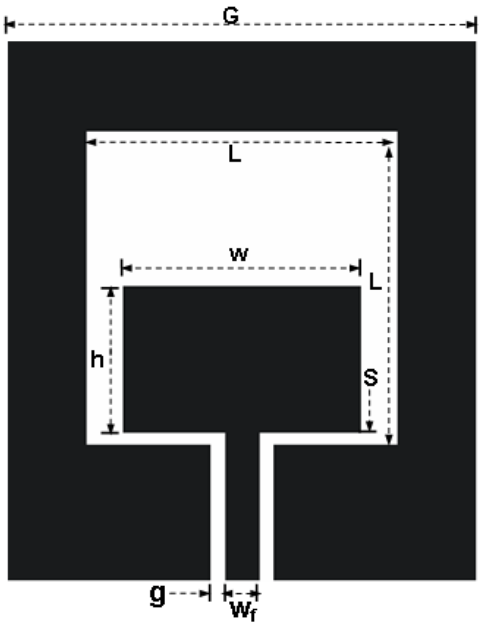

Figure 5.2: Wideband antenna geometry. (*G*=48mm, *L*=28mm,*W*=24.2mm,*S*=0.15mm,*h*=14mm, *g*=0.2mm, W_f=3mm)

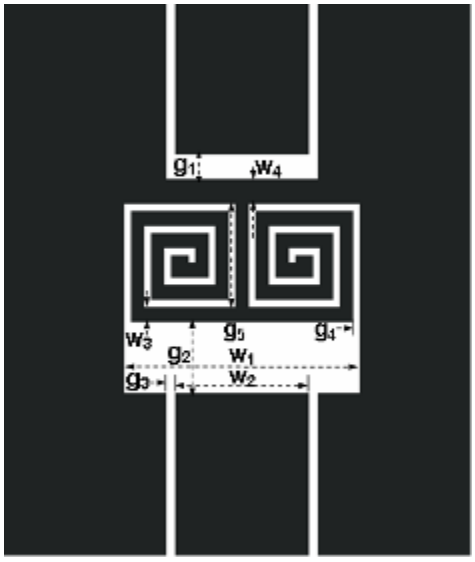

Figure 5.3:4.02 GHz resonator geometry. (W_1=5.3mm, W_2=3mm, W_3=0.3mm, W_4=0.5mm, g_1=0.5mm, g_2=1.6mm, g_3=0.2mm, g_4=0.15mm, g_5=1.95mm)

In real sensing applications, the resonant frequency of the resonator changes versus temperature or gas properties. Therefore, the antenna used in this system should cover the range of possible resonant frequencies. The antenna structure published in [44] is used here to achieve a 35% factional bandwidth with a center frequency of 3.82 GHz. A spiral resonator structure [45] is chosen for compact size and high quality factors and designed to achieve resonant frequencies of 3.59 GHz and 4.02 GHz, respectively. Both antennas and resonators are designed on 60-mil-thick Rogers RO3003 substrates. The geometries of the antenna and spiral resonator are presented in Fig. 5.2 and 5.3 in detail.

This wireless sensing system is set up as shown in Fig. 5.1(a) inside an anechoic chamber. The distance between Antennas 1 and 2 is set to be 28 cm. In order to study the sensing range of this wireless system, the spacing between antennas 1 and 3, which is same as that between antennas 2 and 4, is swept from 3 cm to 10 cm. The measured S_{21} of the system with resonators at 3.59 and 4.02 GHz are plotted in Fig. 5.4 and 5.5, respectively. To verify that the measured resonant frequencies of the wireless system are same as those of the resonators themselves, S_{21} for each resonator is also plotted for comparison. Very close agreement (within 0.6%) has been found among measured resonant frequencies [43].

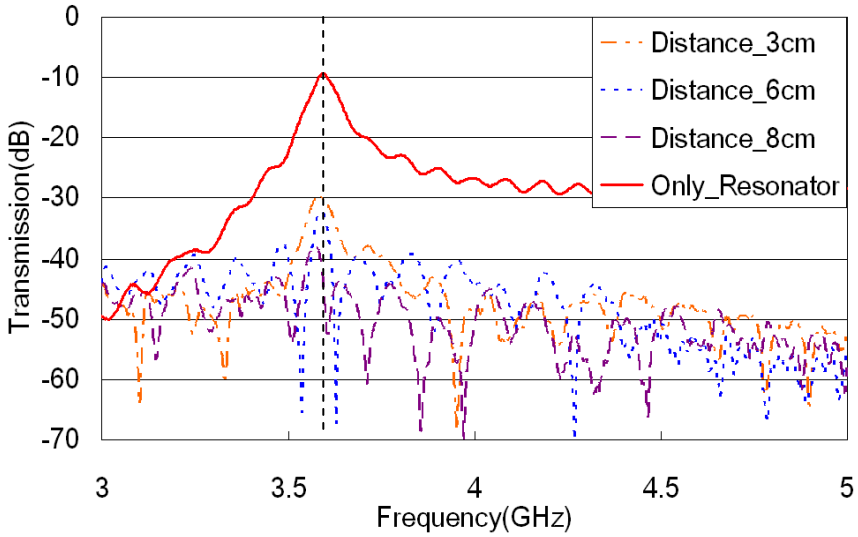

Figure 5.4:Measured S21 for the 3.59 GHz resonator only and the wireless system with antenna spacing of 3 cm, 6cm, 8 cm.

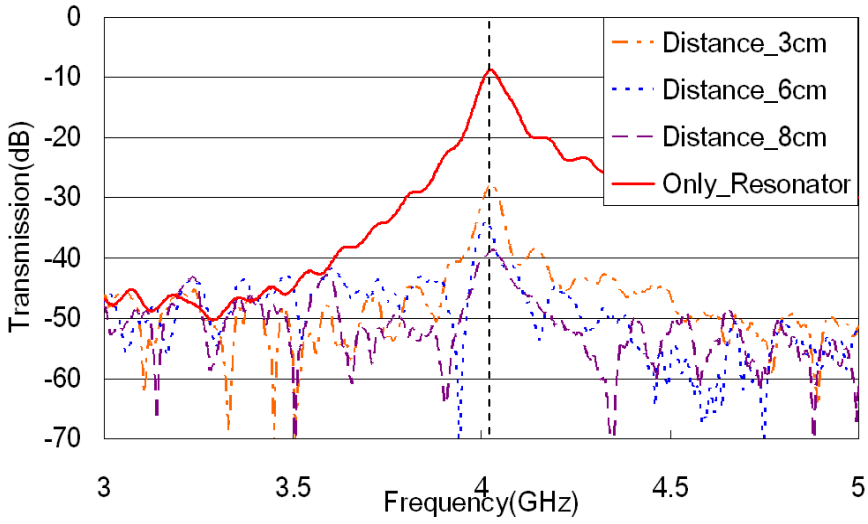

Figure 5.5:Measured S21 for the 4.02 GHz resonator only and the wireless system with antenna spacing of 3 cm, 6cm, 8 cm.

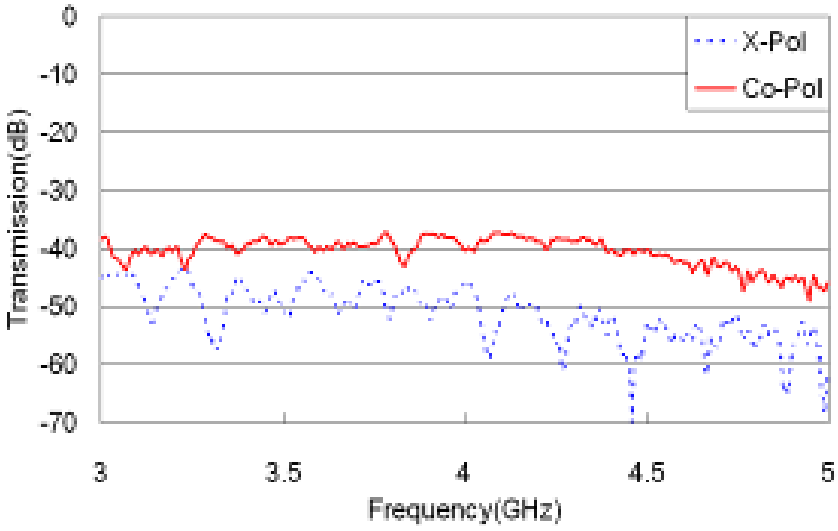

Figure 5.6:Direct transmission between Antennas 1 and 2 for Co-Pol and X-Pol.

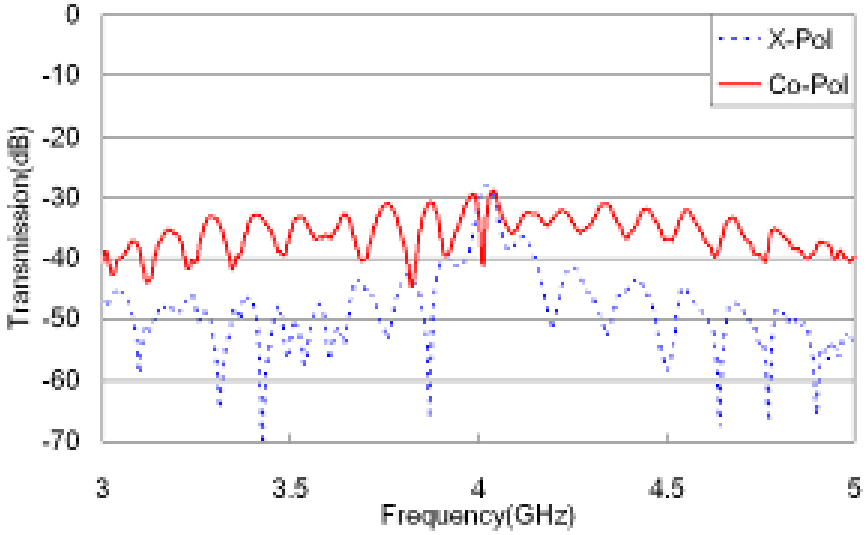

Figure 5.7:Comparison of wireless sensing between Co-Pol and X-Pol cases with an antenna spacing of 4 cm.

In the demonstration shown earlier, antennas 1 and 3 are vertically polarized while antennas 2 and 4 are horizontally polarized. The direct energy coupling between antennas 1 and 2 has an adverse effect on the measured results. Fig. 5.6 shows the transmission between Antennas 1 and 2 for both co-polarization and cross-polarization cases. The cross-polarization case gives approximately 10-dB more isolation than the co-polarization case. This phenomenon is further proved by observing a case in which the spacing between antennas 1 and 3 is 4 cm. As shown in Fig. 5.7, the resonant peak is unidentifiable for the co-polarization case, but clearly visible for the cross-polarization case [43].

A wireless sensing system based on a microwave resonator has been successfully demonstrated. The sensed resonant frequency is identical to the resonant frequency of the resonators. A sensing range up to 8 cm between antenna pairs was achieved. It was found that the placement of antenna orientations has a noticeable effect on the sensing range. This wireless sensing system will be used to sense very high temperatures using ceramic-based microwave resonators [43].

5.2.2 Sensor Design

The wireless passive detection method based on microwave resonators was presented in the last section. Two antennas were connected to a planar resonator to enable wireless detection of the resonant frequency. However, there were three issues associated with that approach for the aforementioned applications. First, the antennas used in that approach were bidirectional, causing undesired radiations and loss of energy. Second, the resonator was made of non-high-

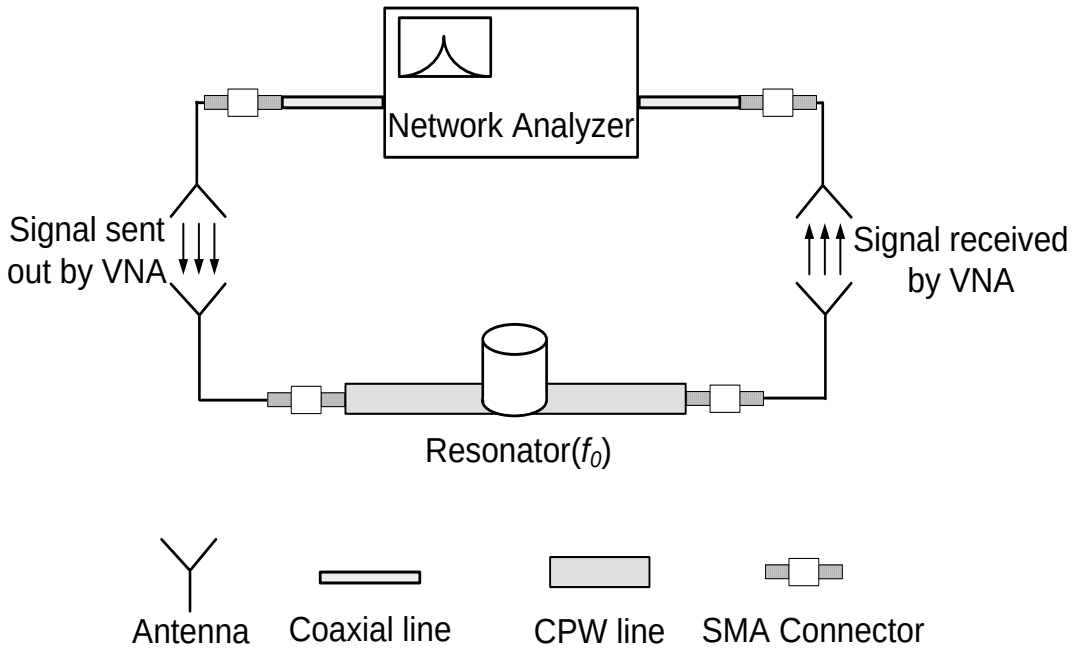

temperature-stable dielectric materials. Third, due to the planar geometry of the resonator, the Q factor of the resonator was very limited, which restricted the sensing resolution [46].

Figure 5.8:Flowchart showing the wireless sensing mechanism.

To overcome the aforementioned limitations, a new sensing mechanism is proposed here using two pairs of antennas to wirelessly measure the resonant frequency of a dielectrically-loaded cavity resonator as shown in Fig. 5.8. The cavity resonator is fabricated using SiCN ceramic material and coupled to CPW lines through two coupling slots. Two pairs of antennas are implemented at each side of the resonator. Within each antenna pair, one is connected to the CPW line and the other is connected to one port of the network analyzer. A wide-band signal is transmitted through the antenna pairs and passes the resonator via the coupling slots. Maximum

transfer of energy occurs at the resonant frequency of the resonator and is observed as a peak in the S_{21}. This wireless detection of the resonant frequency will be used to form a temperature

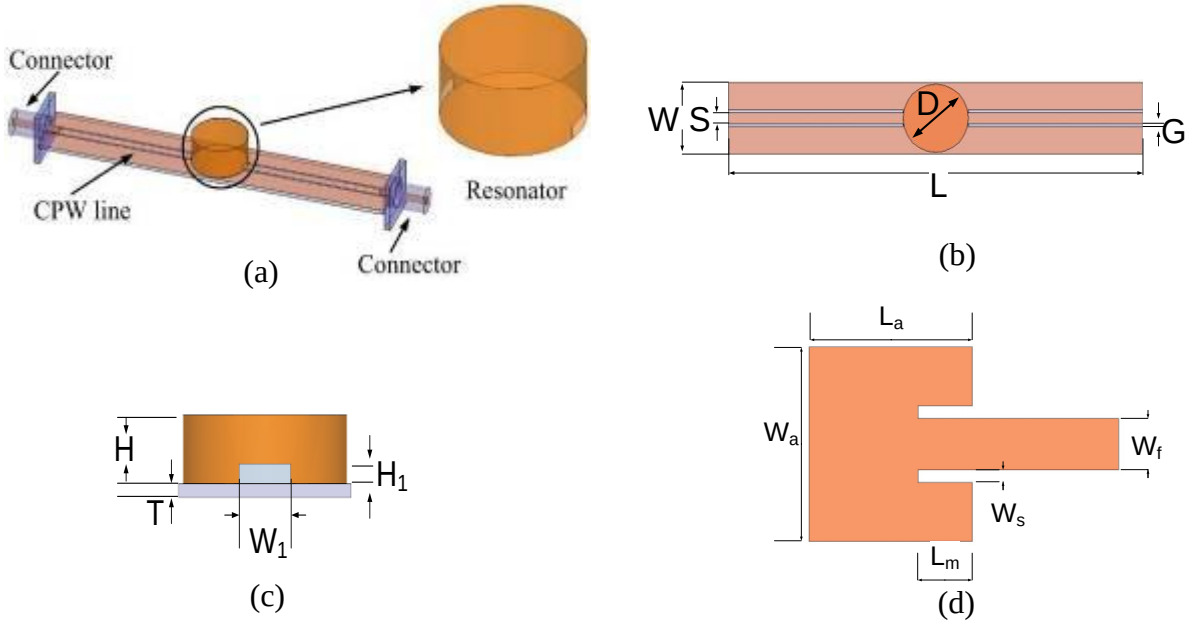

sensor due to the temperature-dependent dielectric constant of SiCN ceramic materials employed in the resonator [46].

Figure 5.9:(a) Passive temperature sensor with a SiCN cavity resonator coupled to CPW lines. (b) Top and (c) side view of the sensor. S = 1.5; G = 0.4; W = 10; T = 0.635; L = 149.4; D = 9.41; H = 5.01; H_1 = 1; W_1 = 3 (unit: mm) (d) Patch antenna. W_a = 9.2; L_a = 7.7; L_m = 2.6; W_s = 0.4; W_f= 2.45.(unit: mm)

Details of the proposed high-temperature sensor based on a SiCN resonator are presented as follows. As seen in Fig. 5.9, a SiCN cavity resonator is placed over CPW lines. The substrate material for the CPW line is alumina. All the dimensions are listed in Fig. 5.9. Two coupling

slots on the sidewall of the resonator are created during the metallization procedure of the SiCN resonator, which allows for the magnetic coupling between the short-ended CPW lines and resonator. For the dielectric cavity resonators studied herein, H/D < 1.015, therefore the dominant resonant mode for this resonator is TM_{010}. SMA connectors are soldered to the CPW lines for connecting the antennas.

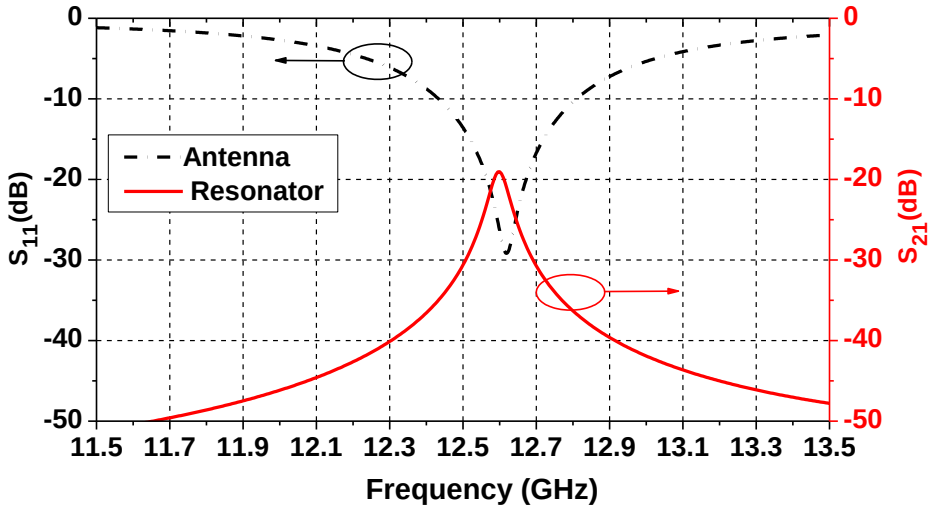

The resonant frequency of the SiCN resonator is determined by the resonator size and the dielectric constant of SiCN. When the dielectric constant of SiCN changes versus temperature, the resonant frequency of the resonator changes accordingly.

Figure 5.10:Simulated S_{11} of the patch antenan shown in Fig. 5.9(d) and S_{21} of the structure shown in Fig. 5.9(a).

A microstrip patch antenna is designed for the sensor. Fig. 5.9(d) shows the geometry of the proposed patch antenna. The antenna is fabricated on a Rogers RT/Duroid 5880 substrate with a thickness of 0.787 mm. The center frequency and bandwidth of the antenna is 12.6 GHz and

approximately 3%, respectively. The gain of this antenna is more than 8 dB over the bandwidth. The simulated antenna return loss is shown in Fig. 5.10. The transmission of the structure shown in Fig. 5.9(a) is also plotted in Fig. 5.10. It is apparent that the resonant frequency of the sensor is within the antenna bandwidth.

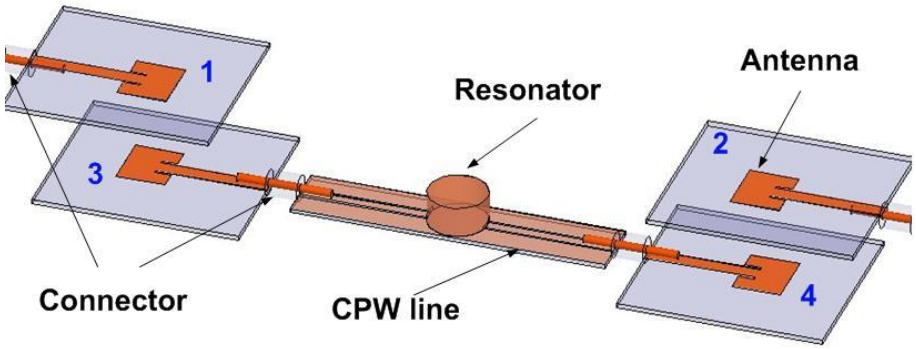

Figure 5.11:Entire wireless sensing system.

The wireless sensing system is illustrated in Fig. 5.11. The passive sensor is composed of two antennas and a SiCN cavity resonator. This sensor receives a wide-band signal from Antenna 3, which is coupled to Antenna 1. Since there is a resonator between Antennas 3 and 4, only the energy at the resonant frequency passes through this resonator and then reaches Antenna 2 via Antenna 4, representing a peak in S_{21}, as shown in Fig. 6. The distance between antennas 1 and 3 is kept the same as that between antennas 2 and 4. Although the resonator is relatively weakly coupled to the CPW lines, a peak in the transmission can still be clearly observed due to the high Q factor of the resonator [46].

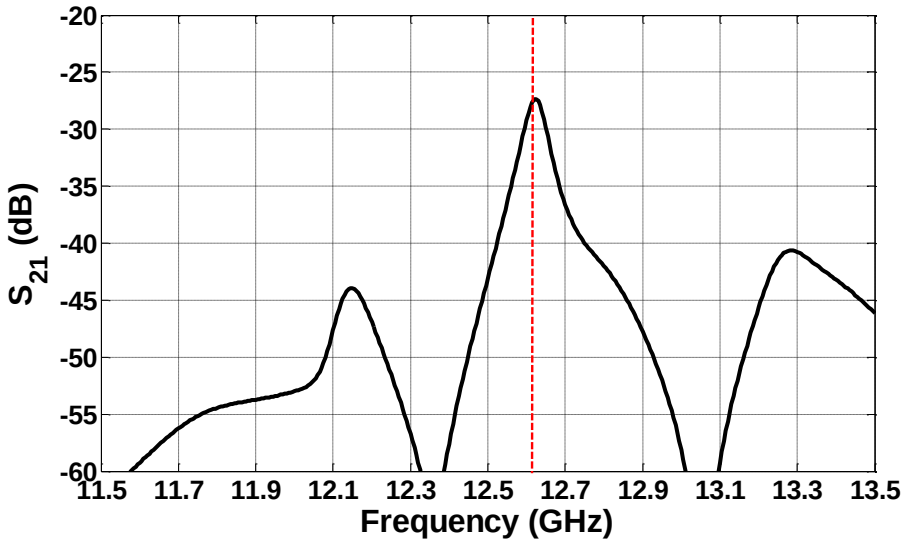

Figure 5.12:Simulation result for the sensing system at the distance of 20mm between antennas in Fig. 5.11.

5.2.3 Fabrication and Measurement up to 500^{o}C

Details about the fabrication process and measurement results are provided in this section. Fig. 5.13(a) shows the fabricated cavity resonator over the CPW line. In order to form a cavity resonator made of the SiCN ceramic material, metallization of the resonator is performed in two steps. First, a 0.3-μm-thick Cr layer is evaporated on the sample. Five evaporations from different directions are necessary to cover the entire surface of the sample. Then Au electroplating is performed to create a 7-μm-thick metal layer in order to minimize the conductor loss. During the metallization steps, the coupling slots are covered by 3 by 1 mm tapes. The CPW lines over the alumina substrate are created using the same metallization procedure and patterned using photolithography. The height and diameter of the SiCN cavity resonator is 5.01

and 9.42 mm, respectively. It should be noted that Cr/Au is used here to demonstrate the proposed wireless sensing concept. For turbine applications, Pt will be used in order for the sensors to work above 1000^{o}C. making it a promising candidate for future high-temperature sensor development. The fabricated antenna is shown in Fig. 5.13(b). Four same antennas are

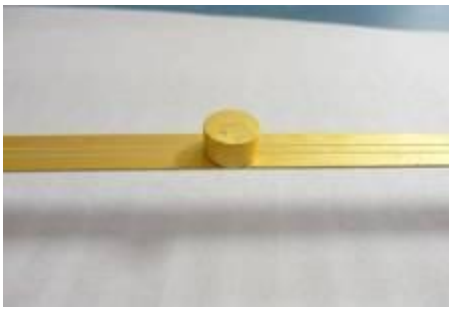

(a)

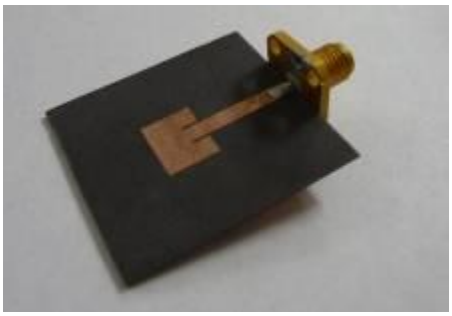

(b)

fabricated for this research.

Figure 5.13:(a) Fabricated cavity resonator over the CPW line (b) fabricated patch antenna; all four antennas are the same

The structure shown in Fig. 5.9(a) is measured and compared with simulations as shown in Fig. 5.14. The reflection coefficient of the fabricated antenna is also measured and shown in the same figure. Good agreement between the simulation and measurement has been observed.

After demonstrating the performance of resonator and antennas separately, the final wireless sensing setup is formed as shown in Fig. 5.15. Each end of the CPW lines is connected to an antenna. Those two antennas are coupled to two other antennas which are connected to the VNA. Fig. 5.16 compares the measured S_{21} for the cases with or without antennas. It is observed that

for both cases the maximum transfer of energy happens at the resonant frequency of the resonator, i.e. 12.6 GHz. It shows that we can successfully measure the resonant frequency wirelessly at the cost of about 11-dB loss. The same measurement is performed for various distances between the antenna pairs. As shown in Fig. 5.17, as the distance increases, the level of received signal decreases. Maximum sensing distance around 40 mm is achieved with this

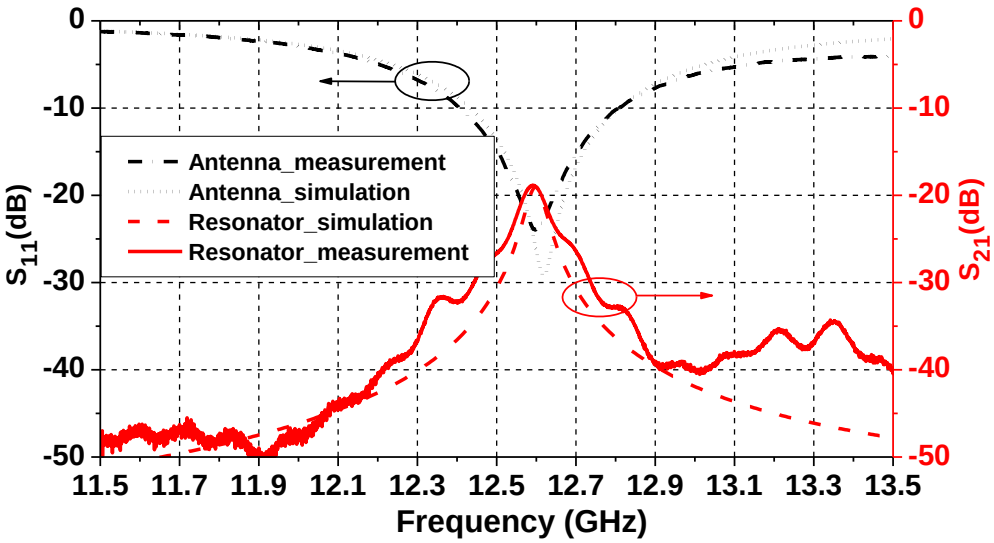

measurement setup. It should be noted that the measured loaded Q reduces from 170 down to 150 when the distance is increased from 10 up to 40 mm.

Figure 5.14:Measured and simulated S_{11} of the patch antenna shown in Fig. 9(d) and S_{21} of the structure shown in Fig. 9(a).

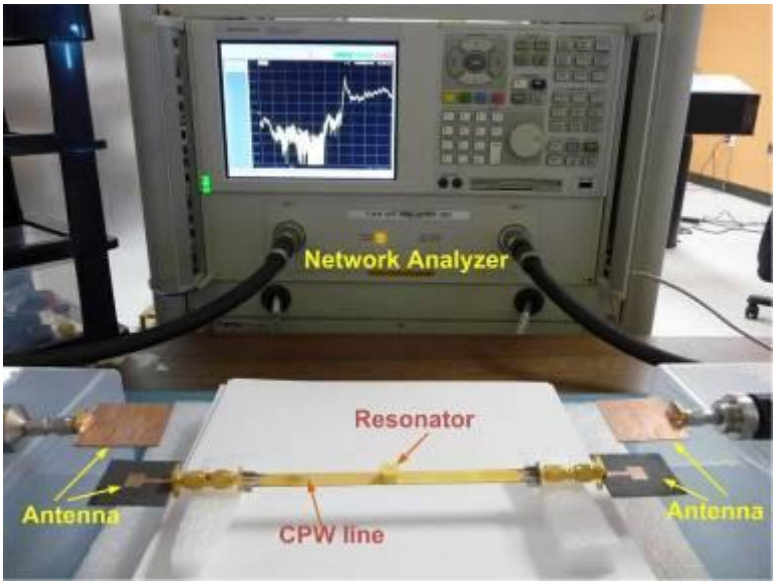

Figure 5.15: Final wireless passive sensing setup.

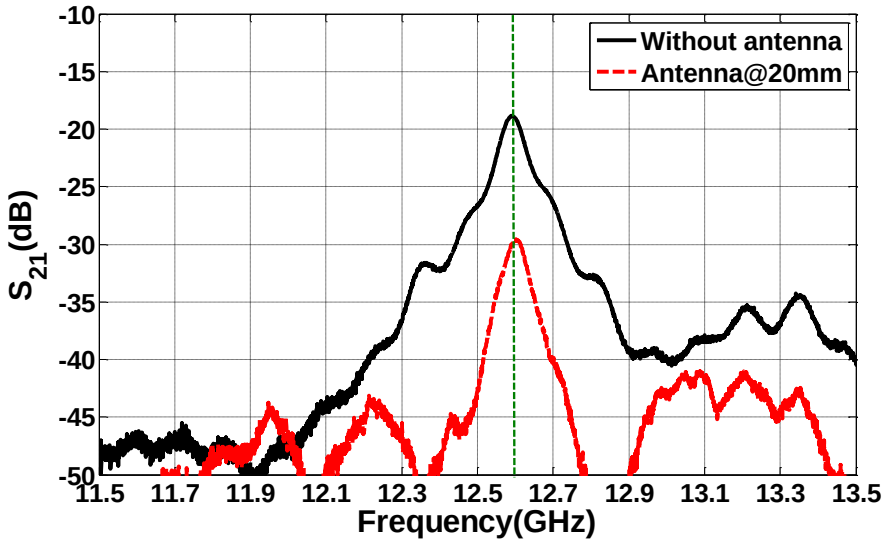

Figure 5.16: Measured S_{21} with or without the antennas.

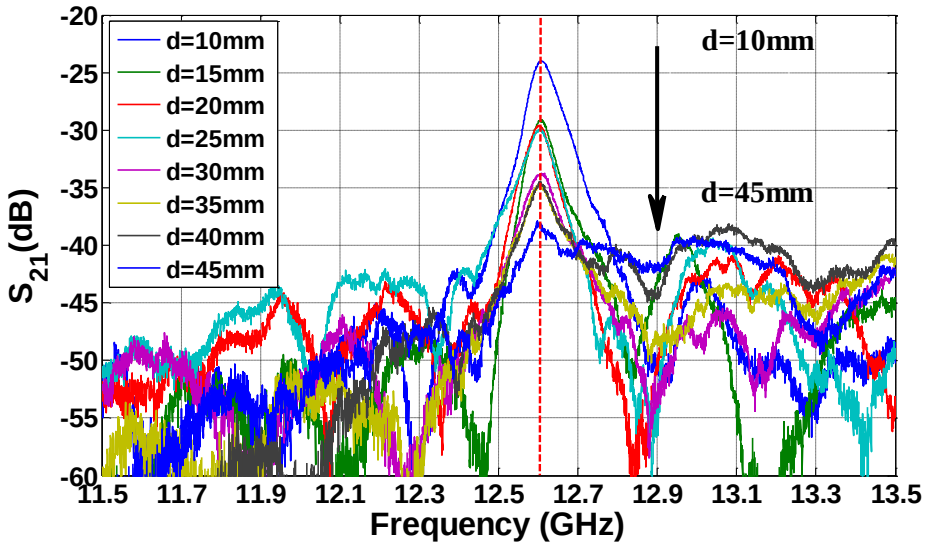

Figure 5.17: Measured S_{21} for sensing distances from 10 to 45 mm.

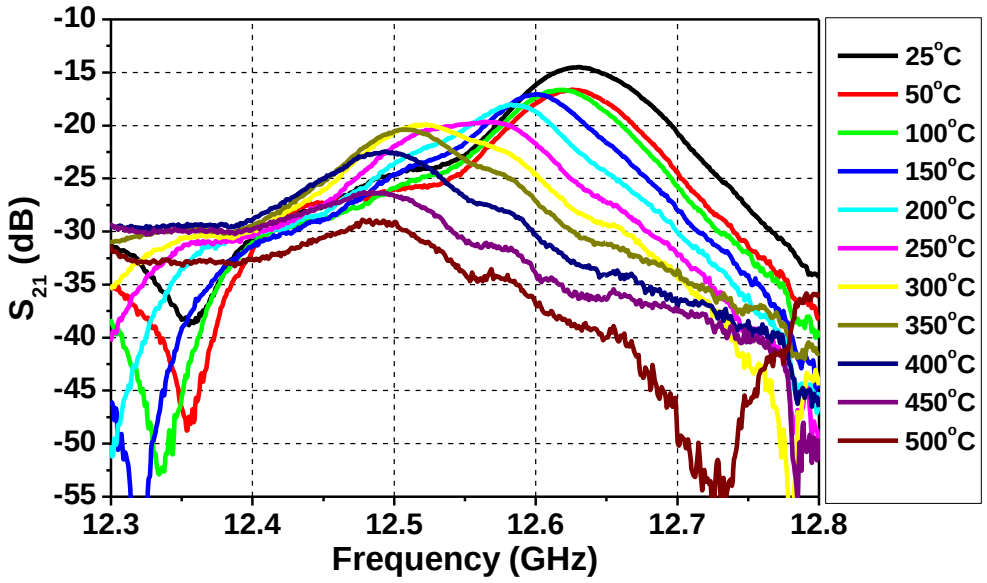

Figure 5.18: Measured S_{21} for different temperatures.

By enhancing the coupling between the resonator and CPW lines, the wireless sensing range can be further increased. To demonstrate high-temperature sensing, the CPW lines and resonator is placed inside a furnace with controllable temperature. The two ends of the CPW lines are outside the furnace at a much lower temperature, allowing for soldering SMA connectors and connecting antennas. Through calibration was done at room temperature. The results of S_{21} for different temperatures are recorded, as shown in Fig.5.18. It is observed that the resonant peak moves to lower frequency for higher temperature, which is the same as we estimated before.

5.2.4 Fabrication and Measurement up to 1000^{o}C

Higher temperature measurement up to 1000^{o}C is realized using Si_4B_1CN (1000^{o}C) sample. The measurement setup and resonator dimensions are shown in Fig. 5.19. The wider bandwidth antennas are used for covering the variation range of resonator because of the larger range of the measurement temperature. The detail of the antenna, such as dimensions will be shown in the next section. In this setup, the high temperature cable is used to connect the antennas and CPW line in order to keep the antenna at low temperature. Through calibration is done at room temperature before the measurement. The distance between a pair of face-to-face antennas was kept at 10 mm during the measurement. The temperature of the inside of furnace was increased from 25 to 1000^{o}C at the step of 50^{o}C when the temperature was over 50^{o}C. The measured S_{21} results are shown in Fig. 5.20 (a). The measurements were repeated twice. The extracted f_r, and Q_u, versus temperature are plotted in Fig. 5.20 (b) and (c).

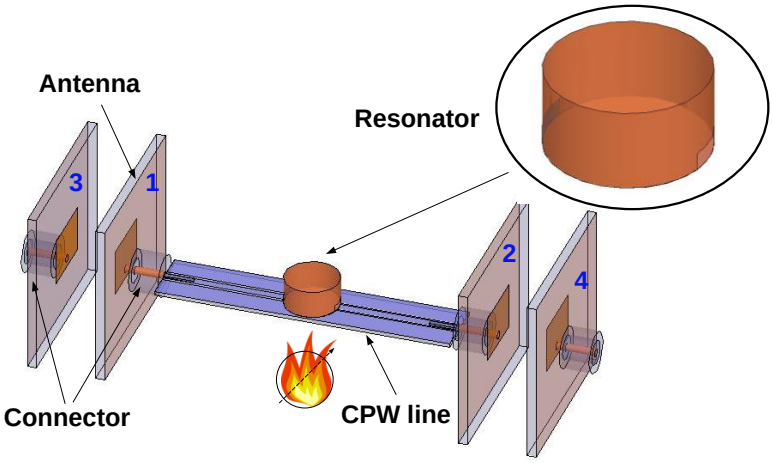

(a)

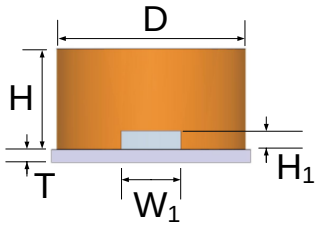

(b)

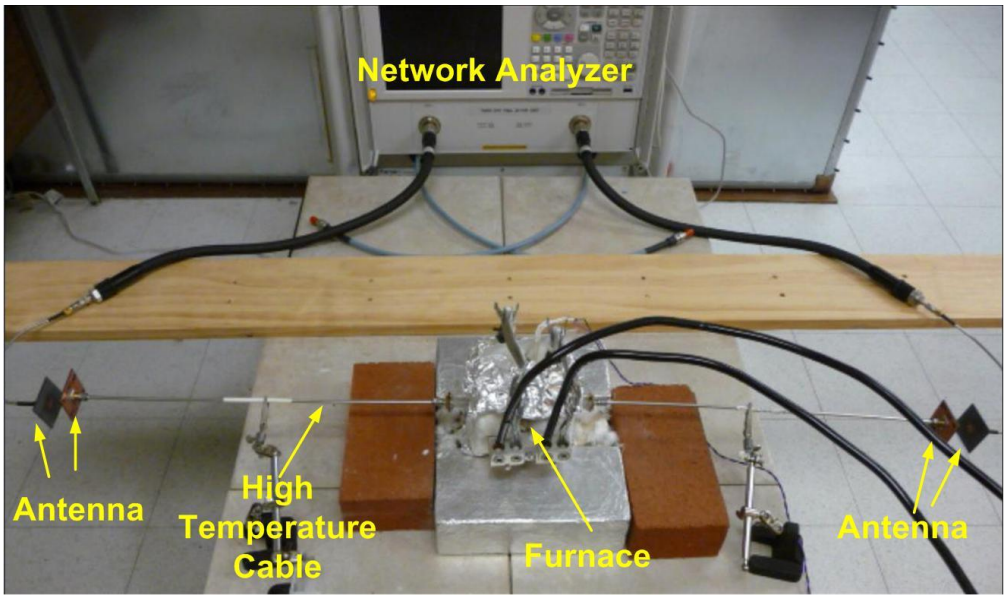

(c)

Figure 5.19: (a) Passive temperature sensor with a Si_4B_1CN (1000^{o}C) cavity resonator coupled to CPW lines, (b) side view of the sensor, and (c) wireless passive sensing setup for room temperature. T = 0.635; D = 9.37; H = 4.71; H_1 = 1; W_1 = 3 (unit: mm).

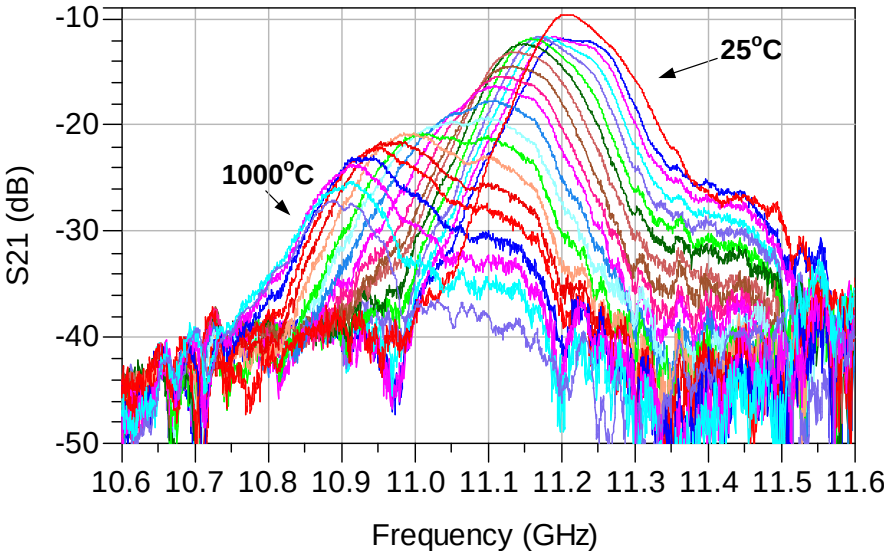

(a)

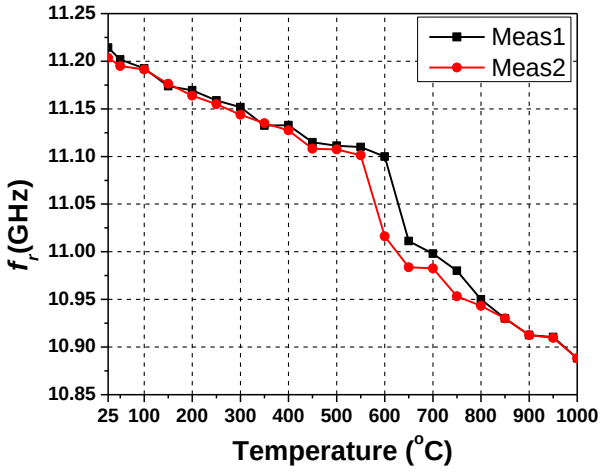

(b)

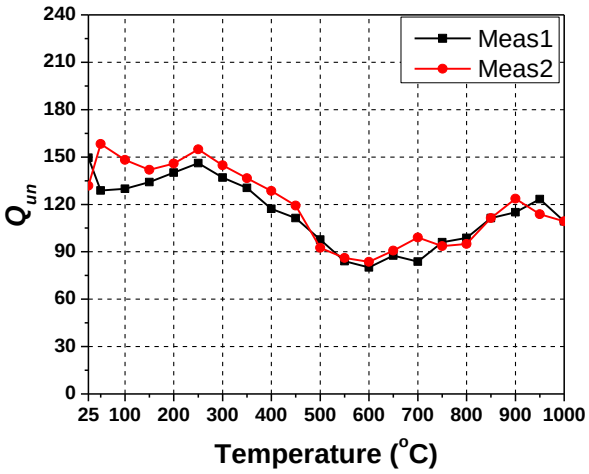

(c)

Figure 5.20: (a) Measured S_{21} for different temperatures, extracted (b) f_r and (c) Q_{un} versus temperature.

5.3 One-antenna Sensor

5.3.1 Sensor Design

In this section, a cavity resonator connected with a patch antenna is proposed to work as a wireless passive temperature sensor as shown in Fig. 5.21. The resonator is a cylindrical ceramic sample coated with a metal layer. The ceramic materials studied here is SiBCN, which is SiCN with Boron doping. The resonant frequency of this resonator sensor changes versus temperature, which is mainly determined by the temperature-dependent dielectric properties of the ceramics. This resonant frequency can be wireless detected by another patch antenna through the patch antenna connected to the resonator [47].

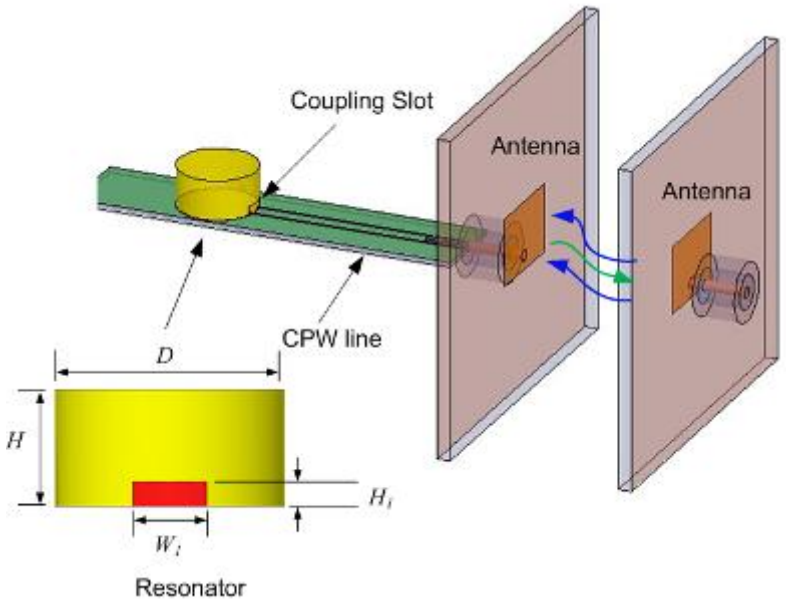

Figure 5.21: Schematic of the wireless temperature sensor. D=9.2; H=4.7; W_1=3; H_1=1 (unit: mm).

The key part of the temperature sensor is the cylindrical cavity resonator loaded with high temperature ceramics with the temperature dependent dielectric property. The resonator is metalized with Pt paste with the conductivity of 2×10^6 S/m. Due to the fabrication limitations of the dielectric material samples, the cylinder diameter and thickness are fixed at D = 9.2 mm and H = 4.7 mm, respectively. The dominant mode for this resonator is TM_{010} mode. The dielectric constant and loss tangent are 4.8 and 0.003 respectively, which are characterized at room temperature. The resonance frequency and unloaded Q factor of the closed cavity resonator can be calculated to be 11.38 GHz and 236 based on analytical equations. The slots are opened on the sidewall of the resonator for the magnetic field coupling with coplanar waveguide (CPW) line. The dimensions of slots are shown in Fig. 5.21. The CPW line is fabricated using alumina board metalized with a layer of Pt paste. The center conductor and slot of the CPW line are 1.5 and 0.4 width in mm in order to keep the characteristic impedance is nominally 50 Ω.

A microstrip patch antennas is designed for receiving and sending signals in order to make the sensor working wirelessly. The center frequency of the antenna is 11 GHz and the bandwidth is approximately 9%, which can cover the variation range of the resonant frequency of the resonator due to the change of the ambient temperature. The gain of this antenna is more than 7 dB over the bandwidth.

With the temperature increasing, the dielectric constant of SiBCN will monotonically increase. Therefore, the resonant frequency of the resonator decreases against temperature. The relationship of the resonant frequency versus temperature is the basis of the sensing mechanism in this paper. The study of the resonant frequency versus dielectric constant is done based on

HFSS simulation. In the simulation, the dielectric constant of SiBCN ceramic swept from 4.8 to 5.1, while the distance between antennas is kept as 30mm. In order to observe the resonance frequency of the resonator clearly, time-domain (TD) gating is applied to S_{11} results to identify the resonant peaks. The S_{11} results after TD gating corresponding to different dielectric constants are plotted in Fig.5.22. The peaks of S_{11} represent the resonant frequencies corresponding to different dielectric constants. The resonant frequency versus dielectric constant is extracted and plotted in Fig. 5.23. It can be noticed that the resonant frequency goes down when the dielectric constant increases [47].

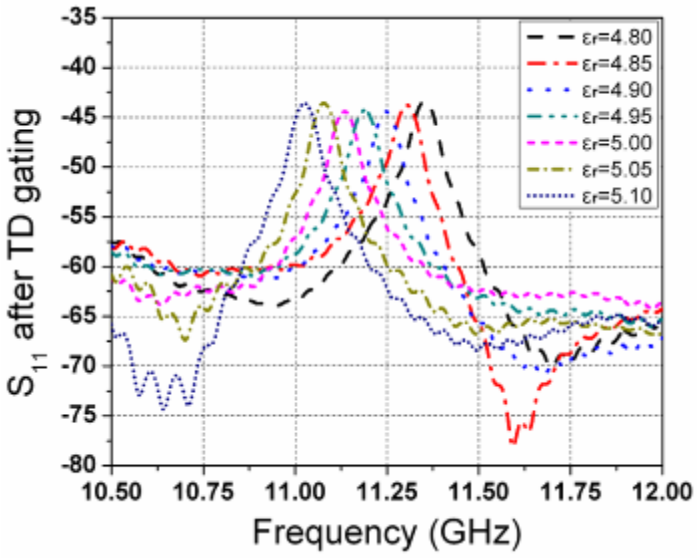

Figure 5.22: Simulated S_{11} of the patch antenna for successive distances away from the sensor *after* TD gating.

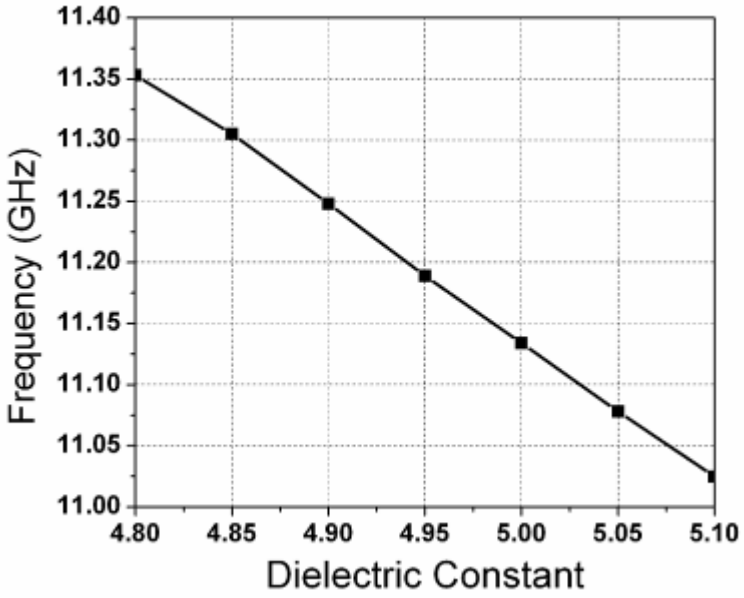

Figure 5.23: Simulated resonant frequency decreases with the increase of dielectric constant of the SiBCN material.

5.3.2 Fabrication and Measurement up to 1000^{o}C

A microstrip patch antenna is designed and fabricated for the sensor. Fig. 5.24 shows the geometry of the proposed patch antenna. The antenna is fabricated on a Rogers RT/Duroid 5880 substrate with a thickness of 62 mils. The center frequency of the antenna is 11 GH and bandwidth is approximately 9%, which covers the change range of the SiBCN resonator. The gain of this antenna is more than 7 dB over the bandwidth.

In order to form a waveguide cavity resonator, the opening slots (3×1mm) on the sidewall of the sample were covered by the tape, and then , a layer of platinum paste (ESL 5542) is applied on all the faces of the cylindrical samples. Then the samples covered by platinum paste are dried at 100ºC for 10 minutes and sintered at 1000ºC for 10 minutes. The ramp rate during the sintering is 10ºC/min. The formed platinum layer is approximately more than 30 µm thick.

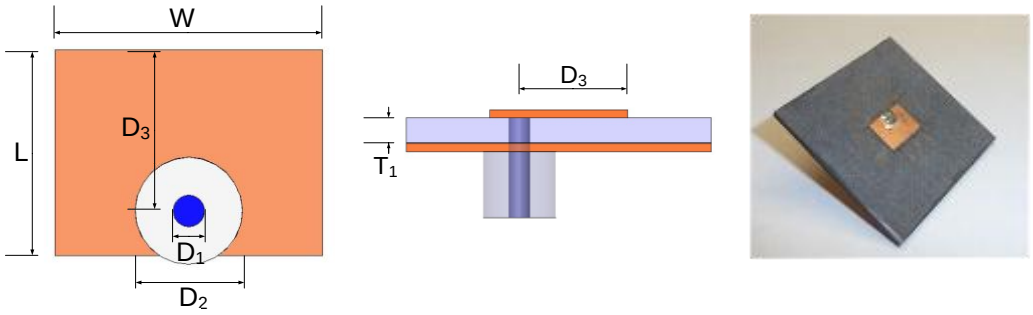

Figure 5.24:Dimensions of the patch antenna. (a) Top view, (b) Side view, and (c) Fabricated antenna. *L=8.3;W=10.8;D_1=1.27;D_2=4.32;D_3=6.5;T_1=1.57* (unit: mm).

In order to ensure the measurement setup working above 1000^{o}C, high temperature solder (91Pb4Sn4Ag1In, melting point: 313^{o}C, Indium Corporation), high temperature connectors (600^{o}C) are used. A copper holder was custom-made for better connection between the CPW line and connector. The sensor is shown in Fig.5.25 (a). A high temperature furnace is used to control the temperature of the sensor from 25 to 1000^{o}C as shown in Fig. 5.25 (b). A *K*-type thermocouple (Omega HH11) show in Fig. 5.25 (c) is used to monitor the temperature inside the heat pad and provide the feedback to the temperature controller. Antenna patch antenna is used for the wireless sensing. One port Short-Open-Load (SOL) calibration is performed at the end of

the coaxial cable and proper TD gating is applied using an Agilent 40-GHz PNA-L (N5230A). Thus, the real-time resonant frequency of the sensor can be measured wirelessly for different temperatures.

The measured S_{11} responses of the Si_4B_1CN (1000°C) temperature sensor at different temperatures is plotted in Fig. 5.26. Each curve corresponds to a single temperature in the 25-1000°C range. At each temperature, there is a unique peak with the highest signal level. This peak corresponds to the resonant frequency of the sensor. The resonant frequencies and *Q*s of the Si_4B_1CN (1000°C) sensor for temperatures from 25 to 1000°C are plotted in Fig. 5.27. The resonant frequency decreases from 11.44 to 10.99 GHz in this temperature range, which corresponds to a measured sensor sensitivity of 0.46 MHz/°C. The Q decreases from 194 at room temperature to 39 at 1000°C. As the temperature increases, Q is reduced due to the increasing loss of both ceramic and platinum. The distances between two antennas is 10 mm. The sensing distance can be increased by increasing the output power from the transmitter.

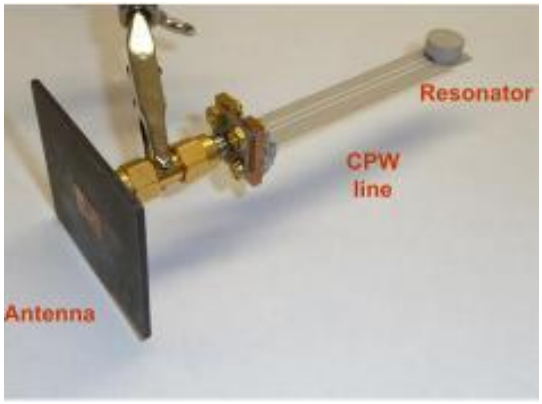

(a)

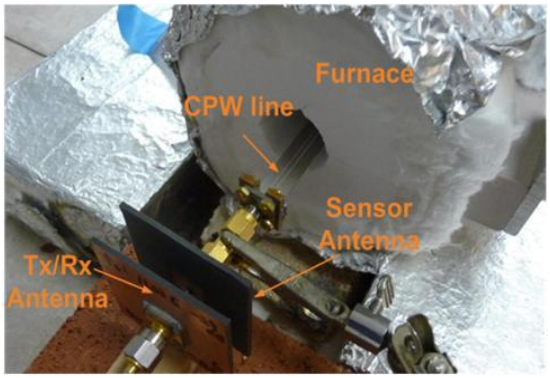

(b)

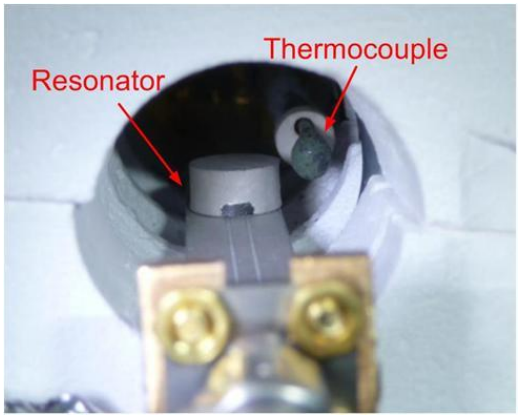

(c)

Figure 5.25: (a) Sensor outside the furnace, (b) Measurement setup with furnace, and (c) Resonator and CPW line inside the furnace.

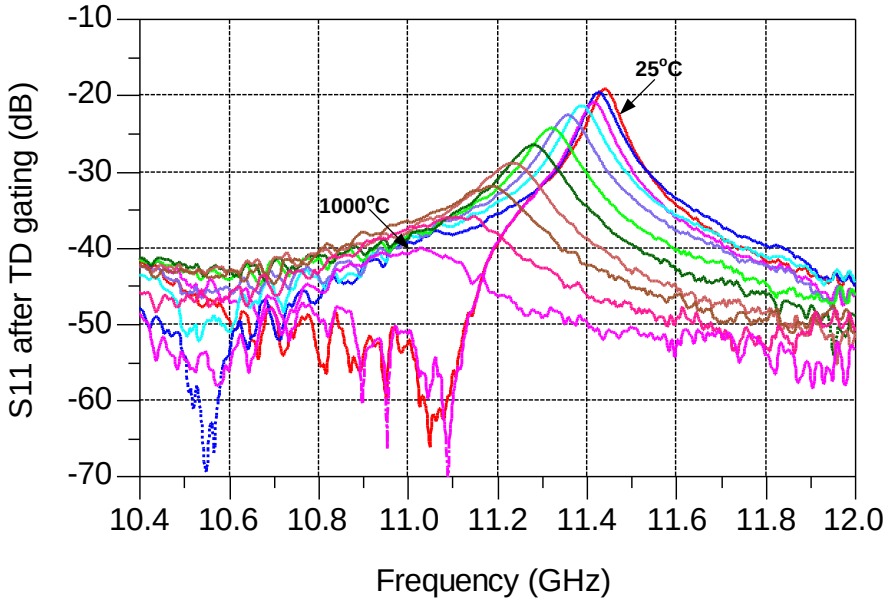

Figure 5.26:Measured S_{11} responses of the sensor at different temperatures Si_4B_1CN (1000°C).

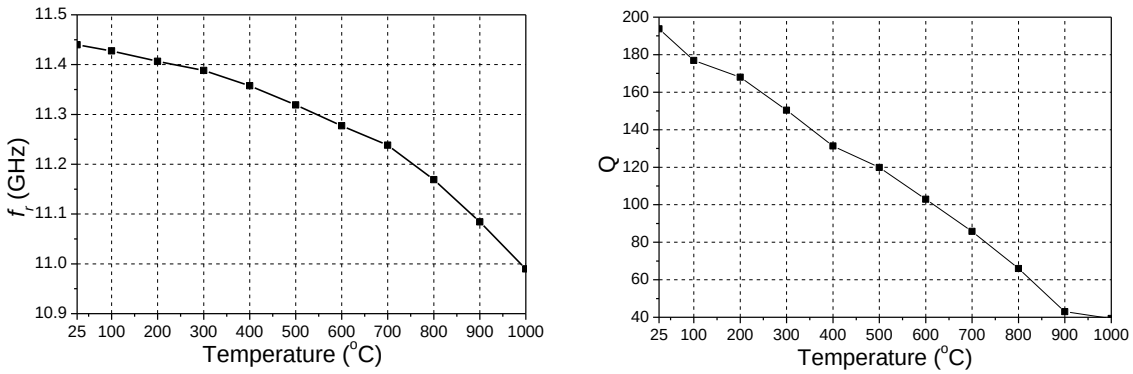

(a) (b)

Figure 5.27: Measured resonant (a) frequency and (b) Q of the Si_4B_1CN (1000°C) sensor

5.4 Integrated Slot Antenna Sensor

5.4.1 Sensor Design

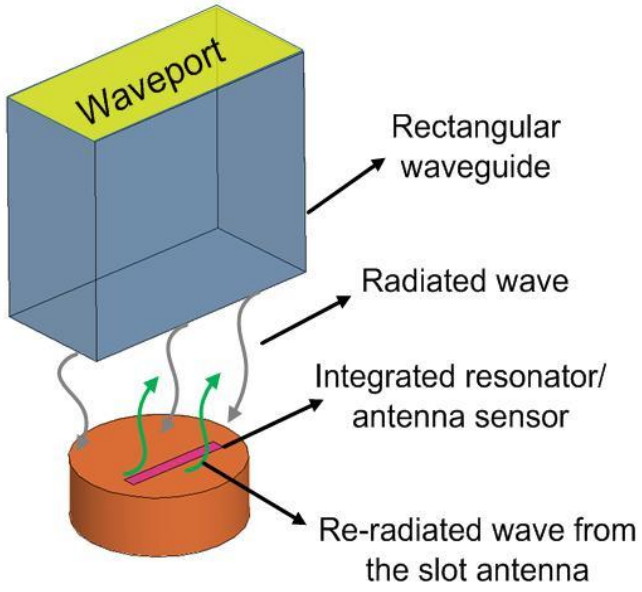

Figure 5.28:Schematic of the wireless temperature sensor.

In this section, a cavity resonator integrated with a slot antenna is proposed to work as a wireless passive temperature sensor as shown in Fig. 5.28. This cylinder resonator is formed by coating a dielectric substrate with a metal layer. The resonant frequency of this resonator sensor changes versus temperature, which is primarily determined by the temperature-dependent material properties of the substrate. This resonant frequency can be wireless detected by an open-ended waveguide (OEWG) antenna through the integrated slot antenna. The seamless integration of slot antenna and resonator, demonstrated in [48][49], is able to provide efficient energy coupling between the sensor and free space without the need of additional volume for the antenna. It is noted that this technique was also used to realize integrated filter/antennas with compact size and

high efficiency [50][51][52]. The sensing mechanism shown in Fig. 5.28 is suitable for implementation over turbine blades which function as a large ground plane.

This temperature sensor is based on a cylindrical microwave cavity resonator. Due to the fabrication limitations of the dielectric material for this sensor, the cylinder radius and thickness are fixed at a = 4.5 mm and h = 4.5 mm, respectively. The dominant mode for this resonator is TM_{010} mode and its resonant frequency is given by:

$$f_{TM010} = \frac{c}{2\pi\sqrt{\varepsilon_r}}\sqrt{(\frac{p_{01}}{a})^2} \tag{5.1}$$

In which a is the radius of the cavity resonator and p_{01} = 2.405. By setting ε_r = 5.8 and $tan\delta$ = 0.01, the fundamental resonant frequency is 10.77 GHz and unloaded Q factor Q_u is 86.6 from eigenmode simulation in HFSS.

In order to construct the wireless sensor, a slot antenna is integrated with the aforementioned cavity resonator as the Tx/Rx antenna. The simplified circuit model for the resonator/antenna is presented in Fig.5.29. R_0 shows the dissipation due to metallic and dielectric losses in the cavity resonator, while R_r indicates the radiation loss from the slot antenna. L and C, from both the resonator and the slot antenna, represent the elements for energy storage. To maximize energy coupling for the resonator through the slot antenna, the radiation Q factor Q_{rad} of the slot antenna should be equal to the unloaded Q factor Q_u of the resonator [53]:

Critical coupling requirement:

$$Q_{rad}=Q_u \tag{5.2}$$

To design the antenna for the critical coupling requirement, a weak coupling excitation of the cavity resonator is performed by two coaxial ports as shown in Fig. 5.30. These two ports affect little on the resonant frequency and will not be included in the final sensor structure. The slot antenna has the length of L_a and its position has a distance d away from the cylinder center. The loaded Q factor Q_L is simulated by the two coaxial ports in HFSS. Then the external Q factor Q_{ext} which is equal to the Q_{rad}, can be calculated by

$$Q_{ext} = \frac{Q_u - Q_L}{Q_u Q_L} \tag{5.3}$$

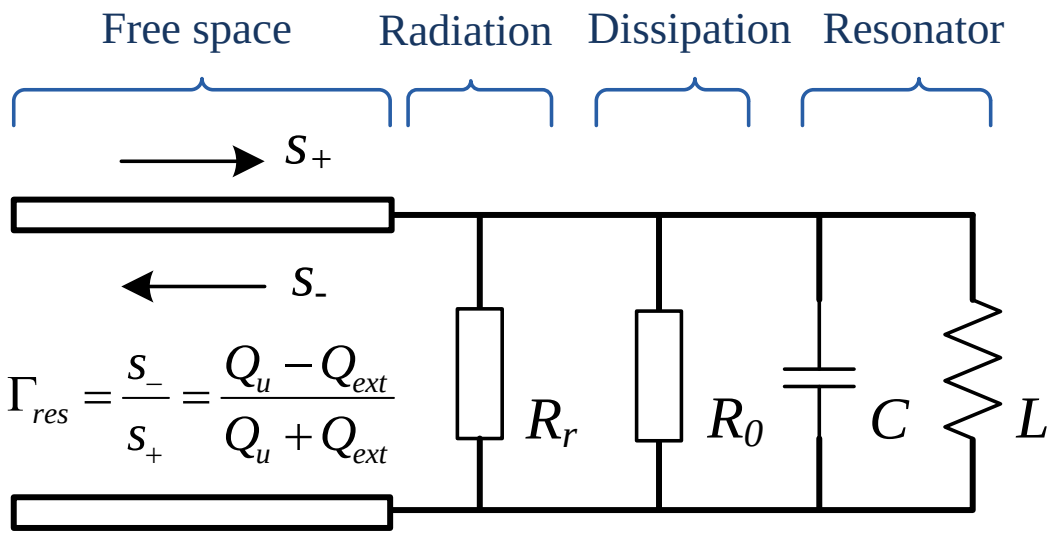

Figure 5.29:Circuit model for the integrated slot antenna/resonator.

To achieve the desired Q_{ext} value, slot position and length are considered as the variable parameters. The design curve of Q_{ext} is plotted in Fig. 5.31 for different combinations of antenna length L_a and position d. It can be observed that Q_{ext} decreases when the slot antenna becomes longer or be further away from the center. This means more current distributed on the cavity top

surface is cut off by the slot antenna, resulting in stronger radiation coupling. Finally, L_a = 6.8 mm and d = 2 mm is selected to match Q_u for maximum energy coupling.

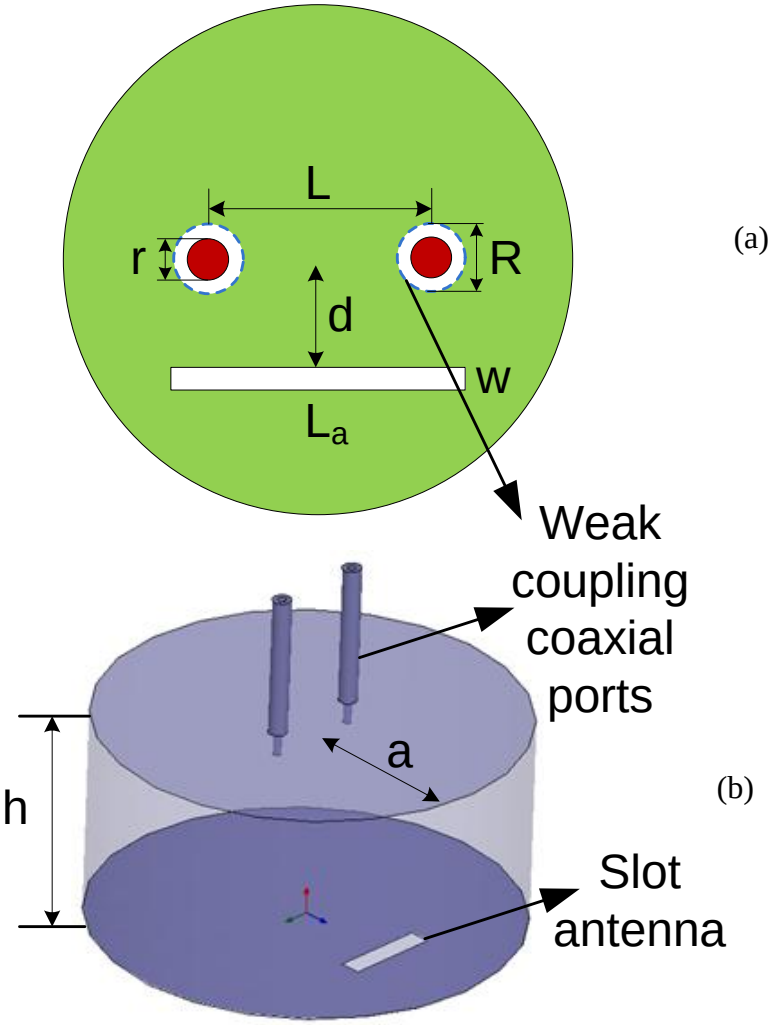

Figure 5.30:Top view (a) and 3-D view (b) of the integrated slot antenna and cavity resonator. The two coaxial ports of weak coupling are for the slot antenna design. w = 0.45 mm, r = 0.174 mm, R = 0.4 mm and L = 2 mm.

At this level, the design is finalized and the sensor's dimensions are fixed. To detect the resonant frequency of the sensor wirelessly, an *X*-band (8-12 GHz) open-ended waveguide (OEWG) is used as the interrogator antenna, which exhibits a gain of 6 dBi around 10 GHz. Fig. 5.32 plots simulated S_{11} responses for successive sensing distances between the OEWG and sensor. The resonant behavior of the sensor is difficult to distinguish due to superimposition of reflections from the OEWG, scatterings from the sensor structure, and the re-radiated waves from the resonator. Therefore, it is necessary to apply time-domain (TD) gating to isolate the response from the sensor itself.

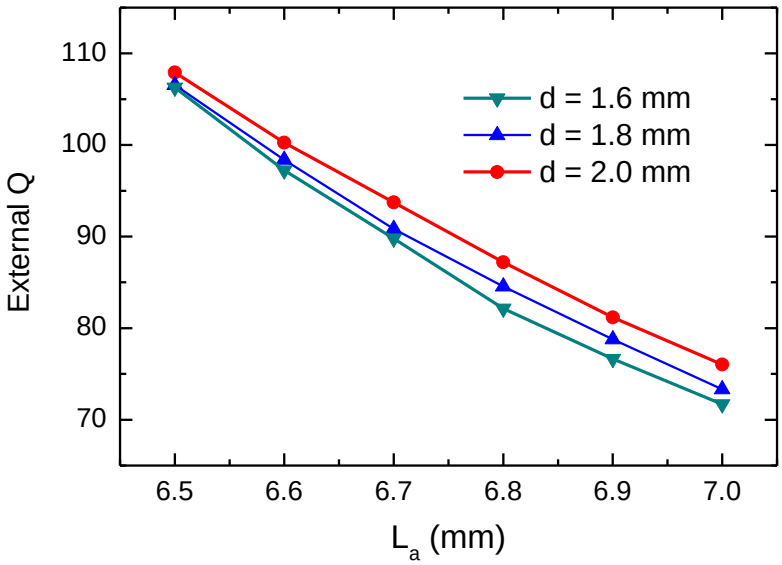

Figure 5.31:Simulated external Q factor for different slot antenna positions *d* and length L_a.

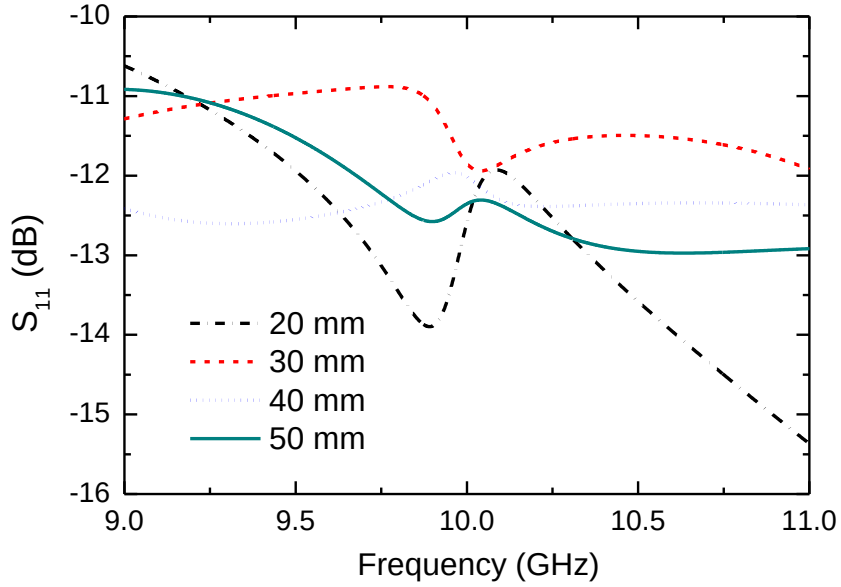

Figure 5.32:Simulated S_{11} of the OEWG for successive distances away from the sensor *before* TD gating.

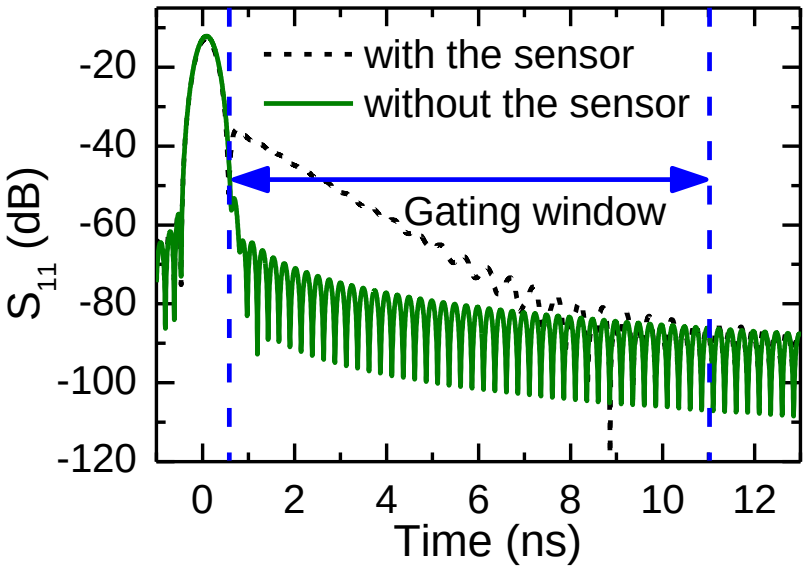

Figure 5.33:Simulated TD responses of OEWG with and without the sensor for 20 mm distance.

The S_{11} responses of the OEWG with and without the sensor are compared in time domain in Fig. 5.33 for a sensing distance of 20 mm. The main peak right after 0 ns is due to the reflection at the open aperture of the OEWG. For the case without the sensor, S_{11} quickly drops to the noise floor. When the sensor is present, it absorbs the incident wave from the OEWG and then re-radiates back to the OEWG in a periodically decaying manner. A gating window should be defined to isolate the response from the sensor. For a sensing distance of 20 mm, the gating start time is set to be 0.7 ns. The gating stop time is set to be larger or equal to 11 ns where the two curves in Fig. 5.33 intersect each other. Similar gating procedures are carried out for different sensing distances of 30, 40 and 50 mm.

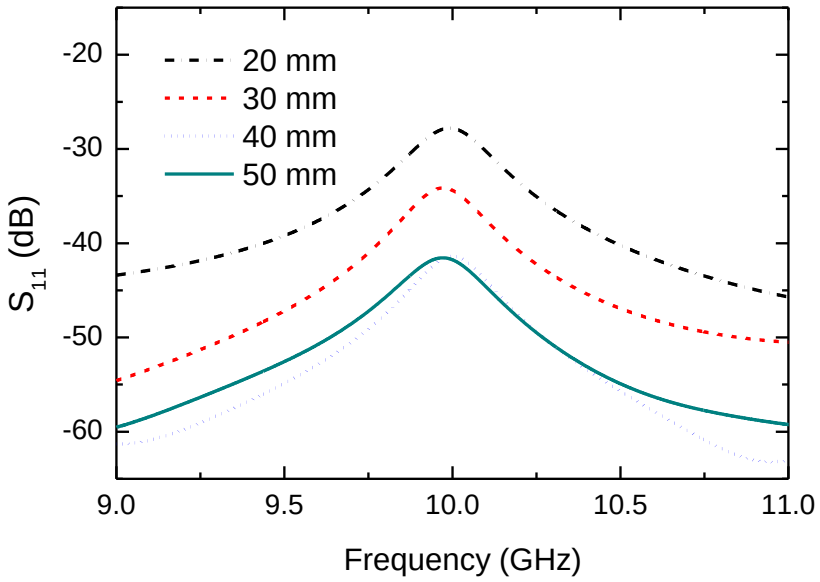

Figure 5.34:Simulated S_{11} of the OEWG for successive distances away from the sensor *after* TD gating.

Finally, TD-gated signals are transformed back into frequency domain and shown in Fig. 5.34. The resonant frequency of the sensor can be clearly identified and is independent of the sensing

distance. Compared with resonant frequency of 10.77 GHz for the resonator without the slot, the resonant frequency for the sensor is reduced to 9.99 GHz by the loading effect from the slot. The Q_L value of 44.6 is consistent with antenna design for critical coupling and the mismatch can be neglected, even though the Q_{ext} and Q_u are simulated at different frequencies. The maximum sensing range between the interrogator antenna and the sensor is 80 mm by simulation.

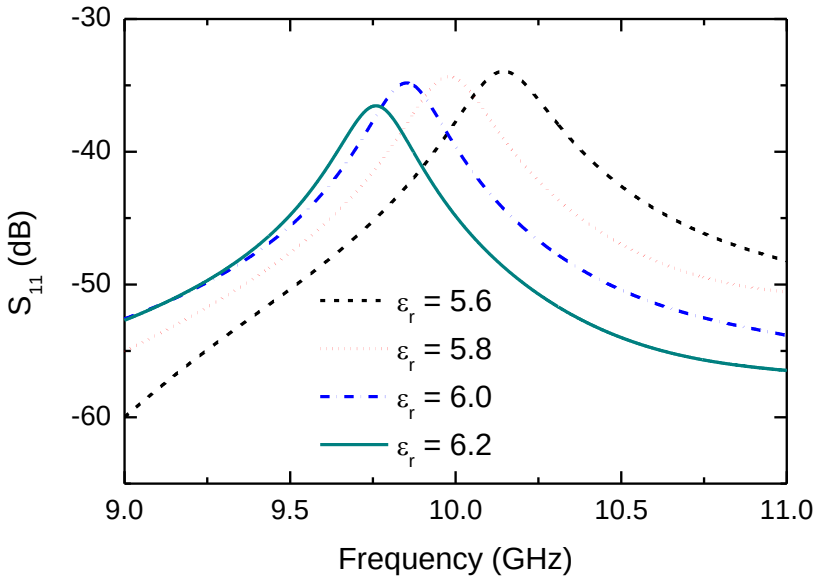

Figure 5.35:Simulated resonant frequency decreases with the increase in dielectric constant of the SiCN material.

When the temperature increases, the dielectric constant of SiCN will monotonically increase. Therefore, the resonant frequency of the resonator decreases against temperature. This resonant frequency and temperature relationship is the basis of the sensing mechanism for the wireless passive sensors presented herein. The dielectric constant of SiCN ceramic is swept from 5.3 to 5.8 in HFSS simulations to prove the concept. The S_{11} responses of the OEWG after TD gating

are plotted in Fig.5.35 for different dielectric constants. The downshift tendency of resonant frequency is shown in Fig.5.36.

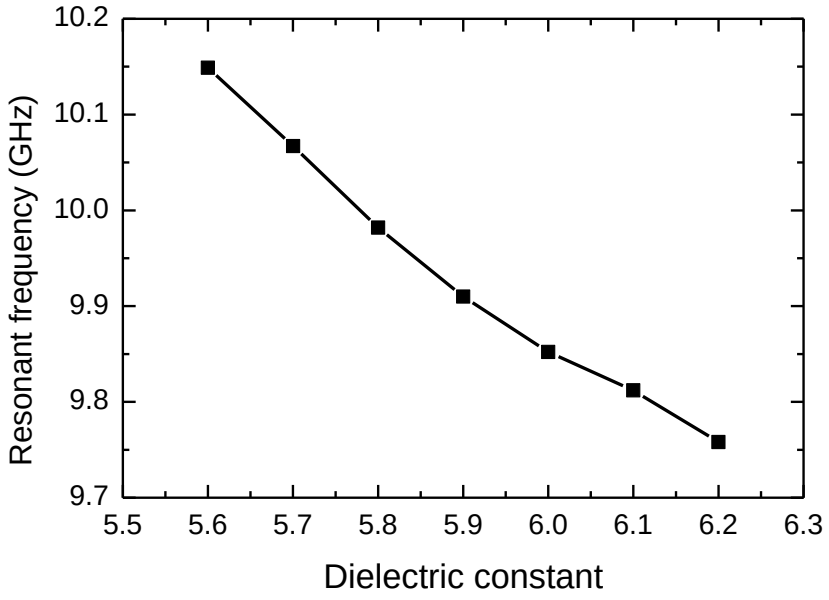

Figure 5.36:Simulated resonant frequency decreases with the increase in dielectric constant of the SiCN material for 30 mm distance

5.4.2 Fabrication and Measurement up to 1000^{o}C

Two sensors are fabricated and measured in this study. One is made of Si_6B_1CN (sintered 1000^{o}C) and another is made of Si_4B_1CN (sintered 1100^{o}C). In order to form a waveguide cavity resonator, a layer of platinum paste (ESL 5542) is applied on all the faces of the cylindrical samples. Then the samples covered by platinum paste are dried at 100ºC for 10 minutes and sintered at 1000ºC for 10 minutes. The ramp rate during the sintering is 10ºC/min. The formed platinum layer is approximately more than 30 µm thick. The slot antenna is formed on the top

surface of the cavity by milling process as shown in Fig. 5.37. The fabricated sensors with dimensions are shown in Fig. 5.38.

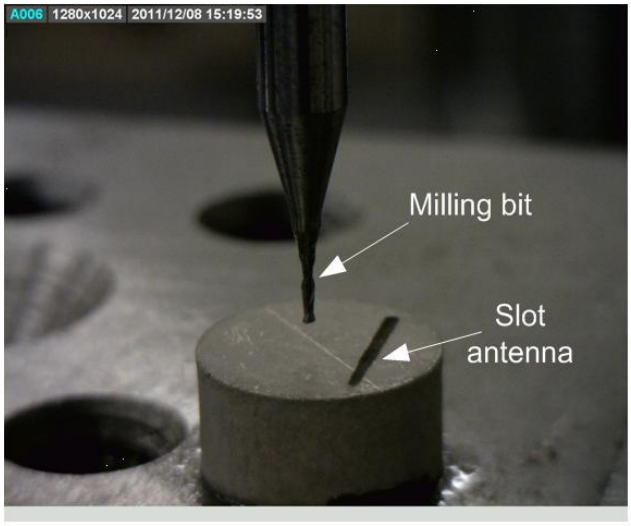

Figure 5.37:Slot antenna fabrication by milling

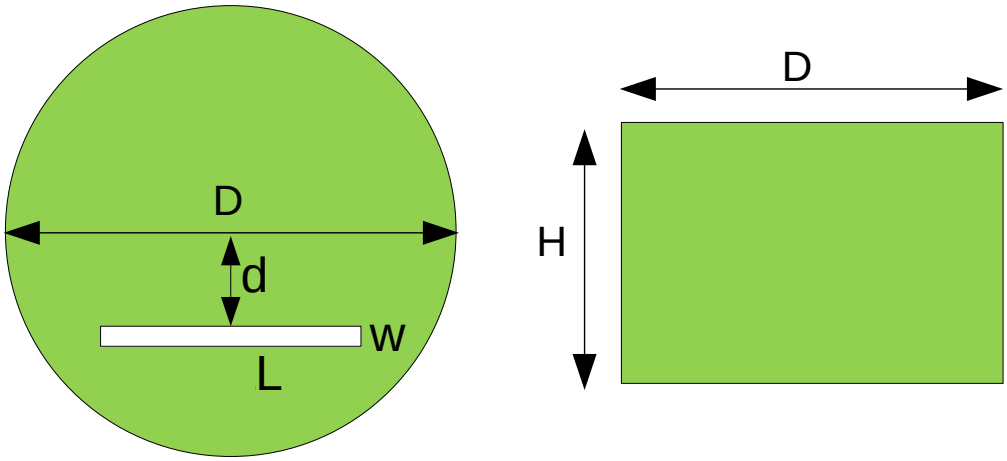

(a) (b)

Figure 5.38: (a)Top and (b) side views of the sensor and dimensions. (Si_6B_1CN (1000^{o}C): D=8.59, H=4.48, d=2.0, w=0.45, L=6.8; Si_4B_1CN (1100^{o}C): D=9.24, H=4.82, d=2.0, w=0.45, L=7.0) (unit: mm)

A heat pad with the diameter of 2 inches (Micropyretics Heaters International Inc.) is used to control the temperature of the sensor from 25 to 1050ºC/1150^{o}C as shown in Fig. 5.39(a). A piece of alumina board is placed over the heat pad to prevent air convection and stabilize the temperature of the sensor as shown in Fig. 5.39(b). A *K*-type thermocouple (Omega HH11) show in Fig. 5.39 (c) is used to monitor the temperature inside the heat pad and provide the feedback to the temperature controller.

The *X*-band open-end waveguide (OEWG) is used for the wireless sensing. One port Short-Open-Load (SOL) calibration is performed at the end of the coaxial cable and proper TD gating is applied using an Agilent 40-GHz PNA-L (N5230A). Thus, the real-time resonant frequency of the sensor can be measured wirelessly for different temperatures.

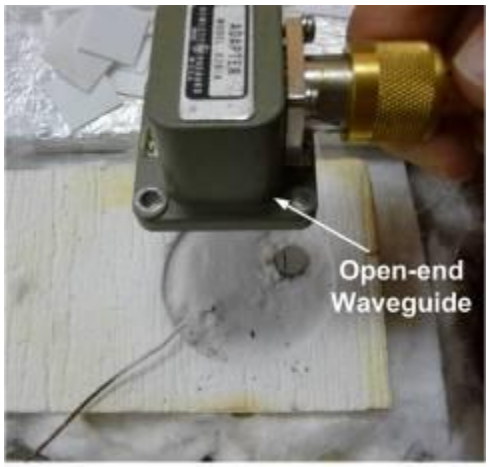

(a)

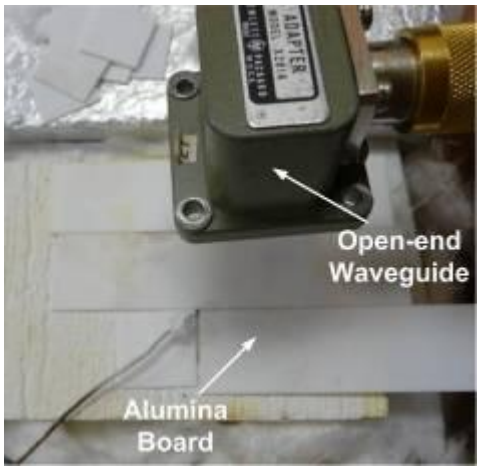

(b)

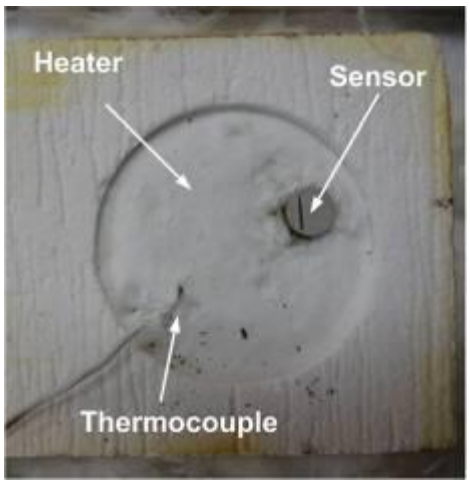

(c)

Figure 5.39: (a) Measurement set-up (b) The sensor is placed inside the heat pad with alumina board cover. (c) Inside of the heater without alumina board cover.

The measured S_{11} responses of the OEWG at different temperatures for Si_6B_1CN (sintered 1000°C) and Si_4B_1CN (1100°C) temperature sensors are plotted in Fig. 5.40. Each curve corresponds to a single temperature in the 25-1050/1150°C range. At each temperature, there is a unique peak with the highest signal level. This peak corresponds to the resonant frequency of the sensor. The resonant frequencies and *Q*s of the Si_6B_1CN (sintered 1000°C) sensor for temperatures from 25 to 1050°C are plotted in Fig. 5.41. The resonant frequency decreases from 11.05 to 10.71 GHz in this temperature range, which corresponds to a measured sensor sensitivity of 0.33 MHz/°C. The Q decreases from 82 at room temperature to 30 at 1050°C. For the Si_4B_1CN (sintered 1100°C) sensor was measured from room temperature to 1150°C. The resonant frequencies and *Q*s of this sensor for this temperature range are plotted in Fig. 5.42. The resonant frequency decreases from 10.39 to 10.06 GHz in this temperature range, which corresponds to a measured sensor sensitivity of 0.30 MHz/°C. The Q decreases from 52 at room temperature to 25 at 1050°C. As the temperature increases, Q is reduced due to the increasing loss of both ceramic and platinum. The distances between the OEWG and Si_6B_1CN (sintered 1000°C) and Si_4B_1CN (1100°C) temperature sensors are 20 and 10 mm, respectively. The sensing distance can be increased by increasing the output power from the transmitter.

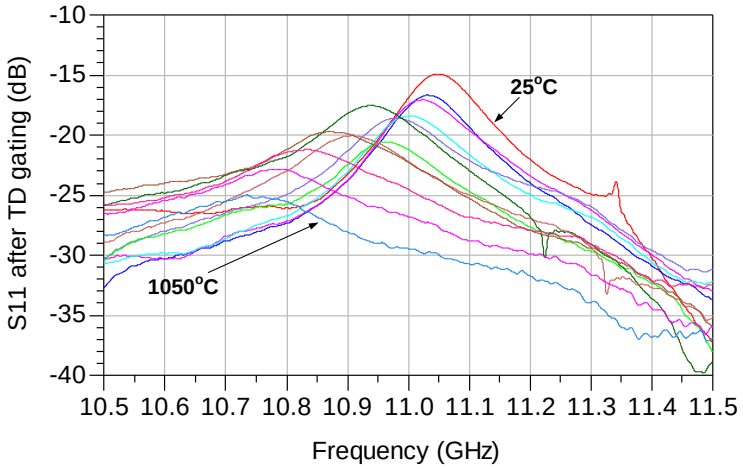

(a)

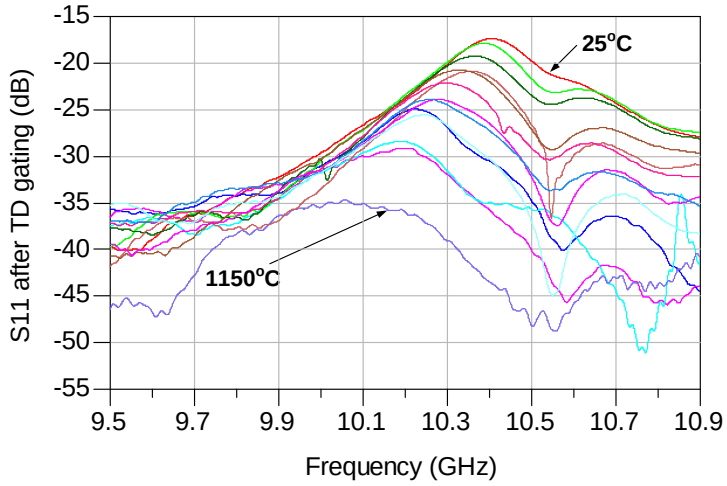

(b)

Figure 5.40:Measured S_{11} responses of the OEWG at different temperatures for (a) Si_6B_1CN (1000°C) and Si_4B_1CN (1100°C).

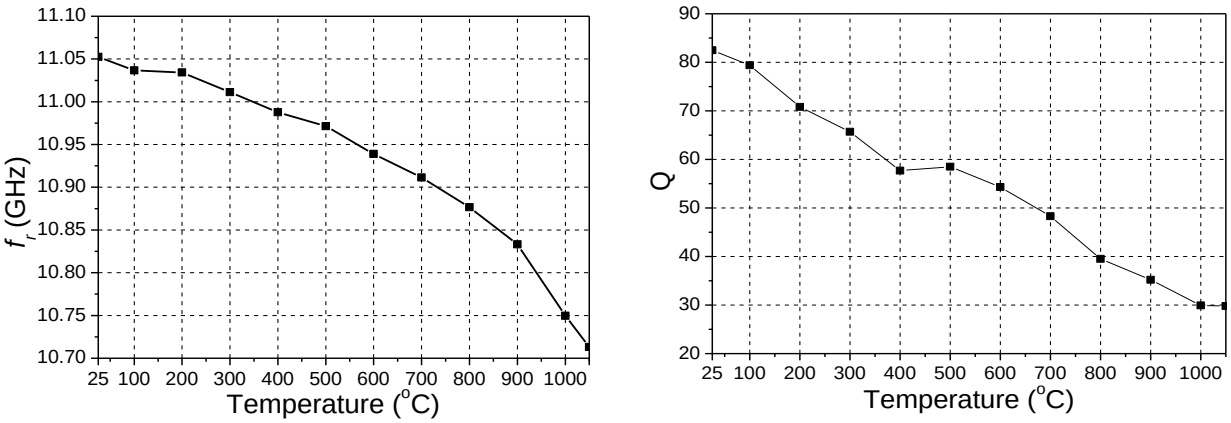

Figure 5.41:Measured resonant frequency and Q of the Si_6B_1CN (1000^{o}C) sensor

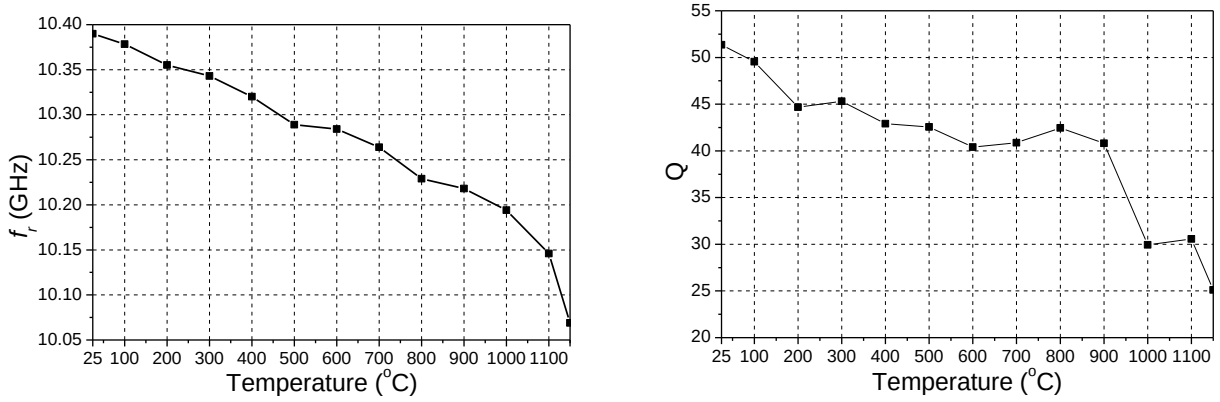

Figure 5.42:Measured resonant frequency and Q of the Si_4B_1CN (1100^{o}C) sensor

5.4.3 Fabrication and Measurement up to 1300^{o}C

Because the heat pad which was used to control the temperature of the sensor is thin (1.77 cm) and the heat zone is close to the air, it is hard to achieve the higher temperature and the

temperature is limited at 1150^{o}C. Therefore, the furnace which is used for the materials characterization has to be employed for measuring sensors at higher temperatures.

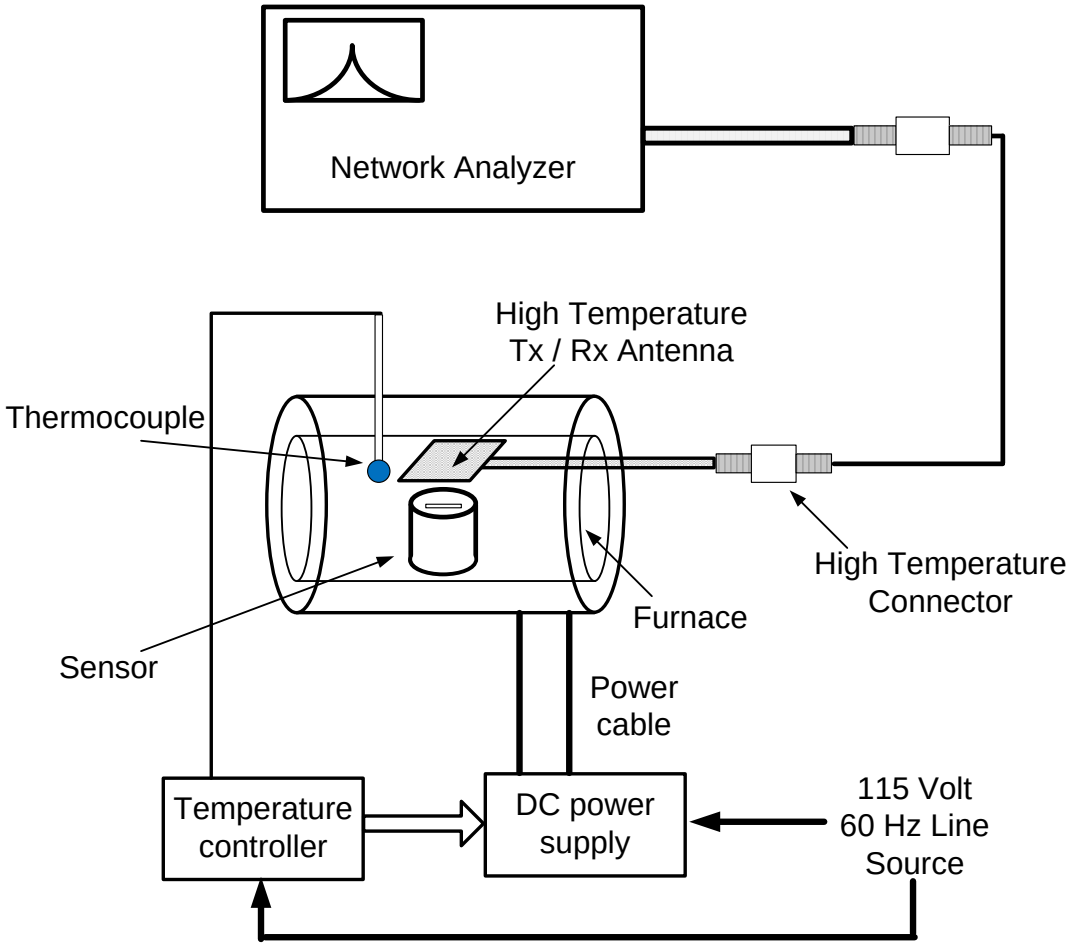

Figure 5.43:Schematic of the measurement setup for the slot antenna sensor

The schematic of the measurement setup is shown in Fig. 5.43. The furnace is the same as the one we used for the material characterization. It can rearch the temperature as high as 1500^{o}C with a high accuracy of ±2^{o}C. The sensor and antenna are in the furnace. The two ends of the

furnace would be sealed using alumina wool during the measurement. Therefore, the temperature inside the furnace is pretty stable. The antenna is connected to the network analyzer through a high temperature cable. The measured results of S_{11} can be read from the network analyzer. However, the *X*-band open-end waveguide can not be directly put into the furnace, because its structure is bulky. In addition, it can not stand in the high temperature due to its low melting point metal. So, the high temperature antenna is needed. The high temperature antenna we will use for the measurement is fabricated on the alumina substrate (0.635 mm in thickness) with the metal of Pt. The dimension of the designed antenna is shown in Fig.5.44 (a). Fig. 5.44 (b) shows the simulated S_{11} of the antenna. The center frequency of the antenna is 10.5 GHz and its bandwidth is 20.2%, which can cover the range of the temperature dependant resonant frequency of the sensor.

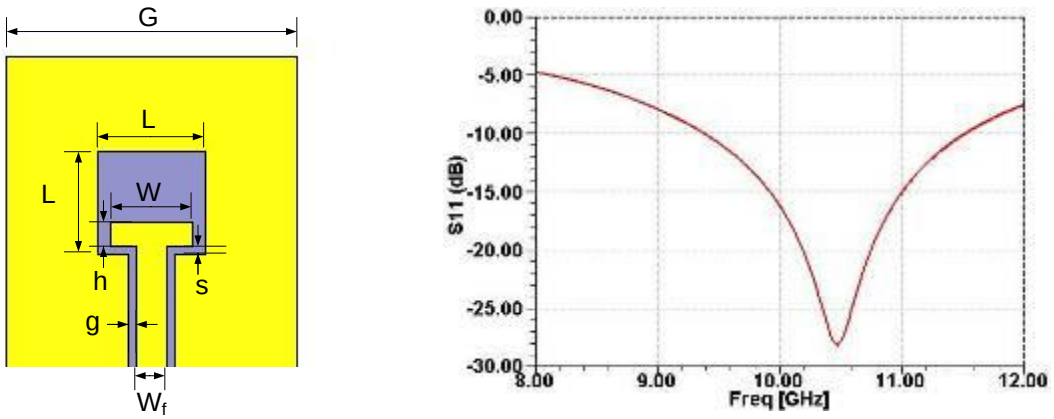

(a) (b)

Figure 5.44:(a) Dimension and (b) simulated S_{11} result of the antenna. *G=23; L_1=8.4; L_2=8; W=6.4; h=1.9; s= 0.6; W_f=2.5.* (Unit: mm)

In order to check the feasibility of this method, a PCB version of the antenna is fabricated and tested at the room temperature. Rogers 3010 is chosen as the substrate, of which the dielectric constant (10.2) is close to the one (9.6) of the alumina. The fabricated antenna and the sensor are shown in Fig. 5.45 (a). The measured result is plotted in Fig. 5.45 (b). It shows the resonant peak is at 10.53 GHz, which is the same as the previous measurement result. This method works.

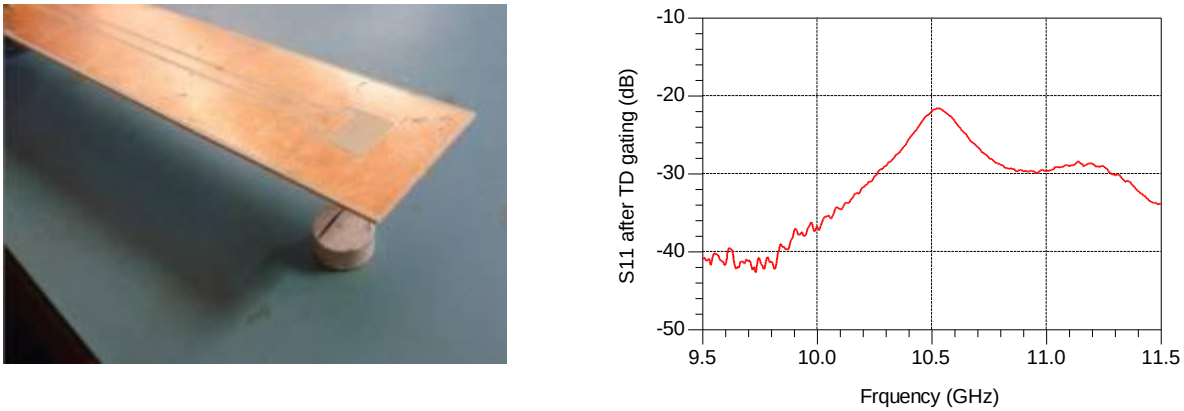

(a) (b)

Figure 5.45:(a) Fabricated PCB antenna and the high temperature sensor and (b) measurement result.

The next step is to fabricate the high temperature antenna. First, the outline of the antenna is printed onto the alumina board and a layer of Pt paste (ESL 5542) is painted to form the antenna pattern. Then, the alumina board covered by platinum paste are dried at 100ºC for 10 minutes and sintered at 1000ºC for 10 minutes. The ramp rate during the sintering is 10ºC/min. This metallization process needs to be repeated at least three times in order to form the enough thickness of the Pt. At last, Pt layer is approximately more than 30 μm thick. Fig. 5.46 shows the fabricated antenna. The measured S11 response of this antenna is plotted in Fig.5.46 (b). The

bandwidth is from 9.57GHz to 10.66GHz, which covers the variation range of the temperature dependant resonant frequency of the sensor.

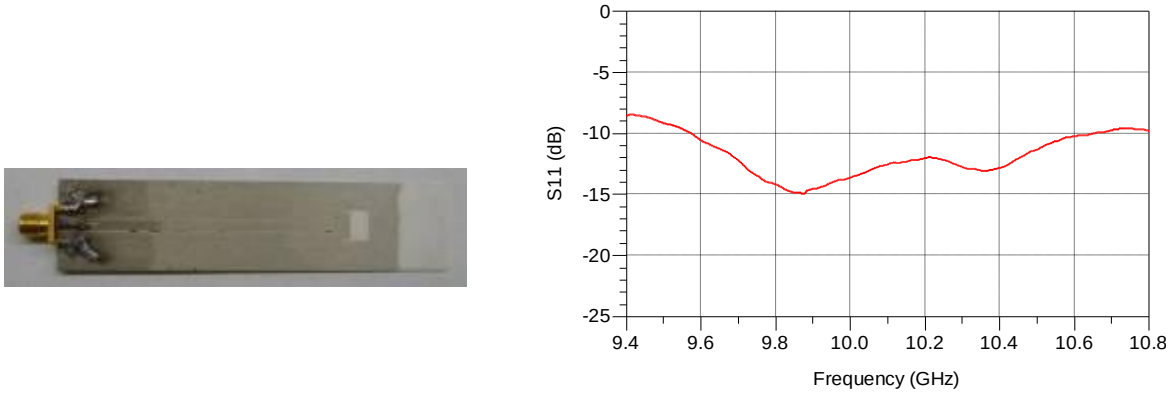

(a) (b)

Figure 5.46: (a) Fabricated high temperature antenna and (b) S_{11} response of the antenna

Fig. 5.47 illustrates the measurement setup. The high temperature antenna is over the top of the sensor and used for the wireless sensing, as shown in Fig. 5.47 (a). The distance between them is kept at 5 mm. One and half inches of the CPW line of the antenna stretches outside the furnace, so the connector at the end of the antenna feed line is at the low temperature. The inside of furnace is shown in Fig. 5.47 (b). The sensor, antenna and K-type thermocouple are in the hot zone of the furnace, where the temperature can be up to 1500^{o}C.

The measurement is performed from 25 to 1300^{o}C. One port Short-Open-Load (SOL) calibration is done at the end of the coaxial cable, which is connected to the high temperature antenna. The proper time domain gating is applied onto the measured S parameters. The measured S_{11} results of high temperature antenna at different frequency for Si_4B_1CN (1100^{o}C) sensor are plotted in

Fig.5.48. Each curve represents a S_{11} response at one temperature in the 25-1300^{o}C range. There is a unique peak at the highest signal level. This peak corresponds to the resonant frequency of the sensor. As temperature increases, the resonant frequency and signal level decrease. Above the temperature of 1300^{o}C, the resonant peak is hard to be observed. According to the temperature dependant property of the materials, the resonant frequency of the sensor is expected to decrease monotonously with temperature. However, the resonant frequency at 1350^{o}C is higher than that at 1300^{o}C, as shown in Fig. 5.49. Because the loss of the Si_4B_1CN (1100^{o}C) material and platinum becomes larger with higher temperature, the re-radiated signal from the sensor becomes weaker. Therefore, the ripples appear on the S_{11} curve due to noise. It becomes harder to detect the resonant frequency at the temperature above 1300^{o}C.

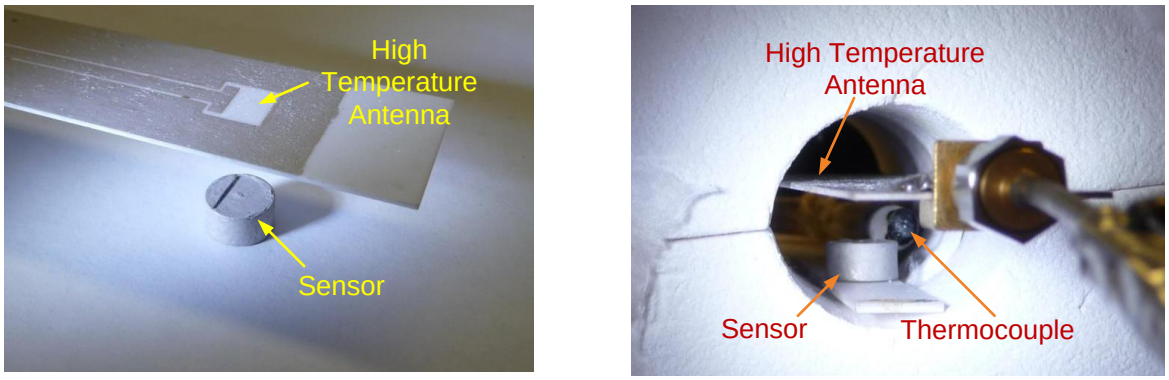

(a) (b)

Figure 5.47:Si_4B_1CN (1100^{o}C) sensor and high temperature antenna (a) outside the furnace and (b) inside the furnace.

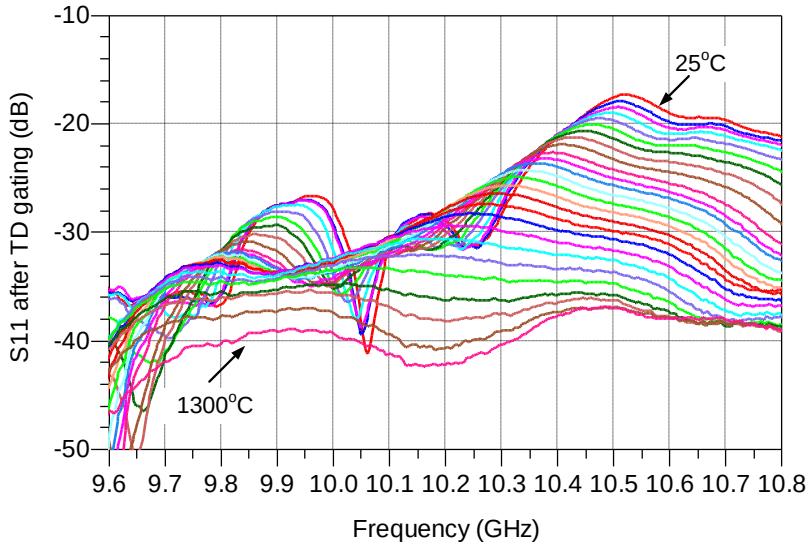

Figure 5.48:Measured S_{11} responses of the Si_4B_1CN (1100°C) sensor at different temperatures.

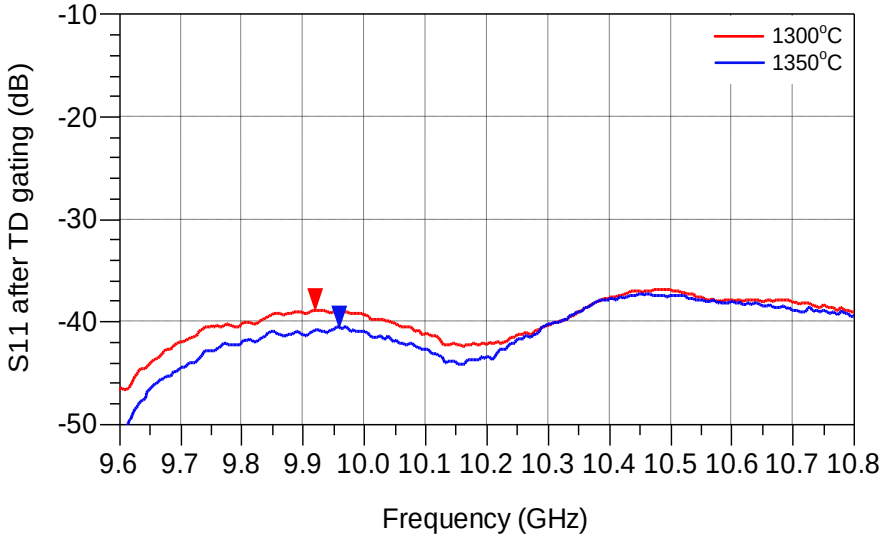

Figure 5.49:Comparison between measured S_{11} responses of the Si_4B_1CN (1100°C) sensor at 1300°C and 1350°C.

The resonant frequencies and *Q*s of this sensor are extracted and plotted in Fig. 5.50. The resonant frequency decreases from 10.52 to 9.92 GHz in the temperature range of 25-1300^{o}C, which corresponds to a measured sensor sensitivity of 0.47 MHz/^{o}C. The highest Q is 34 at room temperature and the lowest Q is 10, which is observed at 1200^{o}C.

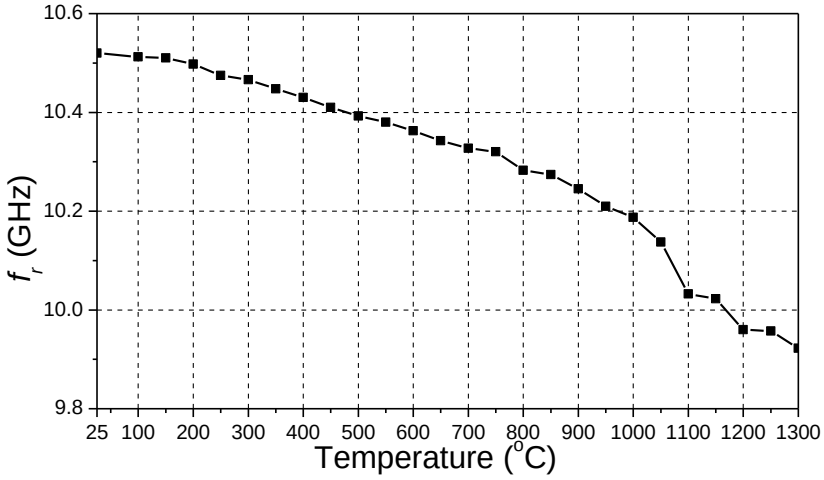

(a)

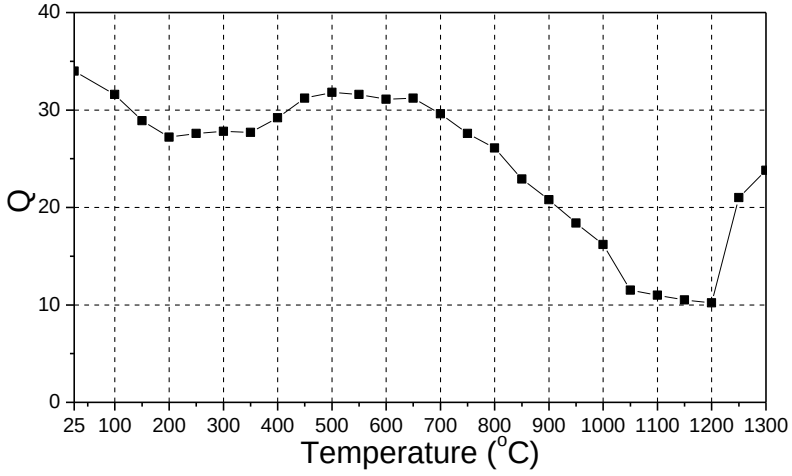

(b)

Figure 5.50:Measured resonant (a) frequency and (b) Q of the Si_4B_1CN (1100^{o}C) sensor

5.5 Conclusion

Based on the temperature-dependant dielectric constant behavior of SiCN materials, three wireless temperature sensing mechanism have been proposed in this chapter for high-temperature applications. Corresponding to different antenna configurations, three different types of sensors are designed and the prototypes are fabricated and tested. All of the sensors successfully perform at temperatures over 1000^{o}C. These wireless passive sensor designs will significantly benefit turbine engines in need of sensors operating at harsh environments.

CHAPTER 6 SUMMARY AND FUTURE WORK

6.1 Summary

This dissertation focused on the high temperature materials characterization and sensor applications. Two contributions have been made in this work, which are summarized as follow:

1) A novel method for precisely characterizing the dielectric properties of high temperature ceramic materials at high temperatures and microwave frequencies are presented in this dissertation. This technique provides accurate characterization of both dielectric constant and loss tangent. The dielectric properties of Si(B)CN ceramics are characterized from 25 to 1300^{o}C. Two different metallization processes are implemented for the measurements with the highest temperatures of 500^{o}C and 1300^{o}C, respectively. Custom-made through-reflect-line (TRL) calibration kits are used to maximize the measurement accuracy at every temperature point. It is observed that the dielectric constant and loss tangent of the Si(B)CN sample increase monotonously with temperature. This temperature dependency of Si(B)CN dielectric properties as well as the dielectrically-loaded cavity resonator structure provides the basis for the development of wireless passive temperature sensors for high-temperature applications.

2) Wireless temperature sensors are designed based on the cylindrical cavity resonator loaded with these temperature dependent dielectric materials. Three different types of sensors are designed and the prototypes are fabricated and tested. All the sensors work over 1000^{o}C.

6.2 Future Work

In order to make the sensors low profile and robust, different materials should be involved as fewer as possible. This can avoid reaction between different materials and minimize thermal mismatch between materials, devices and packaging. For the sensors presented in this dissertation, precious metals are used to cover the ceramic samples to reduce the radiation loss and therefore form dielectrically loaded high Q resonators. These resonators work at the TM_{010} cavity mode. For the conventional TE, TM and hybrid dielectric resonator modes, the radiation loss degrades their Q's especially for low dielectric constants, such as the one of SiCN, which is only between 3 and 5. A potentially effective way to achieve high Q and get rid of metals is to utilize the whispering gallery modes (WGM) of the dielectric resonators. The radiation loss will decrease when WGM's are employed, especially with increase of azimuthal mode number [54]. Compared with patch antennas and slots antennas, dielectric image-line antennas would be better candidates used as receiving/transmitting antennas[55][56], because they are much simpler from the fabrication's point of view.

LIST OF REFERENCES

[1] M. P. Boyce，*Gas Turbine Engineering Handbook, Third Edition,* Gulf Professional Publishing, 2006, Ch. 19.

[2] X. Gong, L. An, and C. Xu, "Wireless passive sensor development for harsh envionment applications," *2012 IEEE International Workshop on Antenna Technology*, Tucson, AZ, Mar. 5-7, 2012.

[3] G. W. Tregay, P. R. Calabrese, P. L. Kaplin, and M J. Finney, "Optical fiber sensor for temperature measurement from 600 to 1900°C in gas turbine engines," *Proceedings of SPIE - The International Society for Optical Engineering*, vol. 1589, pp. 38-47, 1991.

[4] T. Tomoki, S. Koji, O. Yoshihiko, and N. Atsushi, "Temperature measurement of high speed rotating turbine blades using a pyrometer," *Proceedings of the ASME Turbo Expo 2006 - Power for Land, Sea, and Air*, vol. 2, pp. 521-529, 2006.

[5] S. S. Lutz, W. D. Turley, H. M Borella, B. W. Noel, M. R. Cates, and M. R. Probert, "Remote temperaturemeasurement instrumentation for a heated rotating turbine disk," *Proceedings of the ISA Aerospace Instrumentation Symposium*, vol. 34, pp. 217-229, 1988.

[6] A. Bhattacharya, R. R. Srinivasa, K. M. Ghanashyam, "Characterization of Yb_2O_3 based optical temperature sensor for high temperature applications," *Sensors and Actuators, A: Physical*, vol. 134, no. 2, pp. 348-356, 2007.

[7] S. Zappe, J. Franklin, E. Obermeier, M. Eickhoff, H. Moeller, G. Kroetz, C. Rougeot, O. Lefort, and J. Stoemenos, "High temperature 10 bar pressure sensor based on 3C-SiC/SOI for turbine control applications," *Materials Science Forum*, vol. 353-356, pp. 753-756, 2001.

[8] D. J. Young, J. Du, C. A. Zorman, and W. H. Ko, "High-temperature single-crystal 3C-SiC capacitive pressure sensor," *IEEE Sensors Journal*, vol. 4, no. 4, pp. 464-470, August, 2004.

[9] K. Wasa, T. Tohda, Y. Kasahara, and S. Hayakawa, "Highly reliable temperature sensor using RF-sputtered SiC thin film," *Review of Scientific Instruments*, vol. 50, no. 9, pp. 1084-1088, 1979.

[10] P. Nieva, H. Tada, P. Zavracky, G. Adams, I. Miaoulis, and P. Wong, "Mechanical and thermophysical properties of silicon nitride thin films at high temperatures using in-situ MEMS temperature sensors," *Materials Research Society Symposium - Proceedings*, vol. 546, pp. 97-102, 1999.

[11] S. V. Patel, M. DiBattista, J. L. Gland, and J. W. Schwank, "Survivability of a silicon-based microelectronic gasdetector structure for high-temperature flow applications," *Sensors and Actuators, B: Chemical*, vol. B37, no 1-2, pp. 27-35, 1996.

[12] R. S. Okojie, A. A. Ned, A. and D. Kurtz, "Operation of α (6H)-SiC pressure sensor at 500° C," *International Conference on Solid-State Sensors and Actuators*, vol. 2, pp. 1407-1409, 1997.

[13] V. V. Varadan, R. D. Hollinger, D. K. Ghodgaonkar, and V. K. Varadan, "Free-space, broadband measurements of high-temperature, complex dielectric properties at microwave frequencies," *IEEE Trans. Instrum. Meas.*, vol. 40, pp. 842-846, 1991.

[14] T. T. Grove, M. F. Masters, R. E. Miers, "Determining Dielectric Constants Using A Parallel Plate Capacitor," *Am. J. Phys.*, Vol. 73, No. 1, Jan. 2005

[15] Agilent Application Note, "Agilent Basics of Measuring the Dielectric Properties of Materials," Agilent Literature Number 5989-2589en, Jun. 2006

[16] S. Fargeot, D. Guihard, and P. Lahitte, "Dielectric characterization at high temperature (1600°C) for space applications" *IEEE International Conference on Microwave Technology & Computational Electromagnetics (ICMTCE)*, 22-25 May 2011, Beijing, China.

[17] S. Bringhurst, M. F. Iskander, and M. J. White, "Thin sample measurements and error analysis of high temperature coaxial dielectric probes," *IEEE Microwave Theory Tech.*, vol. 45, pp. 2073-2083, 1997.

[18] C. A. Jones, "Permeability and Permittivity Measurements Using Stripline Resonator Cavities: A Comparison," *IEEE Trans. Instrum. Meas.*, Vol. 48, pp. 843–848, Aug. 1999.

[19] X. Gong, W. H. She, E. Hoppenjans, Z. N. Wing, R. Geyer, J. W. Halloran, and W. J. Chappell, "Tailored and anisotropic dielectric constants through porosity in ceramic components," *IEEE Trans. MTT*, vol. 53, pp. 3638-3647, 2005.

[20] L. Liew, W. Zhang, L. An, S. Shah, R. Lou, Y. Liu, T. Cross, K. Anseth, V. Bright, and R. Raj, "Ceramic MEMS – new materials, innovative processing and futuristic applications," *Am. Ceram. Soc. Bull.*, 80(5), pp. 25-30, 2001.

[21] L. Liew, W. Zhang, V.M. Bright, L. An, M.L. Dunn, and R. Raj, "Fabrication of SiCN ceramic MEMS using injectable polymer-precursor technique," *Sensors and Actuators: A. Physical*, 89(1-2), pp. 64-70, 2001.

[22] Y. Liu, L. Liew, R. Lou, L. An, V.M. Bright, M.L. Dunn, J.W. Daily and R. Raj. "Application of microforging in SiCN MEMS structure fabrication," *Sensors and Actuators: A. Physical*, 95 (2-3): pp. 143-151, 2002.

[23] L. Liew, Y. Liu, R. Luo, T. Cross, L, An, V.M. Bright, M.L. Dunn, J.W. Daily, R. Raj. "Fabrication of SiCN MEMS by photopolymerization of pre-ceramic polymer" *Sensors and Actuators: A. Physical*, 95 (2-3): pp. 120-134, 2002.

[24] R. Riedel, G. Passing, H. Schonfelder, and R. J. Brook, "Synthesis of dense silicon-based ceramics at low-temperatures," *Nature*, vol. 35, pp. 714-716, 1992.

[25] R. Riedel, A. Kienzle, W. Dressler, L. Ruwisch, J. Bill, and F. Aldinger, "A silicoboron carbonotride ceramics stable to 2000 Degrees C," *Nature*, vol. 382, pp. 796-798, 1996.

[26] L. An, Y. Wang, L. Bharadwaj, Y. Fan, L. Zhang, D. Jiang, Y. Sohn, V. Desai, J. Kapat and L. Chow, "Silicoaluminum carbonitride with anomalously high resistance to oxidation and hot corrosion," *Adv. Eng. Mater*., vol. 6, no. 5, pp. 337-340, 2004.

[27] Y. Wang, Y. Fan, L. Zhang, W. Zhang, and L. An, "Polymer-derived SiAlCN ceramics resist to oxidation at 1400oC," *Scripta Mater*., vol. 55, pp. 295-297, 2006.

[28] Y. Wang, W. Fei, Y. Fan, L. Zhang, W. Zhang, and L. An, "A silicoaluminum carbonitride ceramic resist oxidation/corrosion in water vapour," *J. Mater. Res*., vol. 21, no. 7, pp. 1625-1628, 2006.

[29] R. Riedel, L.M. Ruwisch, L. An, and R. Raj, "Amorphous silicoboron carbonitride ceramics with anomalously high resistance to creep" *J. Am. Ceram. Soc*., 81, pp. 3341-3344, 1998.

[30] L. An, R. Riedel, C. Konetachny, H.J. Kleebe, and R. Raj. "Newtonian viscosity of amorphous silicon carbonitride at high temperature" *J. Am. Ceram. Soc*., 81, pp. 1349-52, 1998.

[31] A. Dhamne, W. Xu, B. Fookes, Y. Fan, L. Zhang, S. Burton, J. Hu, J. Ford, and L. An, "Polymer-ceramic conversion of liquid polyaluminasilazanes for SiAlCN ceramics" *J. Am. Ceram. Soc*., 88[9], pp 2415-19, 2005.

[32] T. Jiang, "Electronic properties and microstructures of amorphous SiCN ceramics derived from polymer precursors," *Ph.D. Thesis, University of Central Florida*, pp. 102-117, 2009.

[33] R. G. Nitsche, and E. M. Biebl, "A free-space technique for measuring the complex permittivity and permeability in the millimeter wave range," in *IEEE MTT-S Int. Microwave Symp. Dig.*, pp. 1465–1468, 1994.

[34] V. R. K. Murthy, and R. Raman, "A method for the evaluation of microwave dielectric and magnetic parameters using rectangular cavity perturbation technique," *Solid State Communication*, vol. 70, no. 8, pp. 847–850, 1989.

[35] A. Kumar, and S. Sharma, "Measurement of dielectric constant and loss factor of the dielectric material at microwave frequencies," *Progress In Electromagnetics Research*, PIER 69, pp. 47-54, 2007.

[36] X. Ren, T. Jiang, Y. Wang, L. An, and X. Gong, "Characterization of high-temperature ceramic materials at microwave frequencies for MEMS applications," *10th IEEE Wireless and Microwave Technology Conference*, Clear Water, FL, April 2009

[37] W. H. She, E. Hoppenjans, and W. J. Chappell, "Embedded dielectric resonator filter in layered polymer packaging," *IEEE MTT-S Int. Microwave Symp. Dig*., pp. 261-264, 2005.

[38] L. Kirkup, and R. B. Frenkel., *An Introduction to Uncertainty in Measurement: Using the GUM (Guide to the Expression of Uncertainty in Measurement),* Cambridge: Cambridge University Press, pp.53-59, 2006.

[39] C. A. Balanis, *Advanced Engineering Electromagnetics*, New York: J. Wiley & Sons, pp. 494-498, 1989.

[40] D. Kajfez, S. Chebolu, M. R. Abdul-Gaffoor, and A. A. Kishk, "Uncertainty analysis of the transmission-type measurement of Q-factor", *IEEE Trans. MTT*., vol. 47, pp.367 -371, 1999.

[41] G. E. Ponchak, J. L. Jordan, and M. C. Scardelletti, "High Temperature Characteristics of Coplanar Waveguide on R-Plane Sapphire and Alumina," *IEEE Trans. Advanced Packaging*, vol. 31, no. 1, pp.146-151, Feb. 2009.

[42] Agilent network analysis applying the 8510 TRL calibration for non-coaxial measurements, *product note 8510-8A, Agilent Technologies*.

[43] X. Ren, and X. Gong, "A Wireless Sensing Technique Using Passive Microwave Resonators," *2008 IEEE AP-S Int. Symp.*, San Diego, CA, July, 2008.

[44] H. Chen, "Broadband CPW-fed square slot antennas with a widened tuning stub," *IEEE Trans. on Antennas and Propagation*, vol. 51, no. 8, pp. 1982 – 1986,Aug. 2003.

[45] R. Azadegan, and K. Sarabandi, "Miniature high-Q double-spiral slot-line resonator filters", *IEEE Transactions on Microwave Theory and Techniques*, vol. 52, no. 5, pp. 1548 – 1557, May 2004.

[46] X. Ren, S. Ebadi, H. T. Cheng, Y. Chen, L. An, and X. Gong, "Wireless resonant frequency detection of SiCN ceramic resonator for sensor applications," *2011 IEEE AP-S Int. Symp*., Spokane, WA, July 2011.

[47] X. Ren, S. Ebadi, and X. Gong, "A single-antenna wireless passive temperature sensing mechanism using a dielectrically-loaded resonator," in *2012 IEEE AP-S Int. Symp*., Chicago, IL, July 8-14, 2012.

[48] H. Cheng, S. Ebadi, and X. Gong, "A Compact Wireless Passive Temperature Sensor Using a Resonator/Antenna Integration Up to 1000˚C," *IEEE Antennas and Wireless Propagation Letter*, submitted.

[49] H. T. Cheng, S. Ebadi, X.H. Ren, Y. Yusuf, and X. Gong. "A Compact Wireless Passive Sensing Mechanism Based on A Seamlessly Integrated Resonator/Antenna," *2011 IEEE AP-S Int. Symp.*, July 3-8, 2011.

[50] H. T. Cheng, Y. Yusuf, and X. Gong, "Vertically Integrated Three-Pole Filter/Antennas for Array Applications," *IEEE Antennas Wireless Propagat. Lett.*, vol.10, pp.278-281, 2011.

[51] Y. Yusuf, and X. Gong, "Compact low-loss integration of high-Q 3-D filters with highly efficient antennas," *IEEE Trans. on Microwave Theory Tech*., vol. 59, no. 4, pp. 857-865, Apr. 2011.

[52] Y. Yusuf, H. T. Cheng, and X. Gong, "A seamless integration of 3-D vertical filters with highly efficient slot antennas," *IEEE Trans. Antennas Propagat*., vol. 59, no.11, Nov. 2011.

[53] H. A. Haus, *Waves and fields in optoelectronics*, Prentice-Hall, 1984, ch.7.

[54] M. Neshat, D. Saeedkia, S. Gigoyan, and S. Safavi-Naeini, "Mode selective dielectric resonator coupled to dielectric image waveguide for sensing applications," in *Proc. 32nd Int. Conf. Infrared Millimeter Waves*, Cardiff–Wales, U.K., pp. 764–765, Sep. 2007.

[55] Song Lin, Joshua L. Wilson, Aly E. Fathy and Suren Gigoyan, "Development of millimeter wave antennas and associated feed network components using dielectric image guide," *International Journal of RF and Microwave Computer-Aided Engineering*, vol. 20, pp. 56–65, Jan. 2010.

[56] S. Gigoyan, D. Saeedkia, M. Neshat, H. Chen, and S. Safavi-Naeini, "Tapered Dielectric Image-Line Antenna Array for Millimeter-Wave Applications," *2008 IEEE Radio and Wireless Symposium* , pp.667-670, Jan. 2008.